Search for $\nu_\mu \to \nu_e$ oscillation using 250 km long baseline neutrino beam

Makoto Yoshida

January 26, 2001

Abstract

The KEK-Kamioka (K2K) long baseline ν_μ beam experiment has successfully taken data both at KEK and at Kamioka to search for neutrino oscillations for the period from June 1999 to June 2000, during which 2.29×10^{19} protons were delivered on the target to generate neutrinos.

When we assume 3-flavor neutrino oscillations with one mass scale dominance, the electron neutrinos are expected to appear against the background events from ν_μ mis-identification and ν_e contamination to our beam.

First of all, we measured the ν_e/ν_μ interaction ratio to be $1.76 \pm 0.62(\text{stat.})^{+0.76}_{-1.00}(\text{sys.})(\%)$ at the KEK site. Thus, it is confirmed that the amount of ν_e contamination in our ν_μ beam is as small as the prediction by our beam simulation, 1.3%.

We searched for ν_e appearance at Super-Kamiokande by detecting single-ring e-like fully-contained events, and found 1 such event.

We estimated the number of background electron events to be observed in Super-Kamiokande by extrapolating the neutrino interaction rate in the 1 kilo-ton water Cherenkov detector at the KEK site. As a result, the expected number of single-ring e-like FC events in Super-Kamiokande is calculated to be $1.92^{+0.89}_{-0.88}(\text{sys.})$ events from ν_μ mis-identification and beam ν_e contamination, which is consistent with the observed number, 1 event.

Therefore, we conclude that no evidence for $\nu_\mu \to \nu_e$ oscillations is found in this analysis. The following parameter region assuming $\nu_\mu \to \nu_e$ oscillations is excluded at 90% confidence level: $\sin^2 2\theta_{13} \gtrsim 0.7$ and $\Delta m^2 \gtrsim 3 \times 10^{-3}$. This is the first experimental limit in the world on $\nu_\mu \to \nu_e$ appearance oscillation sensitive to $\Delta m^2 \sim 3 \times 10^{-3} \text{eV}^2$.

Acknowledgment

Contents

List of Figures

List of Tables

Chapter 1

Introduction

1.1 Neutrino Mass

Neutrinos are assumed to be massless in the standard model of the elementary particles [1, 2, 3]. The finite mass of the neutrino has been searched for since the existence of neutrino was predicted by Pauli[5] in the 1930's to explain the continuous energy spectrum of emitted electrons in nuclear β decays.

Direct mass measurements of the neutrinos have only succeeded in giving upper limits. The best method to measure the ν_e mass was to study the end point in the electron energy spectrum of tritium decays. If the ν_e has a finite mass, m_{ν_e}, then the end-point can be shifted to a lower value by m_{ν_e}. What is interesting about the ν_e mass measurements is that all the best experiments have obtained negative values for the square of the mass. The Particle Data Group give a limit of 3 eV from tritium data. Nowadays, they also refer to the astrophysical mass limit of 23eV [7]. It was derived from the arrival time spread of the neutrinos from SN 1987A, coupled with the measured neutrino energies to provide a simple time-of-flight limit on m_{ν_e}. It can be regarded as a safe limit. The PSI group gives an upper limit on the ν_μ mass of 170keV[8]. It is based on decay kinematics of pions into a muon and a neutrino. The best ν_τ mass measurement is obtained by the ALEPH collaboration which studied the end point in the τ invariant mass distribution of the decay of a τ particle, $\tau \to 3\pi\nu_\tau$ and $\tau \to 5\pi(\pi^0)\nu_\tau$ and set an upper limit of 18.2MeV[9].

The best upper limits at present on the mass of each neutrino species are summarized in Table 1.1

Flavor	Mass Limit	Experiment
ν_e	3eV	tritium β decays[7]
ν_μ	170keV (90% C.L.)	PSI[8]
ν_τ	18.2MeV (95% C.L.)	ALEPH[9]

Table 1.1: Best neutrino mass limits at present

1.2 Neutrino Oscillations

If the neutrinos have finite mixings and non-degenerate masses, the flavor changing phenomena, called neutrino oscillations, can occur. Neutrino oscillations were proposed by Z.Maki, M.Nakagawa and S.Sakata[12], and by B.Pontecorvo[13].

Neutrinos interact via the weak interaction in the flavor eigenstates $|\nu_\alpha\rangle$ ($\alpha = e, \mu, \tau$). However, if they have a finite mass, the mass eigenstates $|\nu_i\rangle$ ($i = 1, 2, 3$) exist and the flavor states can be expressed by the superposition of the mass eigenstates as follows:

$$|\nu_\alpha\rangle = \sum_i U_{\alpha i} |\nu_i\rangle \tag{1.1}$$

where U is a unitary mixing matrix ($UU^\dagger = U^\dagger U = 1$). In the following, we will consider the flavor indices $\alpha, \beta = e, \mu, \tau$ and the mass indices $i, j = 1, 2, 3$. The mixing matrix for three neutrinos, Maki-Nakagawa-Sakata matrix[12, 13], is usually expressed as follows, analogously to the Cabibbo-Kobayashi-Maskawa (CKM) quark mixing matrix[16]:

$$U = \begin{pmatrix} c_{12}c_{13} & s_{12}c_{13} & s_{13}e^{-i\delta} \\ -s_{12}c_{23} - c_{12}s_{23}s_{13}e^{i\delta} & c_{12}c_{23} - s_{12}s_{23}s_{13}e^{i\delta} & s_{23}c_{13} \\ s_{12}s_{23} - c_{12}c_{23}s_{13}e^{i\delta} & -c_{12}s_{23} - s_{12}c_{23}s_{13}e^{i\delta} & c_{23}c_{13} \end{pmatrix}, \tag{1.2}$$

where s_{ij} and c_{ij} (i, j=1,2,3) stand for $\sin\theta_{ij}$ and $\cos\theta_{ij}$ respectively, and θ_{ij} and δ are the mixing angle and the CP violation phase.

The mass eigenstate $|\nu_i\rangle$ with a finite mass m_i, momentum p and energy $E_i = \sqrt{p^2 + m_i^2}$ satisfies the following energy eigenvalue equation:

$$\mathcal{H}_0 |\nu_i\rangle = E_i |\nu_i\rangle . \tag{1.3}$$

where $\mathcal{H}_0$ is the free neutrino Hamiltonian. The time evolution of the flavor state is expressed by the Schrödinger equation:

$$\begin{aligned} i\frac{d}{dt} |\nu_\alpha(t)\rangle &= \mathcal{H}_0 |\nu_\alpha(t)\rangle \\ &= \sum_i U_{\alpha i} E_i |\nu_i(t)\rangle \\ &= \sum_{i,\beta} U_{\alpha i} \left[E_i \exp\left(-iE_i t\right) \right] U_{\beta i}^* |\nu_\beta(t)\rangle \end{aligned}$$

$$\tag{1.4}$$

The $|\nu_\alpha(t)\rangle$ can be obtained by solving this equation analytically:

$$\begin{aligned} |\nu_\alpha(t)\rangle &= \sum_{i,\beta} U_{\alpha i} \exp\left(-iE_i t\right) U_{\beta i}^* |\nu_\beta(0)\rangle \\ &= \exp\left(-ipt\right) \sum_{i,\beta} U_{\alpha i} \exp\left(-i\frac{m_i^2}{2p} t\right) U_{\beta i}^* |\nu_\beta(0)\rangle \end{aligned}$$

$$= \sum_{\beta} A_{\alpha\beta} \, |\nu_{\beta}(0)\rangle \, , \tag{1.5}$$

where $A_{\alpha\beta}$ shows the transition amplitude from ν_{β} to ν_{α}. The relativistic approximation $E_i \simeq p + m_i^2/2p$ is used in (1.5).

Using the unitarity condition

$$\sum_{j} U_{\alpha j} U_{\beta j}^* = \delta_{\alpha\beta}, \tag{1.6}$$

the oscillation probability is calculated as:

$$
\begin{aligned}
P(\nu_{\beta} \to \nu_{\alpha}) &= |A_{\alpha\beta}|^2 \\
&= \mathrm{Re} \sum_{j,k} U_{\alpha j} U_{\beta j}^* U_{\alpha k}^* U_{\beta k} \exp\left(-i\frac{\Delta m_{jk}^2 L}{2p}\right), \\
&= \delta_{\alpha\beta} - \mathrm{Re} \sum_{j,k} U_{\alpha j} U_{\beta j}^* U_{\alpha k}^* U_{\beta k} \left\{1 - \exp\left(-i\frac{\Delta m_{jk}^2 L}{2p}\right)\right\}, \tag{1.7} \\
&= \delta_{\alpha\beta} - 4 \sum_{j<k} U_{\alpha j} U_{\beta j}^* U_{\alpha k}^* U_{\beta k} \sin^2\left(\frac{\Delta m_{jk}^2 L}{4p}\right), \tag{1.8}
\end{aligned}
$$

where $\Delta m_{jk}^2 \equiv m_j^2 - m_k^2$ is the difference of mass squared, and the neutrino propagation length L is equal to the time τ in natural unit.

1.2.1 2-flavor Oscillations

In the two flavor mixing case, the mixing matrix is simplified and given by the following 2 by 2 matrix with θ being the only one mixing angle:

$$U = \begin{pmatrix} \cos\theta & \sin\theta \\ -\sin\theta & \cos\theta \end{pmatrix} \tag{1.9}$$

The oscillation probability (1.8) is given in a much simpler form:

$$P(\nu_{\beta} \to \nu_{\alpha}) = \sin^2 2\theta \sin^2\left(\frac{\Delta m^2 L}{4p}\right) \qquad (\alpha \neq \beta) \tag{1.10}$$

$$= \sin^2 2\theta \sin^2\left(\pi \frac{L}{L_v}\right) \tag{1.11}$$

$$P(\nu_{\alpha} \to \nu_{\alpha}) = 1 - \sin^2 2\theta \sin^2\left(\frac{\Delta m^2 L}{4p}\right) \tag{1.12}$$

$$= \sin^2 2\theta \sin^2\left(\pi \frac{L}{L_v}\right), \tag{1.13}$$

Equation 1.10 shows the transition probability from ν_{β} to ν_{α} and Eq.1.12 shows the survival probability of ν_{α}. The oscillation length, L_v is defined by momentum p and Δm^2,

$$L_v = \frac{4\pi p}{|\Delta m^2|}$$

$$= 2.48 \left(\frac{p}{\text{GeV/c}}\right) \left(\frac{|\Delta m^2|}{\text{eV}^2}\right)^{-1} \text{km} . \qquad (1.14)$$

In the case of $L \gg L_v$, the survival probability approaches to $1 - 1/2 \sin^2 2\theta$, where factor $1/2$ appears because the value of $\sin^2\left(\frac{\Delta m^2 L}{4p}\right)$ averages out. In this experiment, K2K, the nominal neutrino energy is $1.3\,\text{GeV}$ and the neutrino flight length L is $250\,\text{km}$. Therefore, the parameter region down to $\Delta m^2 \sim 7 \times 10^{-3}$ will be investigated at large mixing angles.

1.2.2 3-flavor Oscillations with One Mass Scale

The behavior of the 3-flavor mixing oscillations is much more complicated than that of the 2-flavor mixing case. The oscillation probability is expressed by the superpositions of three wave components, whose oscillation lengths are $4\pi p/|\Delta m_{21}^2|$, $4\pi p/|\Delta m_{32}^2|$ and $4\pi p/|\Delta m_{31}^2|$. Therefore the physical implications are far from transparent.

However, assuming

1. the neutrino mass hierarchy

$$m_1 < m_2 < m_3 ,$$

2. $\Delta m_{32}^2 = (3 \pm 1.5) \times 10^{-3}\text{eV}^2$
   from the Super-Kamiokande atmospheric neutrino results[18] ;

3. $\Delta m_{21}^2 = (3 - 10) \times 10^{-5}\text{eV}^2$
   from the combined result of solar neutrino expriments[18] ,

the oscillation behavior becomes much simpler [14, 15]. In this case,

$$\Delta m_{32}^2 = \Delta m_{31}^2 = \Delta m^2 \Delta m_{21}^2 \ll \Delta m^2,$$

where $\Delta m^2 = m_3^2 - m_{1,2}^2$ is the dominant mass square difference in the neutrino oscillation (one mass scale dominance).

The generic oscillation probability (1.8) is modified with $\Delta m_{32,31}^2 \to \Delta m^2$ and $\Delta m_{21}^2 \to 0$,

$$\begin{aligned}
P(\nu_\beta \to \nu_\alpha) &= \delta_{\alpha\beta} - 4(U_{\alpha 1}U_{\beta 1}^* + U_{\alpha 2}^* U_{\beta 2})U_{\alpha 3}U_{\beta 3}^* \sin^2\left(\frac{\Delta m^2 L}{4p}\right) \\
&= \delta_{\alpha\beta} - 4(\delta_{\alpha\beta} - U_{\alpha 3}U_{\beta 3}^*)U_{\alpha 3}U_{\beta 3}^* \sin^2\left(\frac{\Delta m^2 L}{4p}\right) \qquad (1.15)
\end{aligned}$$

After the unitarity condition (1.6) is applied in (1.15), the transition and survival probabilities are expressed by

$$P(\nu_\beta \to \nu_\alpha) = 4|U_{\alpha 3}|^2 |U_{\beta 3}|^2 \sin^2\left(\frac{\Delta m^2 L}{4p}\right) \qquad (\alpha \neq \beta) \qquad (1.16)$$

$$P(\nu_\alpha \to \nu_\alpha) = 1 - 4|U_{\alpha 3}|^2 (1 - |U_{\alpha 3}|^2) \sin^2\left(\frac{\Delta m^2 L}{4p}\right) . \qquad (1.17)$$

The following features of oscillation probabilities are considered in this oscillation scheme:

- Δm^2, $|U_{e3}|^2$, $|U_{\mu 3}|^2$ and $|U_{\tau 3}|^2$ appear in the oscillation probabilities, however $|U_{\tau 3}|^2$ is equal to $1 - |U_{e3}|^2 - |U_{\mu 3}|^2$ according to the unitarity condition (1.6). Referring to Eq. 1.2, $|U_{e3}|^2$, $|U_{\mu 3}|^2$ and $|U_{\tau 3}|^2$ is expressed to be

$$
\begin{aligned}
|U_{e3}|^2 &= \sin^2 \theta_{13}, \\
|U_{\mu 3}|^2 &= \cos^2 \theta_{13} \sin^2 \theta_{23}, \\
|U_{\tau 3}|^2 &= \cos^2 \theta_{13} \cos^2 \theta_{23}.
\end{aligned}
$$

(1.18)

As a result, the oscillation probabilities are determined by only three parameters, $(\Delta m^2, \theta_{23}, \theta_{13})$, and does not depend on the mixing angle, θ_{12}, and the CP violating phase, δ.

- All oscillation channels ($\nu_e \leftrightarrow \nu_\mu$, $\nu_\mu \leftrightarrow \nu_\tau$, $\nu_e \leftrightarrow \nu_\tau$) are open and have the same oscillation length $L_\nu = 4\pi p / |\Delta m^2|$. Pure 2-flavor oscillations are also available by the following parameterization:

$$
\begin{aligned}
\theta_{13} &= 0 & \text{pure } \nu_\mu \leftrightarrow \nu_\tau \\
\theta_{23} &= \pi/2 & \text{pure } \nu_e \leftrightarrow \nu_\mu \\
\theta_{23} &= 0 & \text{pure } \nu_e \leftrightarrow \nu_\tau
\end{aligned}
$$

- The expressions (1.16) and (1.17) have the same form as in the two flavor mixing case with the replacement,

$$
\sin^2 2\theta_{\alpha\beta} = 4|U_{\alpha 3}|^2 |U_{\beta 3}|^2,
$$

(1.19)

$$
\sin^2 2\theta_{\alpha\alpha} = 4|U_{\alpha 3}|^2 (1 - |U_{\alpha 3}|^2).
$$

(1.20)

These equations are useful in comparing the 3-flavor oscillation scenario with the experimental results which were analyzed using the 2-flavor mixing scheme.

1.3 Neutrino oscillation experiments

1.3.1 Atmospheric neutrino experiments

Several experiments have undertaken measurements of the flavor content of the atmospheric neutrino fluxes. Atmospheric neutrinos are produced by the decays of pions and kaons generated when primary cosmic rays strike the upper atmosphere. The energy spectrum of these neutrinos peaks at $\sim 1 GeV$ and extends to 100's of GeV. The neutrino flight distances vary from 15 km for neutrinos produced directly above the detector to 13,000 km for neutrinos produced

on the opposite side of the Earth, making measurements of atmospheric neutrinos sensitive to the neutrino oscillation parameter Δm^2 down to $10^{-4} eV^2$. While the predicted total flux of atmospheric neutrinos is $\sim 20\%$ uncertain, the $(\nu_\mu + \bar{\nu}_\mu)/(\nu_e + \bar{\nu}_e)$ ratio is predicted with only 5% uncertainty. This ratio has been measured by several underground experiments. To help interpret the results and cancel out systematic uncertainties, these measurements are compared to expectations based on detailed Monte Carlo simulations. The experiments frequently report a "double ratio" $R \equiv (N_\mu/Ne)_{DATA}/(N_\mu/N_e)_{MC}$ where N_μ is the number of muon-like events (referred to as "$\mu - like$" or "tracks") and N_e is the number of electron-like events (referred to as "$e - like$" or "showers"). R values obtained by underground water Cherenkov detectors (Kamiokande[17], IMB[19] and Super-Kamiokande[24]) and iron-calorimeter detectors (Fréjus[21, 22], NUSEX[20] and Soudan-2[23]) are summarized in Table 1.2. All the high-statistics experiments give R values significantly lower than one. Early concerns that the atmospheric neutrino anomaly was only present in the water Cherenkov detectors have been relieved by the results of the iron-calorimeter experiment Soudan-2. In addition to low values,

	exposure	R
Kamiokande (sub-GeV)	8.2 kt-yr	$0.60^{+0.06}_{-0.05}$(stat.) $\pm$ 0.05(sys.) [17]
Kamiokande (multi-GeV)	8.2 kt-yr (FC)	$0.57^{+0.08}_{-0.07}$(stat.) $\pm$ 0.07(sys.)[17]
	6.0 kt-yr (PC)	
Super-Kamiokande (sub-GeV)	33 kt-yr	0.63 ± 0.03(stat.) $\pm$ 0.05(sys.) [24]
Super-Kamiokande (multi-GeV)	33 kt-yr	0.65 ± 0.05(stat.) $\pm$ 0.08(sys.) [24]
IMB	7.7 kt-yr	$0.54 \pm 0.05 \pm 0.012$ [19]
Fréjus	2.0 kt-yr	$1.00 \pm 0.15 \pm 0.08$ [21]
NUSEX	0.74 kt-yr	$0.99^{+0.35}_{-0.25}$ [20]
Soudan-2	3.9 kt-yr	$0.64 \pm 0.11^{+0.06}_{-0.05}$[23]

Table 1.2: Summary of the measured R values by various atmospheric neutrino experiments. The variable R is defined in the text.

the Kamiokande and Super-Kamiokande experiments measured a zenith angle dependence of R, and the Super-Kamiokande experiment reported evidence for oscillations of the atmospheric neutrinos in 1998 [24]. The most impressive figures are the zenith angle dependence of e-like and μ-like events (Fig.1.1). These figures show the deficit in the upward-going muon events. Upward-going muons come from muon neutrinos having traveled from the opposite side of the Earth. The zenith angle distribution of electron events is not in conflict with the MC prediction.

1.3.2 Reactor experiments

At nuclear power reactors, electron anti-neutrinos are produced in the nuclear fissions of ^{235}U, ^{238}U, ^{239}P, and ^{241}Pu with a mean energy of $\sim 3 MeV$. The anti-neutrinos are detected based on the reaction $\bar{\nu}_e + p \rightarrow e^+ + n$. Detectors are typically placed at 10's of meters up to 1 km from the reactor core. Search for $\bar{\nu}_e$ disappearance is sensitive to oscillations with Δm^2 down to $\sim 10^{-3} eV^2$.
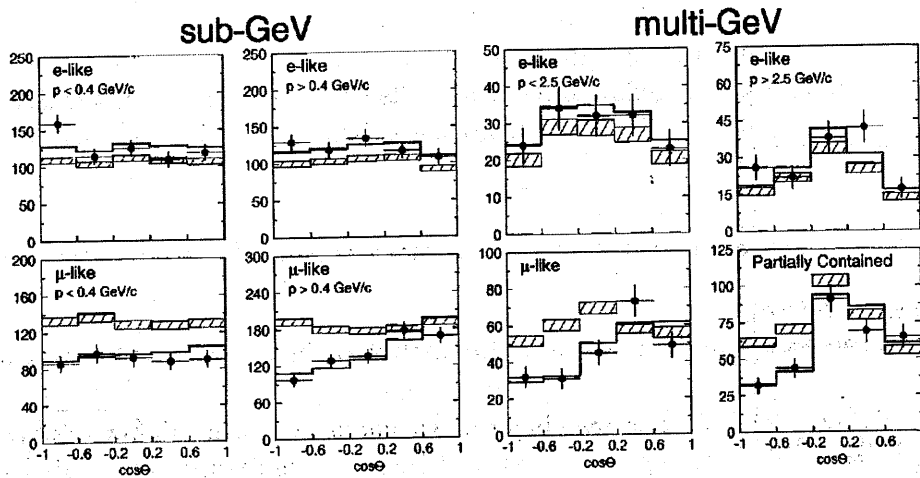
Figure 1.1: Zenith angle distribution of μ-like and e-like events for sub-GeV and multi-GeV data sets[24]. Upward-going particles have $\cos\Theta \leq 0$ and downward-going particles have $\cos\Theta \geq 0$. Sub-GeV data are shown separately for $p \leq 400$ MeV/c and $p \geq 400$MeV/c. Multi-GeV e-like distributions are shown for $p \leq 2.5$GeV/c and $p \geq 2.5$GeV/c and the multi-GeV μ-like are shown separately for FC(Fully Contained in the Super-Kamiokande detector) and PC(Partially contained in the Super-Kamiokande detector) events. The hatched region shows the Monte Carlo expectation for no oscillations. The bold line is the best fit for $\nu_\mu \leftrightarrow \nu_\tau$ oscillations with the overall flux normalization fitted as a free parameter.

The Gösgen [27] experiment measured the $\bar{\nu}_e$ rate in three detectors placed 37.9, 45.9, and 64.7 m from the reactor core. Based on a comparison among the neutrino spectra at each distance, no evidence for oscillations was found, excluding a region of parameter space extending down to $2 \times 10^{-2} eV^2$ for $sin^2 2\theta = 1$ and $sin^2 2\theta > 0.2$ for $\Delta m^2 > 5eV^2$ at 90% confidence level (CL).

The Bugey [28] experiment also used three detectors, placed 15, 40 and 95 m from the nuclear core. No evidence for spectral distortions was found in the three detectors, excluding a large range of oscillation parameter space with $\Delta m^2 > 10^{-2} eV^2$ and $sin^2 2\theta > 2 \times 10^{-2}$ at 90% CL.

The most sensitive reactor neutrino oscillation experiment was carried out by the CHOOZ [26] collaboration. Using a detector located in a tunnel 1 km from the reactor core, the CHOOZ experiment (completed in 1998) searched for evidence for oscillations by comparing the measured $\bar{\nu}_e$ spectrum with the expected spectrum. No evidence for spectral distortion was found, excluding a region of oscillation parameter space down to $0.9 \times 10^{-3} eV^2$ at $sin^2 2\theta = 1$ and $sin^2 2\theta > 0.18$ at large Δm^2 regions.

1.3.3 Accelerator experiments

Neutrinos are produced at accelerators from the decay of pions produced by collisions of protons with a target. Proton beam energies are typically 1 - 10 GeV producing neutrinos of energies from hundreds of MeV. The distances from a neutrino source to a detector, baselines, of the experiments are less than 1 km making typical accelerator-based experiments sensitive down to $\Delta m^2 \sim 0.1 eV^2$.

An experiment E-776 at Brookhaven National Laboratory sought for evidence for $\nu_\mu - \nu_e$ oscillations by searching for ν_e and $\bar{\nu}_e$ appearance 1 km from the neutrino source. No oscillations were found setting the limits on $\Delta m^2 < 0.075 eV^2$ at maximal mixing and $sin^2 2\theta < 0.003$ for large Δm^2 regions[25].

At Fermilab, the E-531 collaboration sought for evidence for oscillations of $\nu_e - \nu_\tau$ and $\nu_\mu - \nu_\tau$ using an emulsion spectrometer to search for τ decays. No candidates were found [29]. Several neutrino oscillation searches have been conducted at CERN:

- CDHSW [30], which used two detectors placed 130 m and 885 m from the neutrino source to search for ν_μ oscillations. No evidence was found excluding the region $0.26 < \Delta m^2 < 90 eV^2$.

- CHARM [31], which searched for $\nu_\mu - \nu_e$ as well as $\nu_\mu - \nu_\tau$ oscillations by looking for ν_e appearance and by comparing the relative fluxes at two detectors placed 123 m and 903 m from the neutrino source. Limits of $\Delta m^2 < 0.20 eV^2$ for $\nu_\mu - \nu_e$, and $\Delta m^2 < 0.29 eV^2$ for $\nu_\mu - \nu_x$ are given assuming the maximal mixing in both cases.

- CHORUS [32], which used a hybrid detector consisting primarily of a 770 kg nuclear emulsion target to search for τ appearance. No candidate has been found, excluding a large region of parameter space for $\nu_\mu - \nu_\tau$ oscillations with $\Delta m^2 > 1 eV^2$.

- NOMAD [33], which looked for evidence for the decay $\tau^- \rightarrow e^- \bar{\nu}_e \nu_\mu$ as well as other τ decay modes. No oscillations have been found limiting $\nu_\mu - \nu_\tau$ oscillations to $sin^2 2\theta <$

4.2×10^{-3} at large Δm^2 region and $\Delta m^2 < 1.5 eV^2$ at large mixing angle.

The Liquid Scintillator Neutrino Detector (LSND) at the Los Alamos Meson Physics Facility has reported evidence for appearance of ν_e and $\bar{\nu}_e$ from pure beams of ν_μ and $\bar{\nu}_\mu$ with $\Delta m^2 \sim 1 eV^2$ and $sin^2 2\theta \sim 10^{-2}$ [34].

The evidence for neutrino oscillations reported by LSND has not been confirmed. The Karlsruhe Rutherford Medium Energy Neutrino experiment (KARMEN) also uses liquid scintillator to search for ν_e appearance from a ν_μ beam produced by muon decays at rest in a detector located at a distance of 17.7 m from the neutrino source. KARMEN has found no evidence for ν_e appearance above the expected background and excludes a region of oscillation parameter space at the edge of the LSND allowed region [34]. Fermilab will attempt to confirm the LSND and KARMEN results with the MiniBooNE experiment [35].

1.3.4 Summary of neutrino oscillation experiments

The existence of neutrino oscillations would imply that neutrinos have a finite mass and that there exist mixings among neutrinos with different flavors. It is sensitive to the non-zero neutrino masses and mixings over a broad range of parameter regions. Only the LSND collaboration among the experiments using the artificial neutrinos reported evidence for such oscillations. There are also some indications and evidence for neutrino oscillations reported by experiments observing atmospheric neutrinos.

The results of searches for neutrino oscillations are summarized in Figure 1.2 ($\nu_\mu - \nu_e$ and $\nu_e - \nu_x$), and Figure 1.3 ($\nu_\mu - \nu_\tau$ and $\nu_\mu - \nu_x$). The two positive signals of neutrino oscillations in the parameter region $10^{-4} eV^2 < \Delta m^2 < 1 eV^2$ are from the observations of atmospheric neutrinos from the LSND experiment. The observations of atmospheric neutrinos have been confirmed by several experiments. The observation of ν_e appearance by LSND from ν_μ has not been confirmed. However, there is currently no other experiment that can exclude the entire LSND allowed region.

1.4 K2K Long Baseline Neutrino Oscillation Experiment

Super-Kamiokande collaboration declared that they found an evidence for ν_μ oscillation based on the atmospheric neutrino data, suggesting the neutrino oscillation parameters ($sin^2 2\theta, \Delta m^2$) are located at ($0.8 \sim 1.0$, $10^{-3} \sim 10^{-2} eV^2$). In the accelerator experiments, the neutrino flux and their flavor is well known (almost pure muon neutrinos). Thus, we can confirm the evidence for neutrino oscillations very clearly. The distance from the neutrino generation point to the detection point should be long, on the order of 100 km to probe such a small Δm^2 with a neutrino beam of energies around 1 GeV.

In order to test the atmospheric neutrino results, several long baseline neutrino experiments have been proposed. K2K is a proposal to use the KEK-PS accelerator to produce ν_μ beam and the Super-Kamiokande detector and is the first among them that has been carried out.

Figure 1.4 shows a schematic view of the K2K experiment. Since the intensity of the beam decreases in proportion to the inverse of the distance squared in the first approximation, the detector at the far end of the beam line must be massive. The Super-Kamiokande detector (SK)
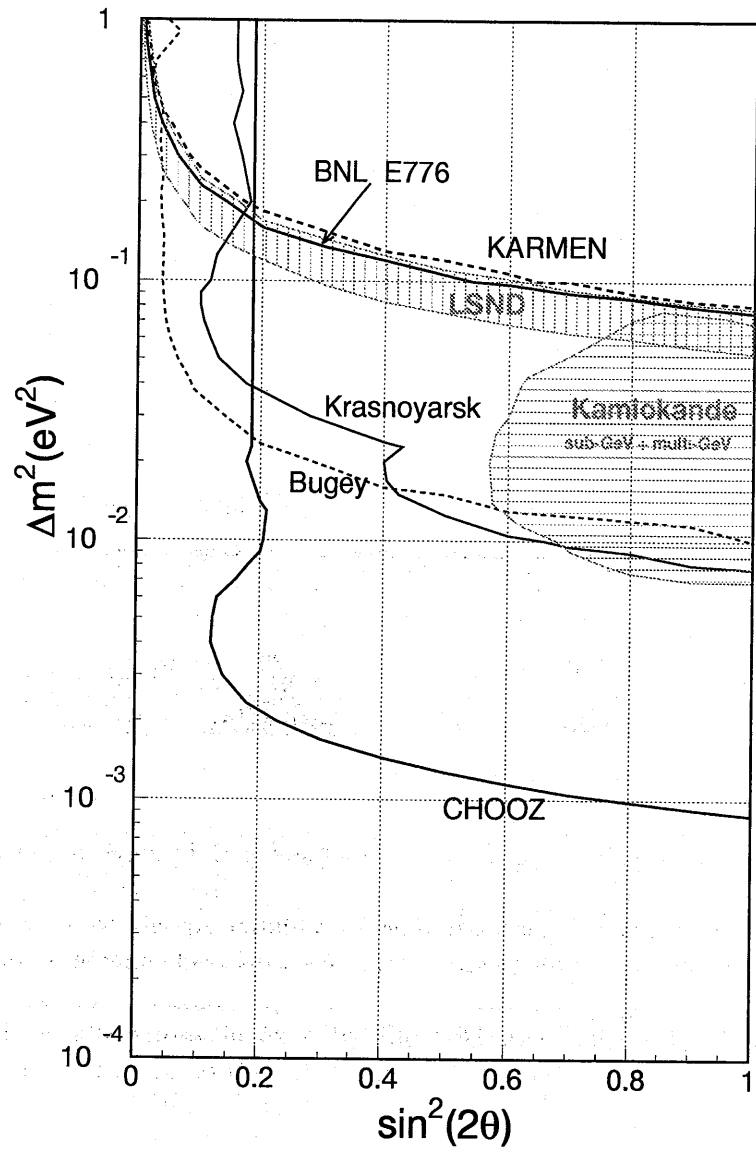
Figure 1.2: Allowed(shaded areas) and excluded(lines) regions of parameter space for $\nu_\mu \to \nu_e$ or $\bar{\nu}_e \to \bar{\nu}_x$ oscillations. The excluded regions lie on the right side of curves.
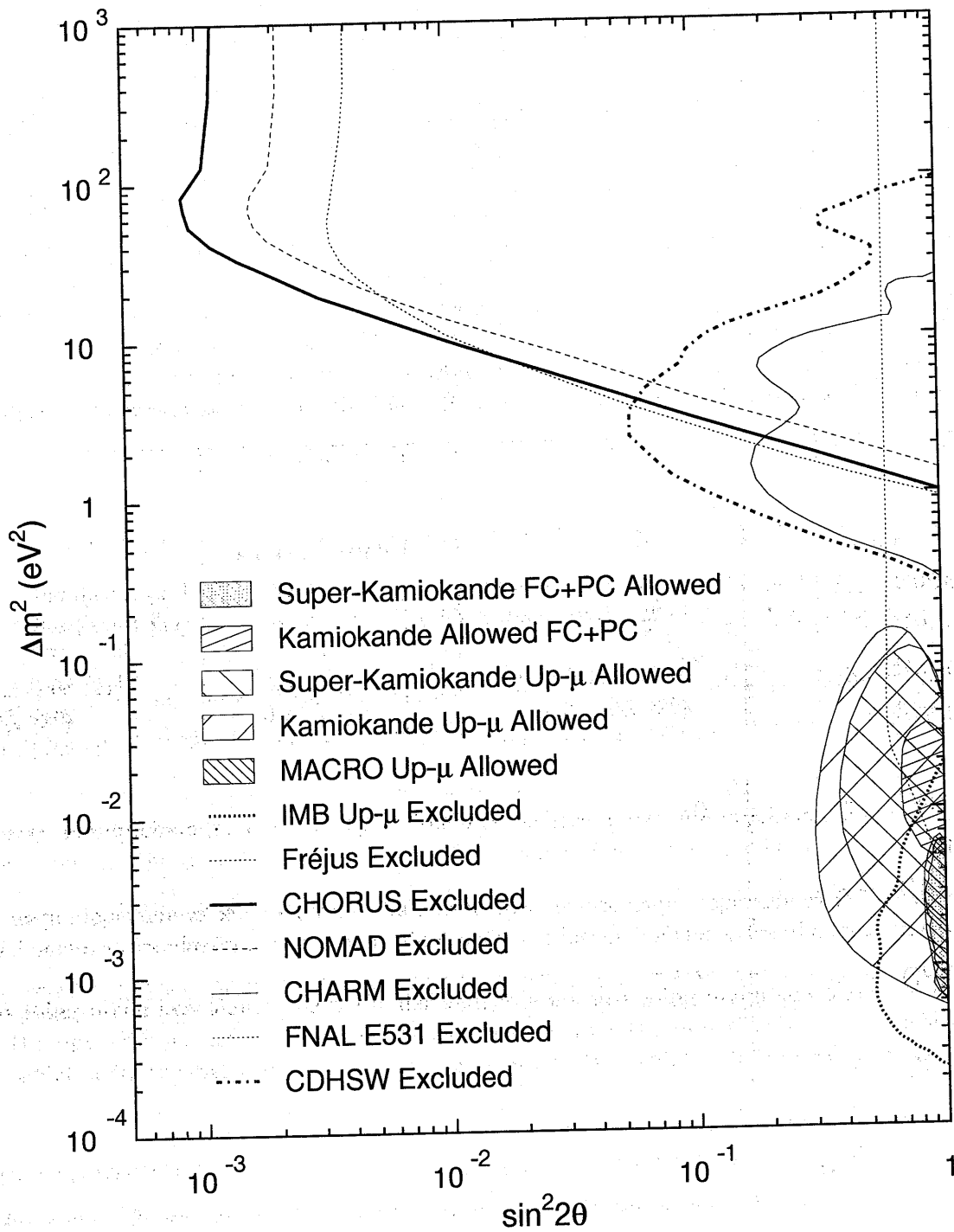
Figure 1.3: Allowed and excluded regions of parameter space for $\nu_\mu - \nu_\tau$ oscillations. In each case, the excluded regions lie on the right side of curves.
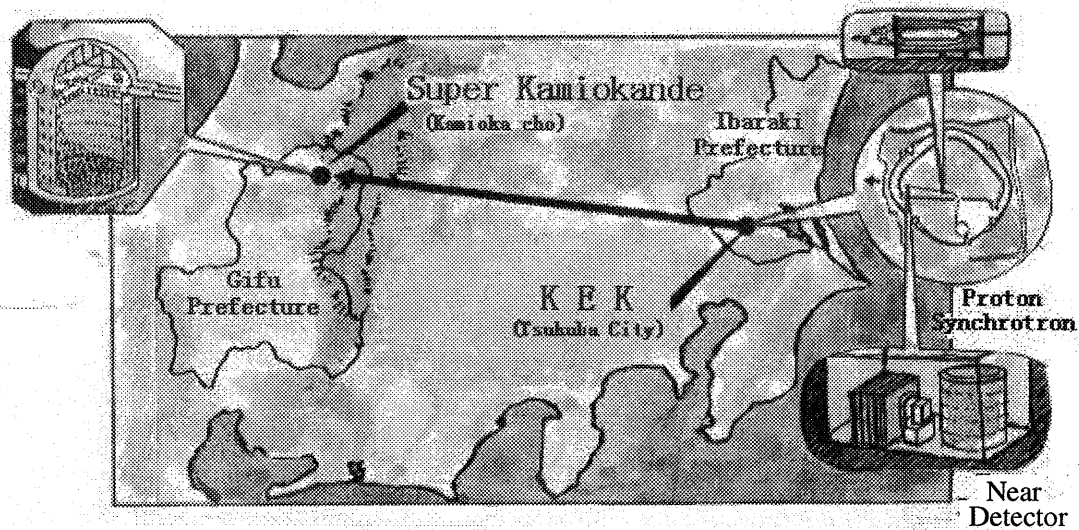
Figure 1.4: Schematic view of K2K

is quite proper for this purpose. We also have near detectors and secondary beam monitors on the KEK site in order to measure the neutrino beam characteristics just after its generation. In this experiment, the distance from the neutrino creation point to the detection point is fixed. Therefore we can see a clear oscillation pattern if we measure the neutrino energy precisely. Figure 1.5 shows the expected oscillation patterns assuming two sets of typical neutrino oscillation parameters. The top figures show the probability of neutrino oscillations as a function of neutrino energy. The middle ones show the distortion of the neutrino flux at SK. The histograms show the MC expected neutrino flux. The shaded one is the expected flux with oscillation assumption. The bottom ones correspond to the total expected number of events at SK. Distortion in the observed neutrino energy spectrum is a definite evidence for neutrino oscillations.

1.5 Motivation of this thesis

The K2K experiment can also search for $\nu_\mu \to \nu_e$ oscillations. When the oscillation occurs in such mode, electron signals are expected to appear at SK with a small background contamination, because the ν_e contamination in the ν_μ beam is expected to be $\sim 1\%$. Although the CHOOZ[26] experiment excluded the allowed parameter region by Kamiokande, they used the $\bar{\nu}_e \leftrightarrow \bar{\nu}_\mu$ mode by measuring the disappearance of $\bar{\nu}_e$ signal from the reactor. Therefore K2K is the first experiment to detect ν_e appearance signal to search for Δm^2 down to as small as $10^{-3} \, \text{eV}^2$.

In this thesis, we discuss $\nu_\mu \to \nu_e$ neutrino oscillations using K2K data taken during 1999 and 2000.
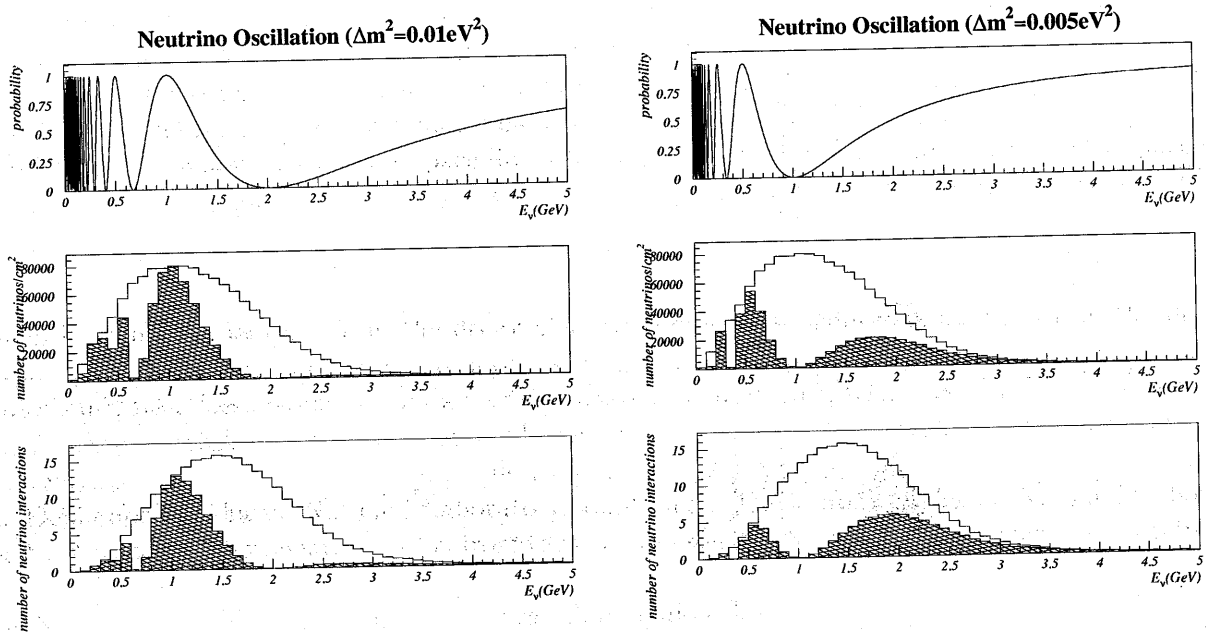
Figure 1.5: Neutrino energy spectrum distortion in the K2K in two Δm^2 cases (Δm^2=0.01 (Left) and Δm^2=0.005 (Right), $\sin^2 2\theta$=1).

In both the left and right figures, the top figures show the probability of neutrino oscillations as a function of energy. The middle ones shows the distortion of the neutrino flux at SK. The histograms show the MC expected neutrino flux (units are "number of neutrinos/cm^2/10^{20}POT(Proton On Target)"). The shaded one is the expected flux with oscillation assumption the probability. The bottom ones correspond to the total expected number of events at SK.

In Chapter 2, we will describe the set-up of the K2K. In Chapter 3, the Monte Carlo simulations which are used in this experiment are described. The ν_e contamination measured by a fine-grained detector at the near site will be described in Chapter 4. Chapter 5 describes how the neutrino flux is measured by the 1kt water Cherenkov detector at the near site to estimate the event rate at SK. The electron event selection at SK is described in Chapter 6. Chapter 7 describes the method to get the expected number of neutrino events at SK. Finally, we compare the expected and the observed number of events at SK in Chapter 8 to draw a conclusion.

Chapter 2

Experimental Setup

2.1 Neutrino Beam Line

2.1.1 KEK 12GeV Proton Synchrotron(PS)

Figure 2.1 shows a schematic view of 12GeV Proton Synchrotron. The proton beam is extracted to the neutrino beam-line from the "EP1" beam channel.

Protons are accelerated by the following procedures:

- extraction of negative ions from an ion source,

- acceleration by a 750keV Cockroft-Walton Accelerator,

- acceleration by a 40MeV Alvarez-type LINAC,

- conversion of negative ions to positive ones with a carbon film,

- acceleration by a 500MeV Rapid-Cycle Booster Synchrotron,

- acceleration by the 12GeV Proton Synchrotron.

Accelerated protons are extracted from the 12GeV PS in a fast extraction mode (Repetition:2.2sec, Spill:1.1μsec). The micro-structure inside a single spill corresponds to the harmonic number of the main ring which is 9. As shown in Fig. 2.2, we can observe this micro-structure using Current Transformers(CTs: which we describe later) after extraction.

For more details, see [44, 42].

2.1.2 Primary Proton Beam Transport Line

We have a kicker magnet for the fast extraction at the extraction point of the accelerator. Kicker, septum, and bump magnets lead the proton beam to the neutrino beam-line [42]. Figure 2.3 shows the neutrino beam-line after the extraction.

The proton beam direction is toward the north just after the extraction point and it must be bent towards Kamioka employing the results of survey (about 90° to the west). An arc
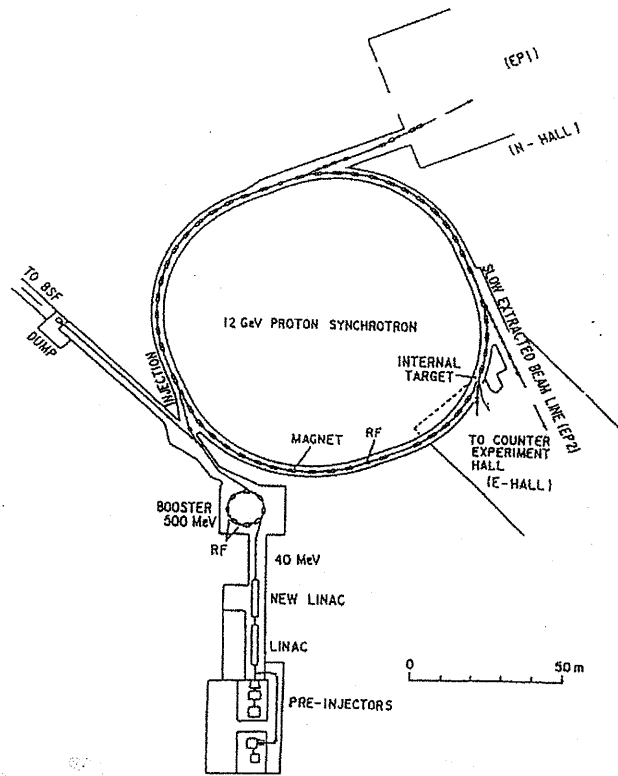
Figure 2.1: Schematic view of the 12GeV Proton Synchrotron
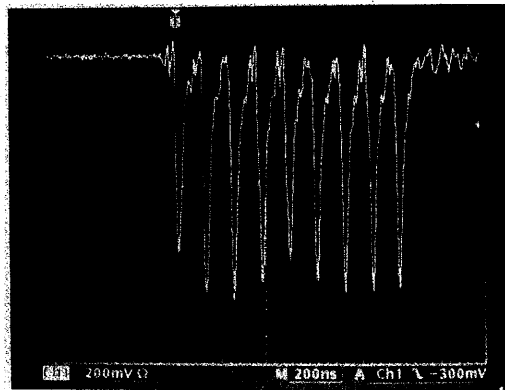
Figure 2.2: Oscilloscope picture of the micro-structure in the beam
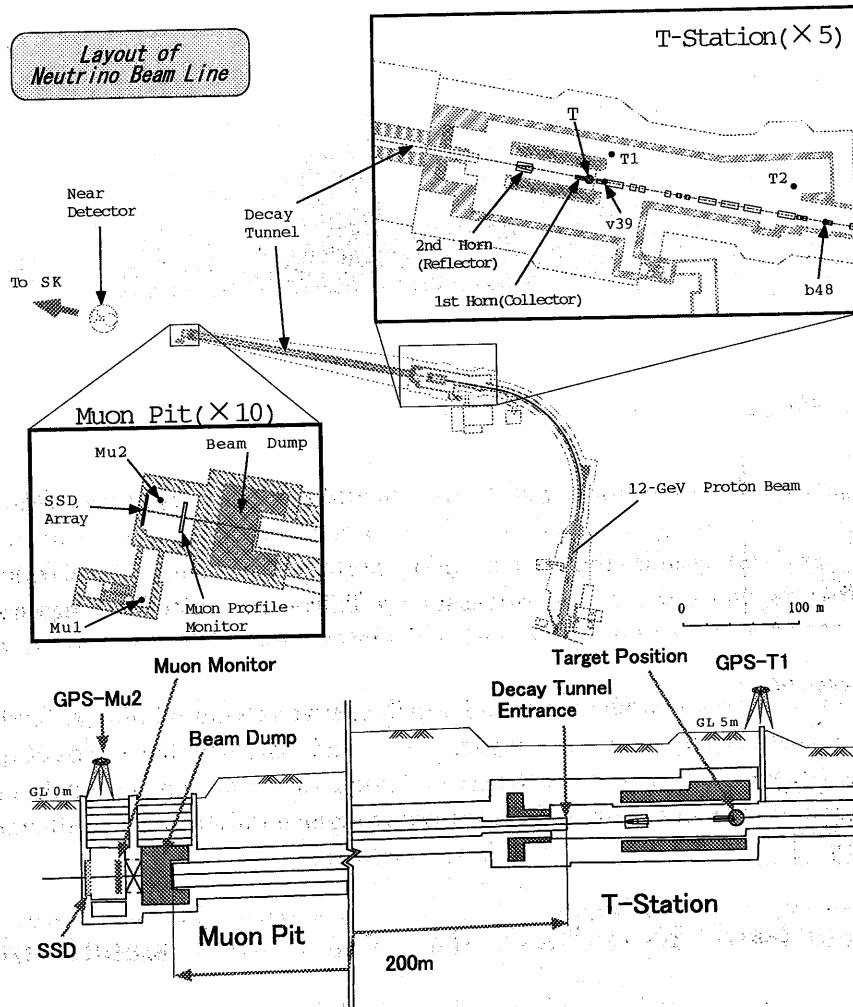
Figure 2.3: Schematic view of the neutrino beam-line and near detector, after 12GeV-PS

section of the beam-line, which is consists of 18 bending magnets and 18 quadrupoles, meets that request.

The target station was built after the arc section. The proton beam is finally focused on the neutrino production target at the target station. A steering magnet is placed just before the target to direct proton beam to SK, about 1° downward from the level of the production target (Fig. 2.4).
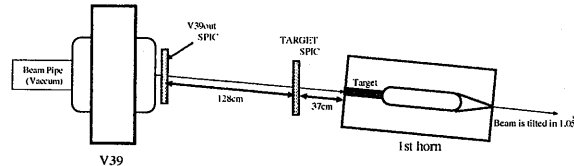
Figure 2.4: A schematic view of the SPICs, between the last magnet and the target

We use TRANSPORT[45] and DECAY-TURTLE[46] program to optimize the beam-line optics [40]. Thanks to this optimization, the actual transport efficiency of this beam-line is about 85%.

2.1.3 Horn Magnets and Target

There are two magnetic horns in the target station to efficiently focus the pions, the parent particles of neutrinos. Figure 2.5 shows the schematic view of the two magnetic horns. The first horn has dimensions of 2.37m in length, and 0.70m in diameter. On the other hand, the second horn has dimensions of 2.76m in length and 1.65m in diameter, located 8m downstream of the first horn. It is needed to efficiently increase the neutrino flux in the forward direction since the momentum distribution of the secondary pions is wide (from 0 to 10GeV/c).

Due to the low-energy feature of our experiment, our design is such that the target is inside the 1st horn in order to focus pions more efficiently. The horns and the target are made from aluminum alloy. The target is 66cm long and 20mm in diameter in June 1999, 30mm since November 1999. This length corresponds to 1.5 interaction lengths. A MC simulation shows almost all protons interact[1] with the target thanks to the magnetic field inside the horn.

In contrast, other parts of the horn through which the secondary particles pass, are required to be as thin as possible in order to minimize the absorption losses of pions. Thus we designed and manufactured horns carefully so as to have mechanical strength enough to stand the electromagnetic force and thermal expansion.

We drive the horns every 2.2s with a 2ms long 250kA pulsed current illustrated in Fig. 2.6. We need to synchronize them with the fast extracted beam (1.1μs bunch width) to generate the toroidal magnetic fields with respect to the beam axis [47]. We cannot use DC current because no power supply can provide 250kA even if such a power supply exists, the horns could not dissipate the heat.

According to the calculation, the strength of the magnetic field B(kGauss) at R(cm) distance from beam center is given by;

---

[1]include elastic scattering
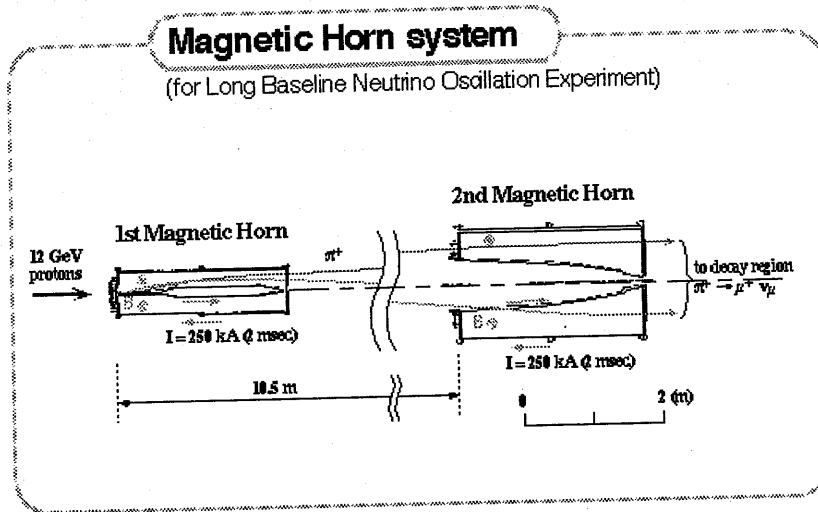
Figure 2.5: Schematic view of the horns.
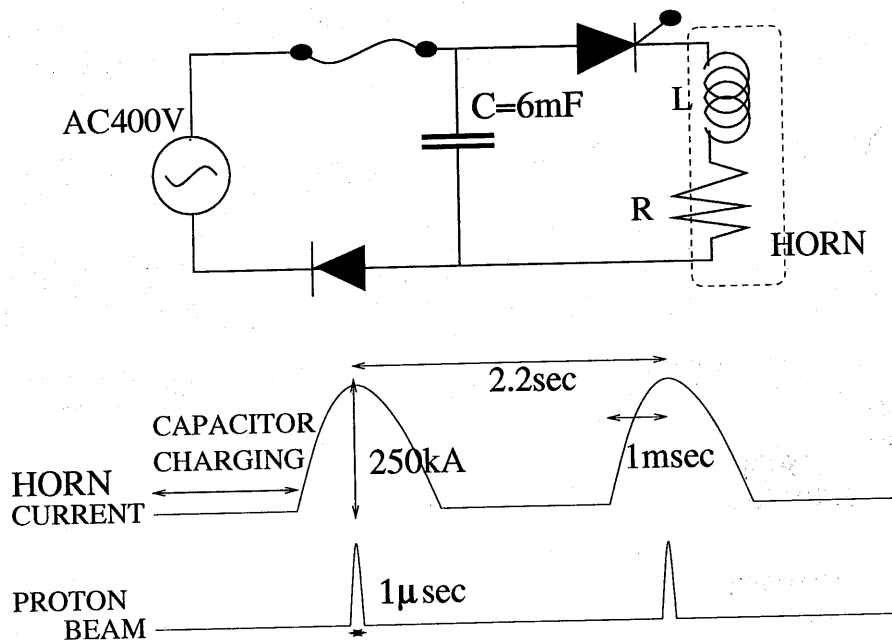
Figure 2.6: The pulsed current supplied to horn magnets[48]

$$B = \frac{I}{5.0 \cdot R},$$ (2.1)

where I is the current supplied to the horn magnets in units of kA. Hence we have 50kGauss at R=1cm. (This formula is valid in the air part of horn)

Fig. 2.7 shows the capability of our horn system. The Shaded region shows the MC simulated neutrino flux at SK with the horn current of 0A, and the histogram shows that of 250kA (target is 30mmϕ). The simulated neutrino flux above 0.5GeV supplying 250kA current supplied to the horn magnets is about 22 times more than the null current case.
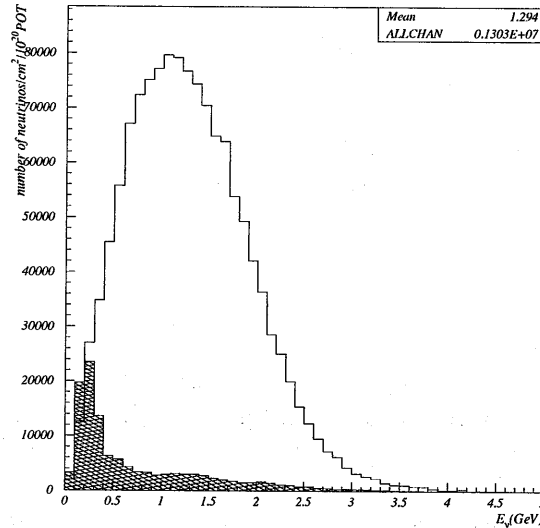
Figure 2.7: Performance of our horn system. The shaded (solid) histograms show the MC simulated neutrino flux at SK with the current supplied to the horn magnets of 0kA (250kA), where the target diameter is target is 30mmϕ

Various measurements have been made to understand the characteristics of this horn system. For example, magnetic field measurements using a pick-up coil, performance test of the cooling system, and so on. These are summarized in [48, 49].

We must take into account difference in beam conditions in June 1999 and since November 1999 because our 1st horn was changed. We increased the diameter of the target part of the 1st horn from 20mmϕ to 30mmϕ in order to strengthen the weakest part against the electromagnetic force. Accordingly we could also increase the current supplied to the horn magnets from 200kA to 250kA thanks to this modification.

2.1.4 Decay Tunnel

The lifetime of pion: 2.6×10^{-8}s ($c\tau = 7.8$m) becomes longer by a Lorenz factor.

In order to make pions decay to neutrinos efficiently, we designed a 200m-long decay tunnel which has a radius of 0.75, 1.0 and 1.5m. Figure 2.8 shows the schematic view of the decay pipe of this experiment.
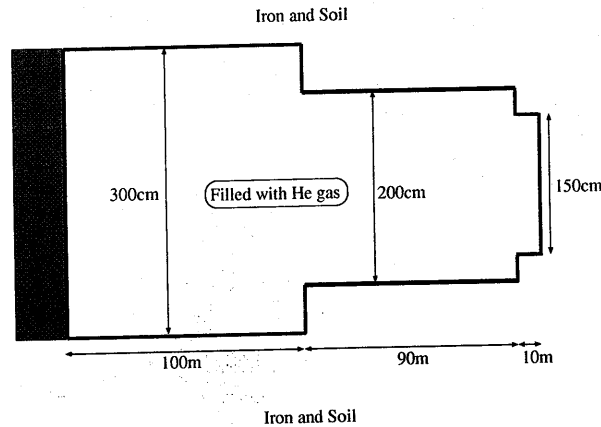
Figure 2.8: Schematic view of the decay pipe.

The decay pipe is filled up with helium gas because the interaction length of helium gas is about 5 times longer than air. (Interaction length of helium: 3.64km(STP), that of Air: 0.731km(STP)). It is also important to reduce the number of neutrinos produced in the gas which may cause uncertainty in this experiment.

2.1.5 Primary Beam Monitors

Current Transformer (CTs)

CT is a kind of pick-up coil sensitive to the beam current. The schematic view of CT is shown in Fig. 2.9.
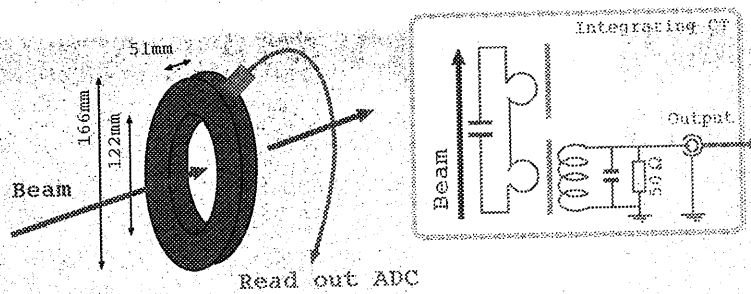
Figure 2.9: Schematic view of the CT

There are 13 CTs in the primary beam-line (Table 2.1). They are used as proton beam

intensity monitors at various points. Comparison among these CT values gives information on the transport efficiency (= down stream intensity/ upstream intensity). The efficiency is typically ~85% from the extraction point to the target.

Each CT is calibrated using pulse current and beam as well. The absolute number of protons is measured within 10% error.

CT located just before the target (called "CT16") monitor the number of protons on the target delivered to generate the neutrino beam. Figure 2.10 shows the integrated protons on the target (POT) as a function of time since May 1999 till June 2000. The total number of protons used for the analysis at the far site, Super-Kamiokande, is 2.29×10^{19}POT@.
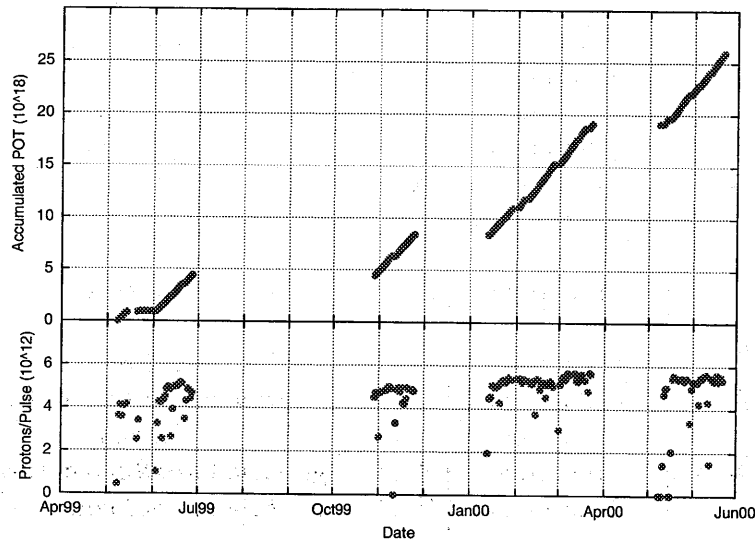
Figure 2.10: (Upper) Integrated number of protons on the target since May 1999 till June 2000. (Lower) Intensity of the proton beam at the target in the unit of protons per pulse (ppp).

Segmented Plates Ionization Chambers (SPICs)

SPICs are used for the profile measurement of the primary protons. There are 28 SPICs in the beam-line from the extraction point to the entrance of the decay pipe (Table 2.1). The principle of ionization chambers is shown in Fig. 2.11

Filled gas in the detector is ionized by radiations. Ionized electrons (or positively charged ions) are collected at the anode (or cathode). Finally collected electrons (ions) make an electric signal. General properties of ionization chambers are described in [50].

The SPICs used in K2K have segmented anode to measure the particle density shown in Fig. 2.12.

It consists of three copper sheets. The central one is for the anode plane (-HV), and the others are for horizontal and vertical readout cathode (GND) planes. The readout planes have 32 channels for x and y readout. As the proton beam directly hits this chamber, the copper sheet is made as thin as possible, 28μm. Most of(26 out of 28) the chambers have a 5mm pitch
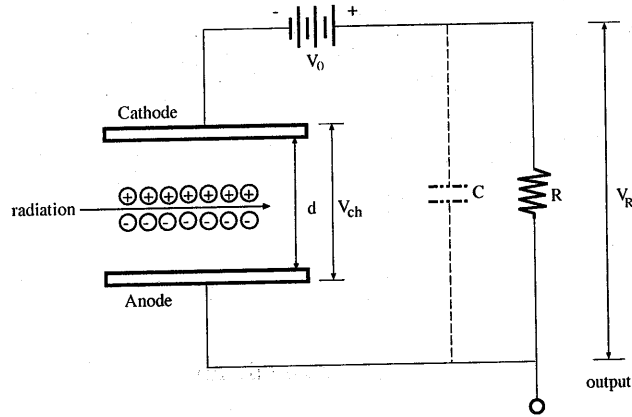
Figure 2.11: The principle of the ionization chamber
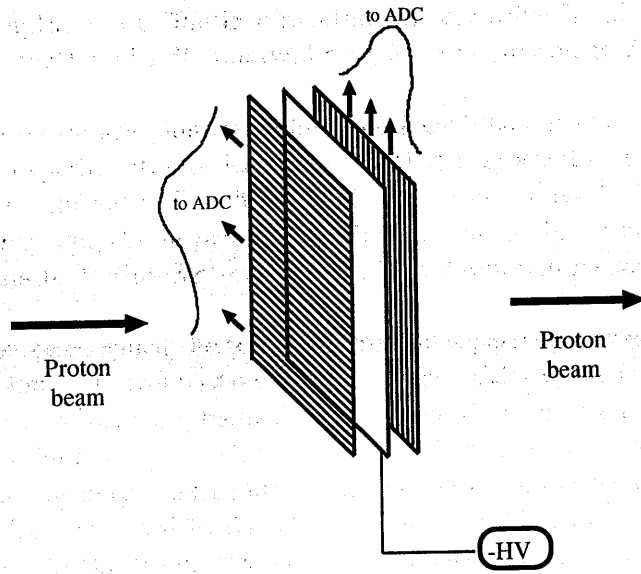
Figure 2.12: Schematic view of the SPIC used in K2K.

strip, except for one chamber before the target which has a 1.27mm pitch, and for one chamber before the decay pipe which has a 2cm pitch. These monitors are quite useful for the steering of the proton beam. The SPICs used in KEK are described in [51].

Figure 2.13 shows the online display for beam-line monitors. English characters show the monitor name; i.e. "V39 out" stands for the monitor located downstream of the 39th vertical dipole magnet. Table 2.1 summarizes the location and type of the beam-line monitors.
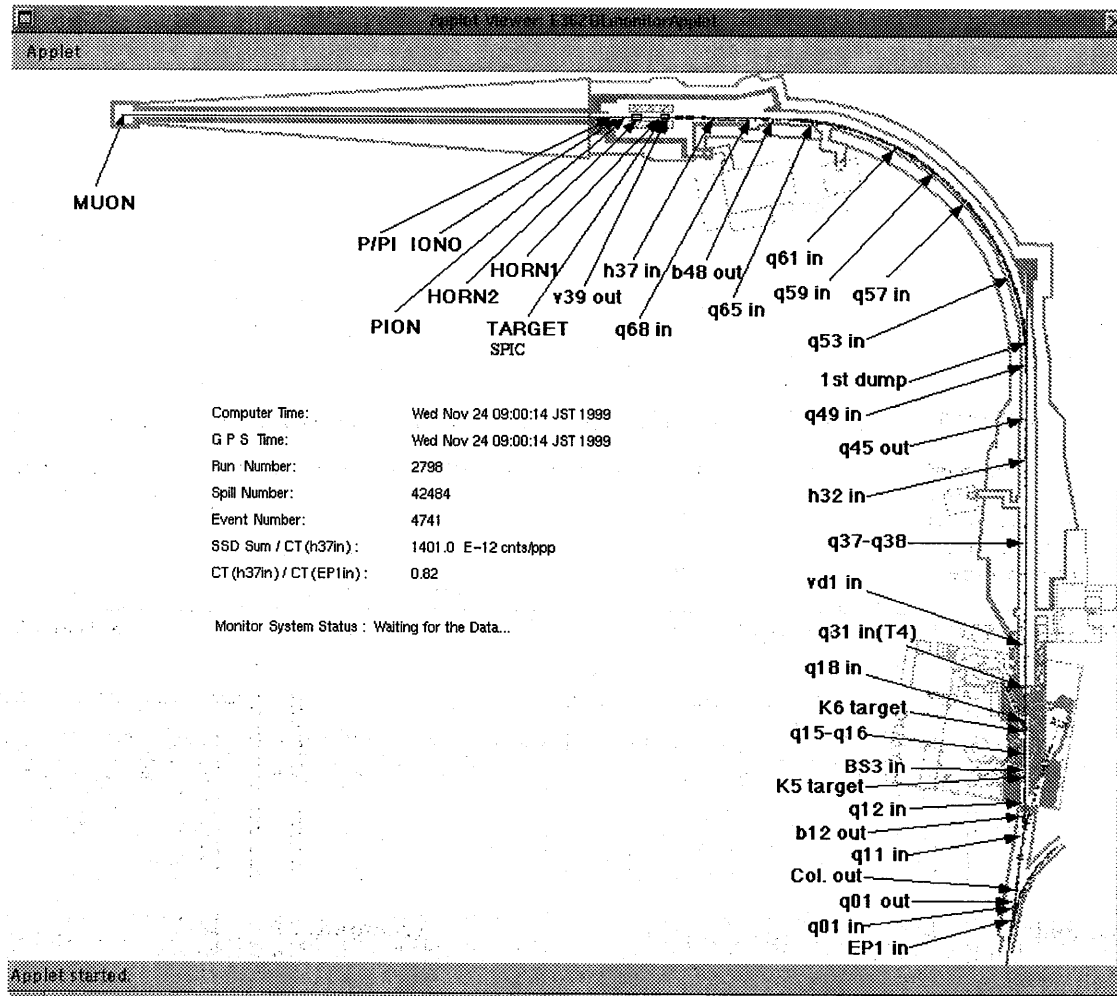
Figure 2.13: Monitors in the neutrino beam-line

2.1.6 Secondary Beam Monitors

Pion Monitor (PIMON)

The pion monitor (PIMON) is a gas Cherenkov detector set just behind the second horn. Cherenkov light generated in fluorine gas(R-C318) is reflected by the pie-shaped spherical

Characters	monitor type	purpose	comment
EP1 in	CT,SPIC	intensity monitor and steering	5mm pitch
q01 in	SPIC	steering	5mm pitch
q01 out	SPIC	steering	5mm pitch
Col. out	SPIC	steering	5mm pitch
q11 in	CT,SPIC	intensity monitor and steering	5mm pitch
b12 out	SPIC	steering	5mm pitch
q12 in	CT,SPIC	intensity monitor and steering	5mm pitch
K5 target	CT,SPIC	intensity monitor and steering	5mm pitch
BS3in	SPIC	steering	5mm pitch
q15-q16	SPIC	steering	5mm pitch
K6 target	SPIC	steering	5mm pitch
q18 in	SPIC	steering	5mm pitch
q31 in	SPIC	steering	5mm pitch
vd1 in	CT,SPIC	intensity monitor and steering	5mm pitch
q37-q38	SPIC	steering	5mm pitch
h32 in	CT,SPIC	intensity monitor and steering	5mm pitch
q45 out	SPIC	steering	5mm pitch
q49 in	CT,SPIC	intensity monitor and steering	5mm pitch
q53 in	CT,SPIC	intensity monitor and steering	5mm pitch
q57 in	SPIC	steering	5mm pitch
q59 in	CT,SPIC	intensity monitor and steering	5mm pitch
q61 in	SPIC	steering	5mm pitch
q65 in	CT,SPIC	intensity monitor and steering	5mm pitch
q68 in	SPIC	steering	5mm pitch
h37 in	CT,SPIC	intensity monitor and steering	5mm pitch
v39 out	SPIC	steering	5mm pitch
target SPIC	CT,SPIC	intensity monitor and steering	1.27mm pitch
HORN1, HORN2	slow monitor	monitor horn current	
PION	Cherenkov counter	measure pions	described later
IONO	Ion Chamber	measure secondary particles	
P/PI	SPIC	measure secondary particle profile (projection)	2cm pitch
MUON	SI + IC	measure muon direction and intensity	described later

Table 2.1: Locations of beam-line monitor. Please refer to 2.13.

mirror on the beam line and then goes to a photo device composed of 20 photo-multiplier tubes(PMT). Figure 2.14 gives a schematic view of the pion monitor.
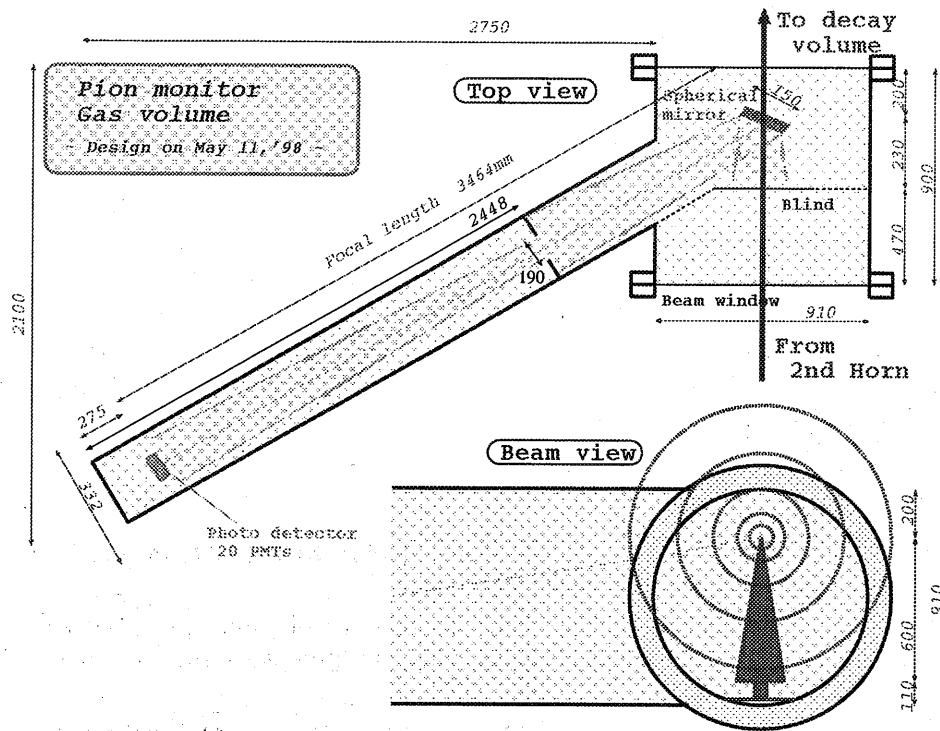
Figure 2.14: Schematic view of the pion monitor (PIMON).

We measure the pion momentum distribution and divergence just after the target from the distribution of Cherenkov light photons. We can estimate the energy spectrum of the neutrino beam both at the near site and at the far site, Super-Kamiokande, from the decay kinematics of the pions. Figure 2.15 shows the energy spectrum and the far to near flux ratio predicted by PIMON analysis in the Novermber configuration. Details of the analyses are described in [100].

Muon monitor (MUMON)

The muon monitor (MUMON) is placed 200m downstream from the target. This information immediately gives us the direction of the neutrino beam. This is an ionization chamber similar to SPIC. However, the muon yield is only (a few) $\times$ 10^4/cm^2 level. To compensate for this small yield within the ionization chamber, large pads (5cm$\times$5cm) are placed in the inside chamber.The position resolution of the muon monitor is 5cm for the muon profile.

Additionally, silicon pad detectors (SPD) are placed in the muon dump room. They also measure the muon profile for confirmation of the MUMON measurement. The SPD is composed of 18 small silicon pads and 8 large silicon pads. The smaller pad detector is 1cm $\times$ 1cm in size, the larger one is 5cm $\times$ 5cm. Each silicon pads are arrayed as in Figure 2.17.
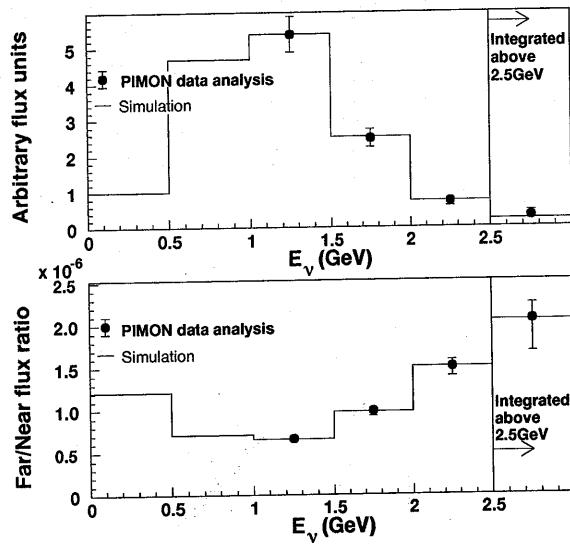
Figure 2.15: The energy spectrum at the near site(upper) and the far site(lower) predicted by the pion monitor in the November configration.
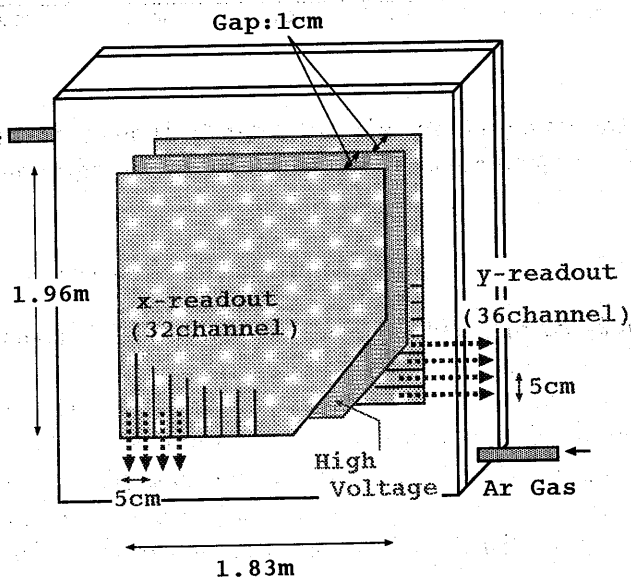
Figure 2.16: Schematic view of the muon monitor.
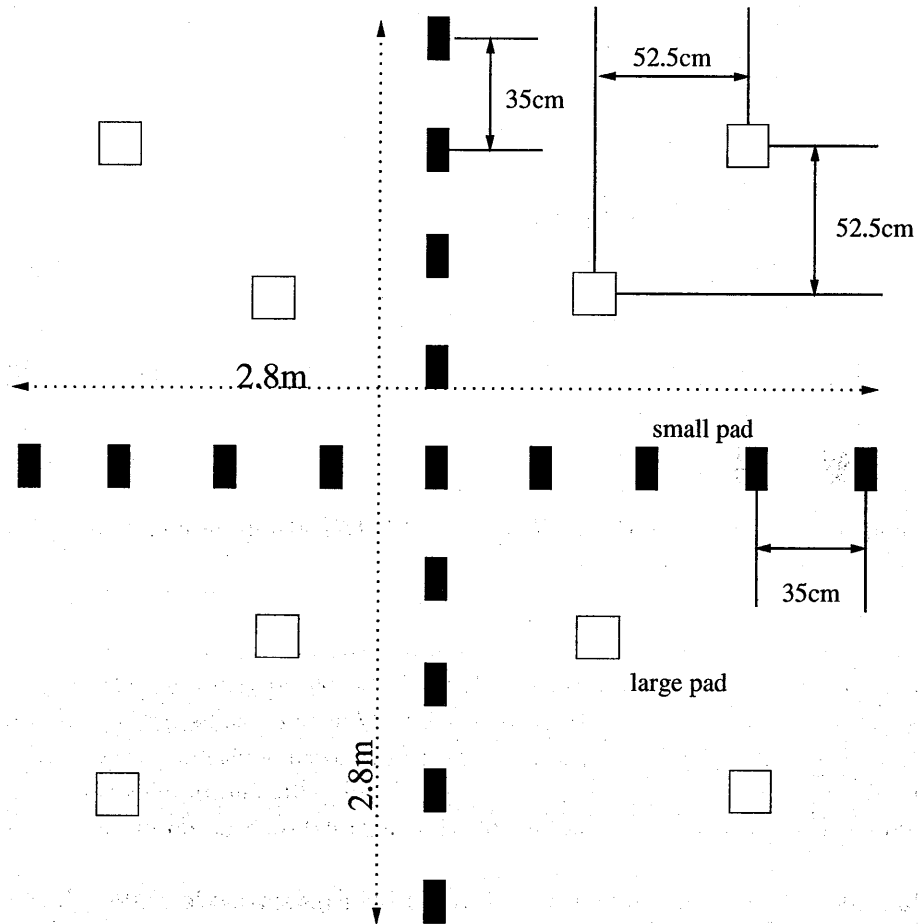
Figure 2.17: Configuration of the silicon pad detectors.

2.2 Super-Kamiokande(SK) Detector

Super-Kamiokande detector is located at the Kamioka Observatory of Institute for Cosmic Ray Research, the University of Tokyo, in the Kamioka mine of Gifu Prefecture, Japan. The latitude and longitude are 36° 25'N and 137° 18'E, respectively. It lies at a mean overburden of the 1000 m thickness of rock, which is equivalent to 2700m of water, below the peak of Mt. Ikenoyama, and the detector site is about 2km away horizontally from the entrance of the mine. There is rich natural underground water flowing near the detector site and it is used as the bases of pure water filled in the Super-Kamiokande detector. The temperature in the mine is about 10 °C, and stable all throughout the year. The main purpose of this experiment is to observe several types of neutrinos (atmospheric neutrinos, solar neutrinos and supernova neutrinos) and to search nucleon decays which are predicted by the Grand Unified Theories (GUTs). The Super-Kamiokande experiment started taking data on April 1 1996 and continued taking data up to now without any serious trouble.

2.2.1 Detection method

Super-Kamiokande is an imaging water Cherenkov detector. It detects Cherenkov light photons generated by charged particles which propagate in water. Cherenkov light photons are emitted when the velocity of a charged particle exceeds the light velocity in the medium (c/n), where c is the light velocity and n is the refractive index of the medium (in the case of water, $n = 1.33$). The threshold momenta for the Cherenkov radiation are 0.58, 120, 153 MeV/c for electrons, muons, pions, respectively.

The Cherenkov light is emitted in a cone of half angle θ toward the direction of the particle track. This θ is called the Cherenkov angle and determined as follows:

$$\cos\theta = \frac{1}{n\beta},$$ (2.2)

where $\beta = v/c$ and θ is about 42° for a relativistic charged particle in water. The spectrum of the Cherenkov light as a function of the wavelength λ is expressed as follows:

$$\frac{dN}{d\lambda dx} = \frac{2\pi\alpha}{c}\left(1 - \frac{1}{n^2\beta^2}\right)\frac{1}{\lambda^2},$$ (2.3)

where α is the fine structure constant and x is the track length of the charged particle. About 390 photons/cm are emitted in water in the wavelength region 300nm $\sim$ 700nm, to which the photo multiplier tubes are sensitive.

2.2.2 Detector features

As shown in Fig. 2.18, the Super-Kamiokande detector is a cylindrical water tank whose size is 41.4 m in height and 39.3 m in diameter, instrumented with photomultiplier tubes (PMT), electronics and online data acquisition systems and a water purification system. The water tank is made of stainless steel and contains 50000 tons of pure water. The detector has two PMT layers, called the inner detector (ID) and outer detector (OD), and the outer detector surrounds the inner detector completely.
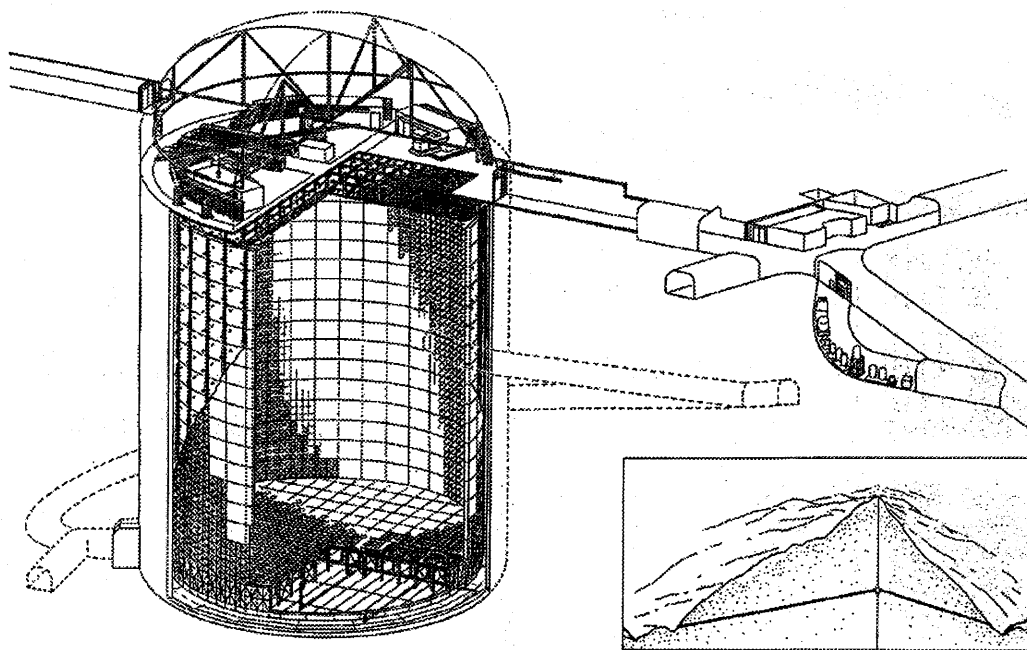
Figure 2.18: Schematic view of the Super-Kamiokande detector
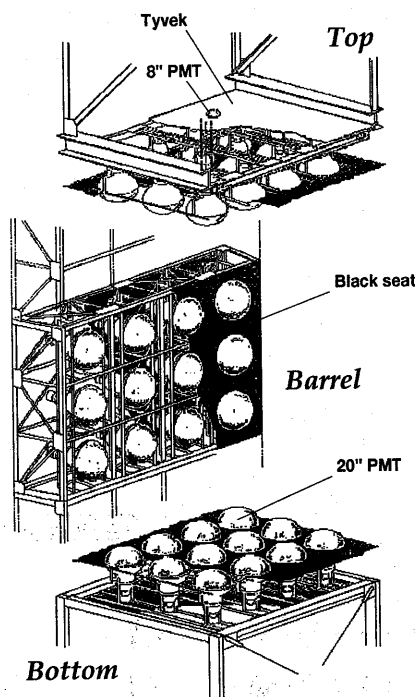
Figure 2.19: Schematic view of the frame which supports PMTs

The diameter, height and total mass of the inner detector are 33.8 m, 36.2 m, and 32 kton, respectively. 11146 20-inch-in-diameter PMTs are used for the inner detector. 7650 PMTs are attached to side wall and the rest are on the top and bottom walls. The PMTs are placed at intervals of 70 cm grid and the gaps are lined with black polyethylene terephthalate sheets, which are called "black sheet". The photocathode coverage is about 40%.

The outer detector surrounds the inner detector completely and its thickness is 2.0 m for the side and 2.2 m for the top and bottom. It is instrumented with 1885 8-inch-in-diameter PMTs and each PMT has a 60cm × 60cm square collar plate of wavelength shifter to increase the light collection efficiency. Tyvek sheets which are known as a reflective material cover the inner surface of OD to further enhance the light collection efficiency. The outer detector plays an important role of reducing backgrounds. It is used as a veto-counter which identifies incoming cosmic-ray muons. Also, the water of 2 m thickness in the outer detector shields against gamma-ray and neutron backgrounds from the surrounding rock.

These two detector volumes are optically isolated from each other by black sheets and Tyvek sheets as shown in Fig. 2.19.

2.2.3   Photomultiplier tube

The photomultiplier tubes (PMTs) 20-inch in diameter were originally developed by Hama-
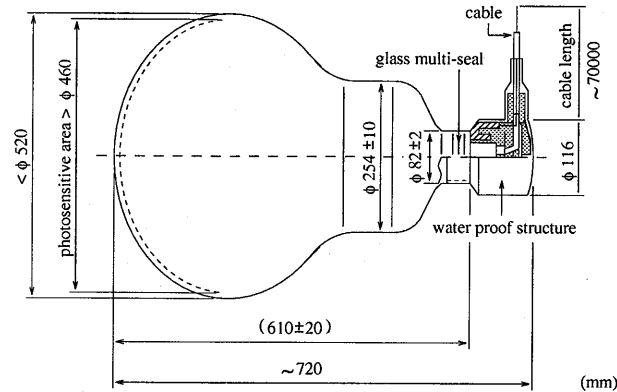
Figure 2.20: Schematic view of 20-inch PMT used in the inner detector (Hamamatsu R3600).

matsu Photonics Company in cooperation with members of Kamiokande [111]. The 20-inch PMTs used in Super-Kamiokande (Hamamatsu R3600) have some improvements over those used in Kamiokande. The size and shape of this PMT is shown in Fig 2.20. The photo-cathode is made of bialkali (Sb-K-Cs) that is suited for the collection of Cherenkov light. The quantum efficiency is shown in Fig 2.21 is 21 % at the wave length $\lambda = 400$nm which is the typical wave length of Cherenkov light.

A Venetian-blind type dynode is used and the bleeder resistor-chain is optimized in order to achieve good timing response and collection efficiency of photoelectrons. The average collection efficiency is more than 70%. The one photo-electron peak can be seen clearly as shown in Fig 2.22. The transit time spread is about 2.5nsec for single photo-electron (p.e.) signal [112]. The PMT have a uniform response under the condition that the geomagnetic field is suppressed to 100 mG. The geomagnetic field inside the tank is kept less than 100 mG based on the field compensation by 26 sets of Helmholtz coils which surround the detector. The average dark noise rate is about 3.1 kHz at discriminator threshold of 0.2 p.e. and the average PMT gain is about 10^7 when 2000 Volt is supplied.

The PMT used in the outer detector is 8-inch-in-diameter Hamamatsu R1408 PMT, which is recycled from the IMB experiment. The size of wavelength shifter which collars the outer PMT is 60cm on each side and 1.3cm thick. It absorbs ultraviolet light and re-radiates blue light to which the PMT is the most sensitive. Consequently, the light collection efficiency increases by 60% [113]. The timing resolution of the PMT is about 11 nsec, and after fitting wavelength shifter, it degrades to more than 15 nsec. Nevertheless, it is enough for tagging the events.

2.2.4 Electronics for inner detector

Figure 2.23 shows the electronics system used in the inner detector. The system has two types of modules, TKO(TRISTAN/KEK Online) modules [114] and VME modules. These are
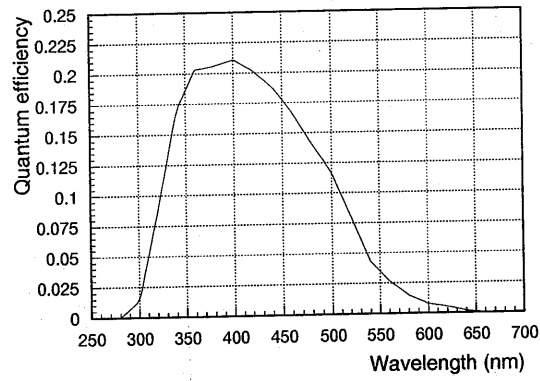
Figure 2.21: Quantum efficiency of 20-inch PMT as a function of wavelength of photons
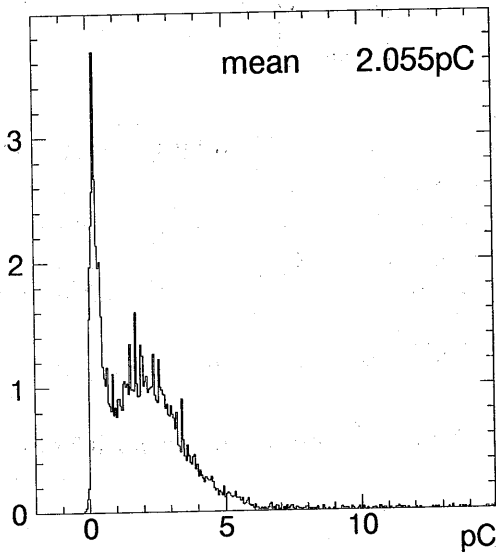
Figure 2.22: One photoelectron distribution measured by 20-inch PMT

48 TKO and 8 VME crates in total and they are distributed in 4 electronics huts. Additionally one VME module for the global trigger (TRG module) is located in the central hut.

Initial process of the PMT signals is done by the TKO modules. This system consists of 48 TKO crates, each of which up to 20 Analog Timing Modules (ATMs) [115], one Go/NoGo (GONG) trigger module and one Super-Controller Header bus interface (SCH) module.

A total of 934 ATMs are used for the inner detector and each ATM has 12 PMT input channels. The ATM provides a 1.2 μsec full range in time with 0.3 nsec resolution and 550 pC full range in charge with 0.2 pC resolution. Each channel has a pair of switching time-to-analog converters (TAC) and charge-to-analog converters (QAC) to measure the time and charge of an input pulse. These pair of switching channel is called "A" and "B" respectively and they realize the continuous, dead-time free data acquisition, for example, for a stopped muon and a decay electron accompanied to it.

Each channel in the ATM has an amplifier with a gain of 100 and a discriminator. The threshold is set to 100mV which is equivalent to about 1/4 p.e., and when input signal exceeds this threshold, a rectangular pulse (200 nsec width and 11mV height) is generated. The rectangular pulses from the all the hit PMTs are added up ("HITSUM" signal) and sent to the global trigger module in the central hut and simultaneously a gate window of 900 nsec width is opened to start time measurement in TAC and charge accumulation in QAC. QAC accumulates charge in the 400 nsec time window and keeps it until the global trigger arrives. If the global trigger does not arrive within 1.3 μsec , the stored information in TAC and QAC is cleared. On the contrary, when the global trigger arrives, charge and timing information is digitized by ADC and sent via SCH to the memory (SMP) in the VME module.

Pedestals of ATMs are measured every 30 minutes. Only 1/8 of all the ATMs are measured at once in order not to miss supernova events.

2.2.5   Electronics for outer detector

The electronics system used in the outer detector is constructed by the collaborators from U.S. universities and systematized independently of that of the inner detector. Fig 2.24 shows the front-end modules for the quadrant electronics system. It consists of 40 paddle cards, 10 charge-to-timing converters (QTCs) modules , 5 time-to-digital converter (TDCs) and one FASTBUS smart crate controller (FSCC).

The paddle card has 12 PMT channels. The signal and high voltage lines are AC coupled and the paddle card has a role to pick off the PMT signals through a high voltage capacitor.

The QTC module converts a PMT signal into a logic pulse (ECL level), the leading edge of which corresponds to the arrival time of signal and the width is proportional to the integrated charge of PMT pulse. The QTC module also provides a HITSUM signal (200 nsec, 20mV rectangular pulse) and send it to the trigger module in the central hut.

The LeCroy model 1877 Multi-hit Time-to-Digital Converter is used for the TDC modules of the outer detector and it has up to 96 ECL level inputs per one module. The least bit counting accuracy of the TDC modules is 0.5 nsec. The TDC module serves as a pipeline buffer within 32 μsec and digitize 16 of the most recent signals and stores in the memory. The time window was set to the full 32 μsec centered around the trigger time in the early period of the operation, but in September 1996, this width was cut to 16 μsec (trigger time is 10 μsec
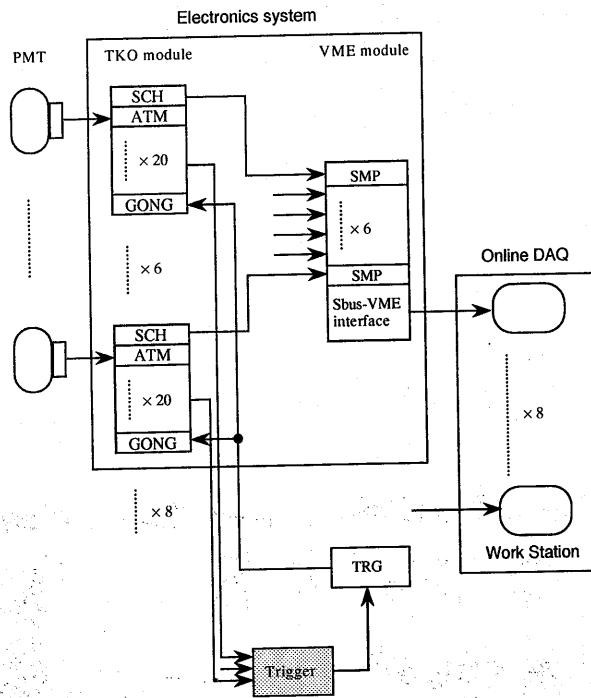
Figure 2.23: Inner detector data acquisition system
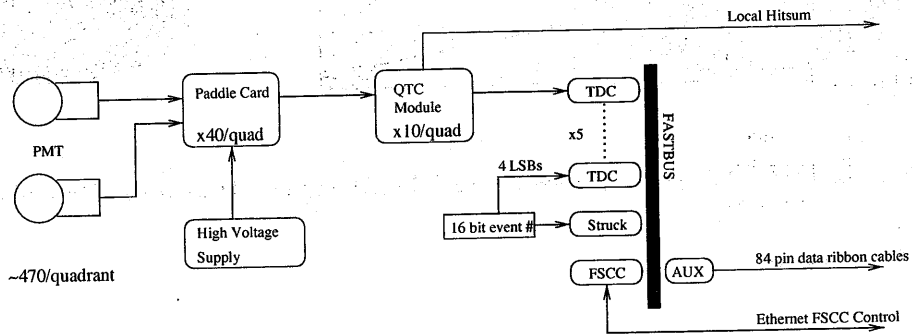
Figure 2.24: Outer detector acquisition system

after opening the gate) in order to reduce the amount of data. The control and read-out of the TDC modules are given by FSCC and the stored data are sent to the online machines.

2.2.6 Trigger

The Super-Kamiokande detector has 3 triggers for the inner detector, which are named as High energy trigger (HE), Low energy trigger (LE) and Super Low energy trigger (SLE), and 1 trigger for the outer detector, Outer detector trigger (OD). Each of them is triggered by its own level of HITSUM signal independently.

The HE trigger is used mainly to identify K2K-beam neutrinos, cosmic-ray muons, atmospheric neutrino and proton decay candidates. It requires a coincidence of 31 HITSUM signals within 200nsec time window and the trigger rate is about $5 \sim 6$ Hz.

The LE trigger is used for solar neutrino analysis above 5~6 MeV in the energy and its threshold is 29 HITSUM corresponding to 5.7 MeV.

The OD trigger is used for the rejection of the cosmic-ray muons. It is formed by the coincidence of 19 HITSUM signals from the QTC modules in the outer detector. If the OD trigger is generated, the trigger signal is sent to the TRG modules.

The SLE trigger started from May-1997 in order to push the the analysis threshold of solar neutrino energy spectrum down to 4.6 MeV. The computer upgrade and the increase of the network speed make it possible. The SLE triggered events are not used at all in the K2K experiment and removed at the first step of the data reduction.

The global trigger is generated independently when any of these four trigger is generated, and the data stored in memory modules is read through online workstations.

2.2.7 High Voltage System

The high voltage (HV) power supply system is composed of HV modules (A933K), intelligent mainframes (SY527) and the VME interface modules (V288) which are made by CAEN Co. In Super-Kamiokande, about 480 A933K modules and 1 primary HV generator. The output voltage (maximum HV drop of 900V from the primary HV) of each channel is set and monitored (0.2V resolution) individually and the primary HV generator has a current monitor ($1\,\mu$A resolution). Therefore, one can set and monitor the output voltage of each channel and monitor output current of each module. Typically 10 A933Ks are accommodated in a SY527 crate which is controlled remotely via a V288 module (VME↔CAENet interface).

2.2.8 Data acquisition and offline system

The data acquisition system consists mainly of 8(1) slave workstations for collecting data of the inner(outer) detector and 1 host workstation for controlling run status and collecting data from the 9 slave workstations. The host workstation provides the graphical interface for shift workers to control run status, and sends commands to each slave workstation via socket according to the requirement of shift workers. Each slave workstation reads out the data from electronics modules when the global trigger is generated, and transfers it to the host workstation via FDDI network. The host workstation concatenates all the information of hit PMTs for both inner and outer detectors, and records as one event.

The data, which are built as an event in the host workstation, are passed to the offline system. First, the format of data is changed to "ZEBRA" format which is easy to handle and store additional information. The sequence of data is separated into a data file in every ten minutes, the data size of which corresponds to about 50 M Bytes. This reformatted data is transferred from the detector site to the offline computer facility out of the mine, and stored to the magnetic tape library. At the same time, the data are transfered to the recalibration process which is called "TQREAL" and the primary reduction process. In the TQREAL process, the timing and charge information of PMTs are converted from ADC and TDC counts to units of photoelectron and nanosecond, respectively, take account of the pedestal values and the calibration constant. Several primary reductions for the different physics, including the K2K first reduction, run in parallel with a total of 20 CPUs in order to process a large amount of data speedily. The reduced data are also stored to the tape library and the subsequent proper reduction is processed by each analysis group.

2.2.9   Water purification system

The 50000 ton of pure water is filled in the Super-Kamiokande detector it was produced from the natural underground water flowing near the detector site and filled up into the detector. The water purification system circulates 50 m^3 of pure water per hour to keep its quality. The instruments to constantly monitor the water quality are installed in various places. The purpose of the water purification is to remove the radioactive materials and bacteria int the water and keep high water transparency high.

Figure 2.25 shows the water purification system. The solid line shows the main circulation of water and the dotted line shows the supplementary circulation line. The heat exchanger keeps the temperature of water about 13 °C to suppress the bacteria growth. The ion exchanger and cartridge polisher remove metal ions such as Ra,U and Th in the water. The ultra-violet sterilizer kills bacteria in the water. The gas in the water, such as oxygen and radon, is removed by the vacuum degasifier and finally the ultra filter (UF) removes the finest dusts with diameter of the order of 10 nanometers.

After the water purification, the concentration of radon, which is $10^4 Bq/m^3$ in the mine primary water, is reduced to $< 10 mBq/m^3$ and the light attenuation length is kept to about 100 m at wavelength of 420 nm.

SUPER-KAMIOKANDE WATER PURIFICATION SYSTEM
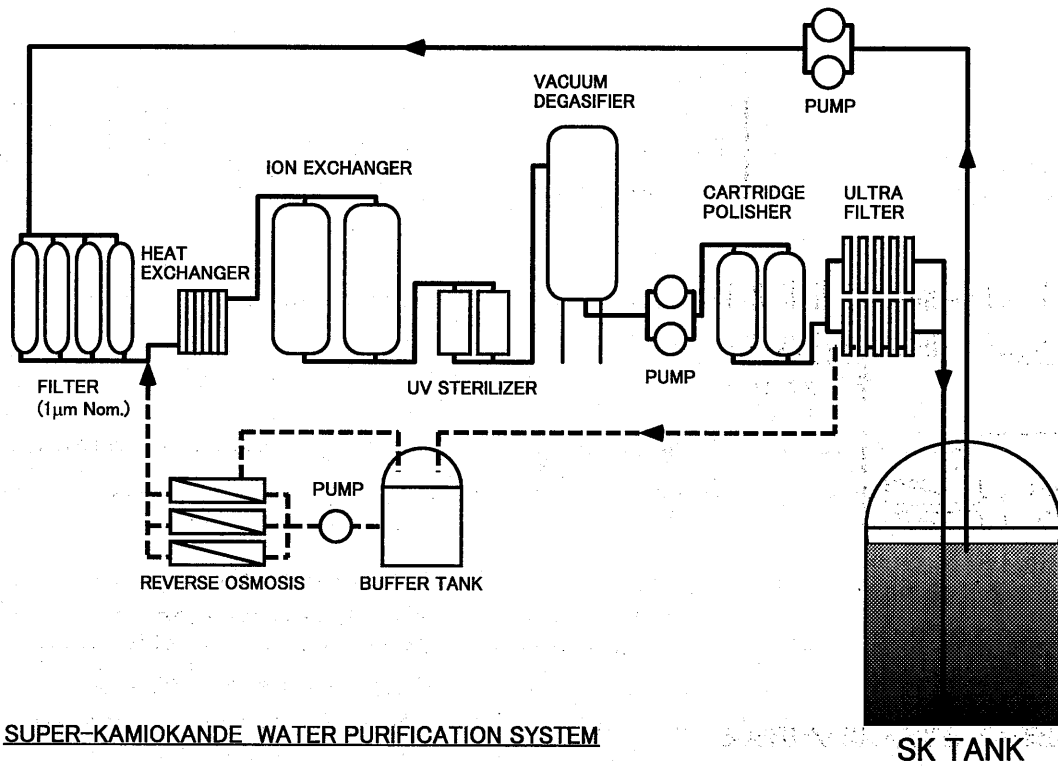
Figure 2.25: Water purification system.

2.3 Near Neutrino Detectors

The near neutrino detectors are located 300m downstream the target. The experimental hall accomodating the near detectors is 24 meter in diameter and 16 meter in depth underground.

There are 2 near detectors in the experimental hall as shown in Fig. 2.26. One is the
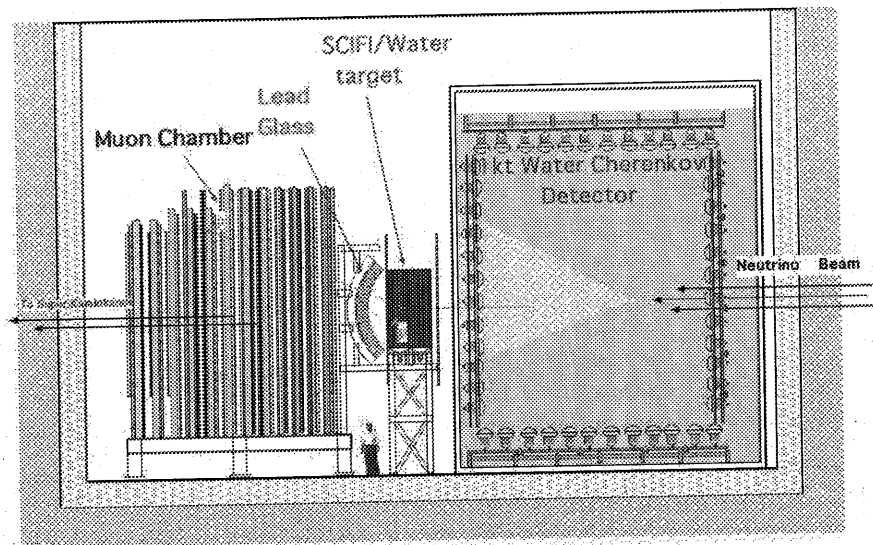
Figure 2.26: Schematic view of the near detectors

1kt water Cherenkov detector and another is the fine-grained detector which consists of 5 components, the Veto counter, the Scintilation Fiber tracker, the Trigger counter, the Lead Glass calorimeter and the Muon range chamber.

The chief aim of the 1kt water Cherenkov detector is to measure the neutrino flux at KEK to predict that at Super-Kamiokande 250km far from KEK. The fine-grained detector can measure the ν_e contamination in our ν_μ beam and measure neutrino-water cross section.

The detailes for each component is decribed below.

2.3.1 1kt Water Cherenkov Detector (KT)

A 1 kilo-ton water Cherenkov detector (KT) is constructed in the cylindrical cavity (25 m in diameter and 15 m in depth) dug out some 300 m downstream of the proton beam target at KEK. The principal motivation why we set KT is that we can cancel out the systematic uncertainties inherent to a water Cherenkov detector by measuring the neutrino beam properties before neutrino oscillations occur, as KT has the same target material (H_2O), detection principle, and analysis programs as in Super-Kamiokande. KT is, in a word, a baby Super-Kamiokande.

The cylindrical water tank, 10.8 m in diameter and 10.8 m in height, contains approximately 1000 tons of pure water. The water tank was originally used by the KEK-PS E261A

experiment[101, 102] which verified the e/μ identification programs employed in Kamiokande and is modified for this 1 kton detector. In the water tank, the inner detector (ID) and the outer detector (OD) are optically separated by black sheets. ID is a cylindrical water Cherenkov detector, 8.6 m in diameter and 8.5 m in height, equipped with 680 20 inch-in-diameter PMTs facing inwards on the ID surface. On the barrel, top, and bottom layers, mounted are 456 (38×12), 112, and 112 PMTs, respectively. The ID photocoverage 40 % (PMT spacing 70 cm) is the same as in Super-Kamiokande and the photoinsensitive ID surface is covered with polyethylene black sheets to prevent light reflection in ID and leakage to OD.

OD is also a water Cherenkov detector, 0.6 m (bottom) to 1 m (barrel) thick, viewed by 68 8 inch-in-diameter PMTs (PMT spacing=1.4 m) facing outwards on the detector surface. On the bottom and the barrel, mounted are 26 and 42 PMTs, respectively. The 42 barrel PMTs cover only beam-front 1/3 of the barrel part ,i.e., ±60 degrees with respect to the neutrino beam. The inner surface of OD is coverd with white light reflecting sheets called Tyvec.

The electronics and data-taking system in KT shown in Fig. 2.3.1 is very similar to those in Super-Kamiokande described in Subsection 2.2. We will describe here only the difference.
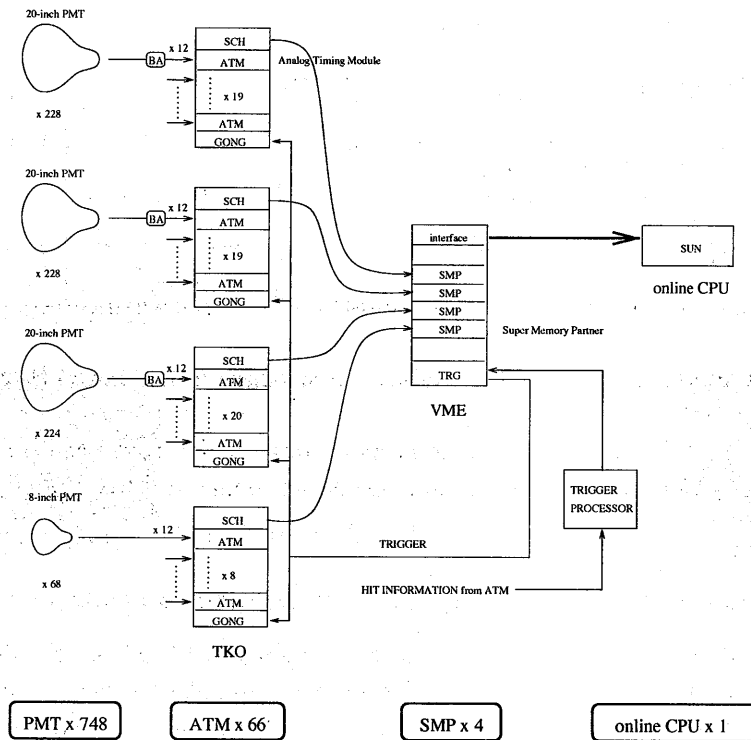
Figure 2.27: Data acquisition system for the 1kt water Cherenkov detector (KT)

A signal cable connecting a 20-inch PMT and analog electronics ATM is 70 m long in Super-Kamiokande. Incomplete termination induces a reflection pulse 700 nsec later to ATM. Each channel in ATM in Super-Kamiokande has a 900-nsec dead time every time it is hit to avoid the reflection pulse. However, the 900-nsec dead time would make it difficult to record

multiple events produced by 1.1 μsec beam spill in KT. Therefore, we gave a modification to the original ATM modules to reduce the dead time down to 300 nsec. Furthermore, we employed a longer signal cable (110 m in length) to delay the reflection pulse (1.1 μsec later) out of the beam spill. The final problems to be solved in ATM is that it still has a 300-nsec dead time and that it has only 2 TAC/QAC per channel. This latter problem implies that it is possible not to record ≥ 3 successive events in a beam spill. To compensate for these problems, we installed a 2-channel 500-MHz 8-bit transient digitizer with 16 μsec full scale, as is shown in Fig. 2.3.1, which continuously records the analog sum signal (PMTSUM) from ID 680 PMTs and from OD 68 PMTs separately. The transient digitizer counts number of events > 1000 p.e.(≈ 100 MeV for an electron) in a beam spill to eliminate μ-decay electrons.
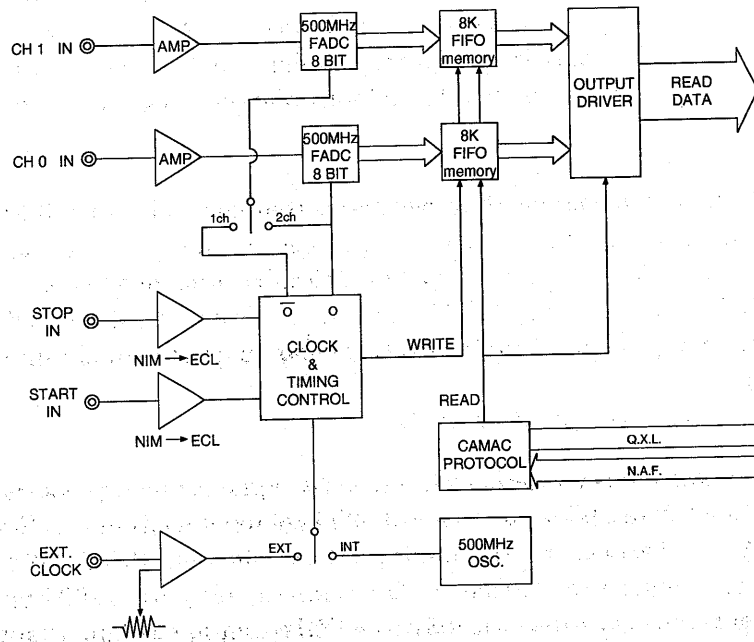
Figure 2.28: Block diagrams of the transient digitizer used in KT

2.3.2 Fine-grained detector (FGD)

The fine-grained detector(FGD) gives an accurate measurement of neutrino energy spectrum and contamination of electron neutrinos at the neutrino production point. The FGD has 4 different instruments, each playing a specific role in neutrino flux measurement.

Scintillating Fiber tracker (SFT)

The Scintillating Fiber tracker(SFT) [103] is used for finding the vertex position and the

direction in a neutrino event. It has a sandwiched structure of 20 scintillating fiber sheet modules interleaved with 19 water tube layers as shown in Fig. 2.29. One module consists of 6 horizontally aligned and 6 vertically aligned fiber sheets, attached to a honeycomb panel. One scintillating fiber sheet has 1142 fibers, each of with is a fiber length of 3.7m long.
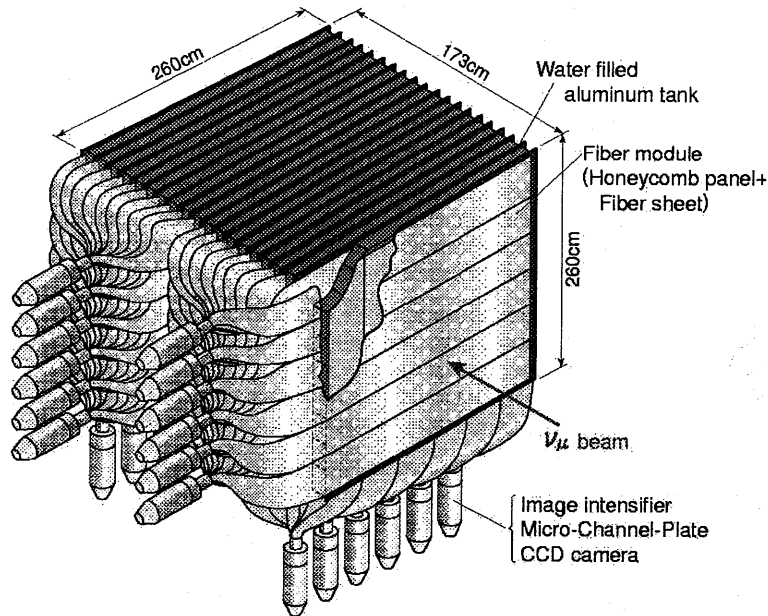
Figure 2.29: Schematic view of the scintillation fiber tracker with the water target.

The neutrino detection area is $2.4m \times 2.4m$. The fiber type is Kuraray SCSF78M (multi-cladding). Fibers are attached to 24 image-intensifiers(IITs) with CCD readout [104]. One water tube layer consists of 15 water tanks made of $1.8mm$ thick aluminum; 240cm $\times$ 16cm $\times$ 6cm in size. The total of 285 water tubes which consists of 6.03 tons of water and 1.44 tons of aluminum are used for the neutrino target. A total mass of SFT is 8.7 ton including the fiber sheets, honeycomb panel and so on. For the tracking method in SFT, refer to [105].

Trigger counter/Veto counter

The trigger counter(TG), for the purpose of getting event time information, is placed between the SFT detector and the Lead Glass calorimeter. Also TG serves as a pre-shower counter of the Lead Glass for electrons. The one unit of the counter is made of plastic scintillator 466 cm long, 10.4 cm wide and 4cm thick. One PMT is attached to both ends of the scintillator. TG has 40 scintillator units placed one upon another and has a total height is 4 m. The PMT signals divided at the NIM divider are fed to the ADC and the TMC(Time Mean Cell), where information about event timing and deposit energy are recorded when charged particles go through the counters. By using the relative time information of both-end PMTs in a scintillator, the horizontal position which particle goes through, can be measured with better than 5cm position resolution. The purpose of the veto counter is to veto the event from

the 1kton water Cherenkov detector, located just in front of the SFT detector. The counter is composed of 20 units of scintillator modules, each of which consists of 2 plastic scintillators with a PMT at both ends.The veto counter covers an area of 4.6m × 4.6m, the same area as the trigger counter. Veto counter signals are also treated in the same way as the trigger counter's.
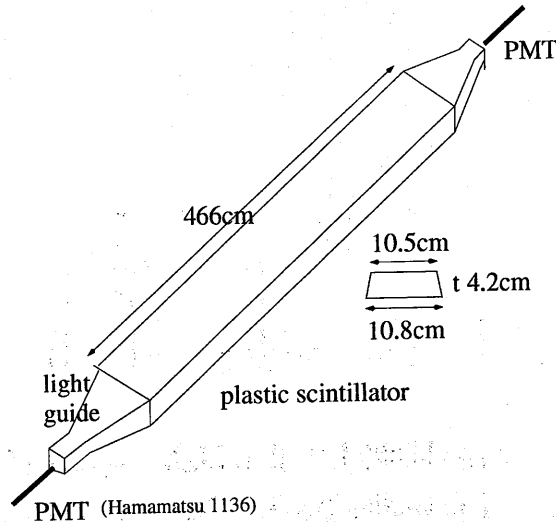
Figure 2.30: Schematic view of the trigger counter (TG).

Absolute energy calibration is made using cosmic-ray muon measurement. The attenuation length of a plastic scintillator is measured to be 2.4m. The energy resolution corresponding to mip is 7.4%, as shown in Figure 2.31. The detector simulation for TG is tuned to reproduce the result of the test.

The horizontal position can be calculated from TDC information of PMTs at both ends, with a position resolution of 5.0cm as demonstrated in Fig. 2.32, which obtained in the cosmic-ray test.

Lead Glass calorimeter

The Lead Glass(LG) calorimeter is located downstream from TG. The purpose of LG is to distinguish electrons from muons. A LG cell about 10cm × 10cm × 34cm, through a light guide cylinder made also by lead glass of 2.5inch in radius and 6cm in length, is viewed by 5inch-in-diameter PMT(Hamamatsu,R1652), as shown in Figure 2.33.

The LG calorimeter is made up of 600 cells. This LG calorimeter was once used in the TOPAZ experiment [53]. 60 LG cells constitute one module, and there are a total of 10 modules in this counter, as shown in Figure 2.34.

The energy scale of the LG calorimeter is described here after. The 9 standard LG cells in the LG calorimeter were pre-calibrated to 5% or 7% by the electron beam from the electron synchrotron. The other LG cells were relatively calibrated to the 9 standard cells by cosmic-ray muons. For the relative PMT gain adjustment, we neglect the second peak (light guide effect)
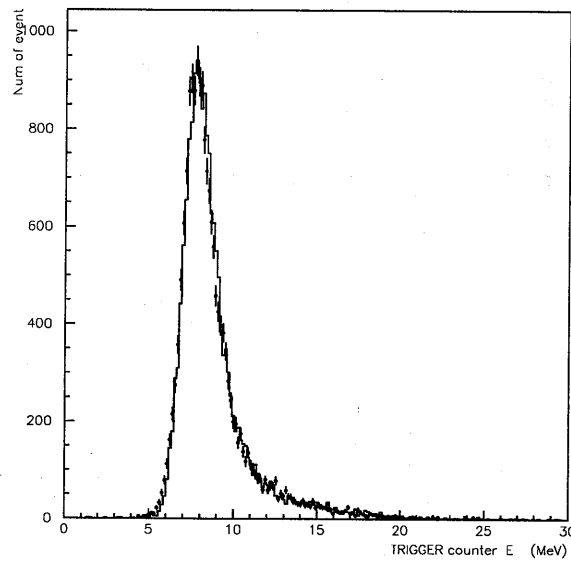
Figure 2.31: Trigger counter energy distribution measured in a cosmic ray test. The points with error bars represents data, while solid histograms are from a simulation.
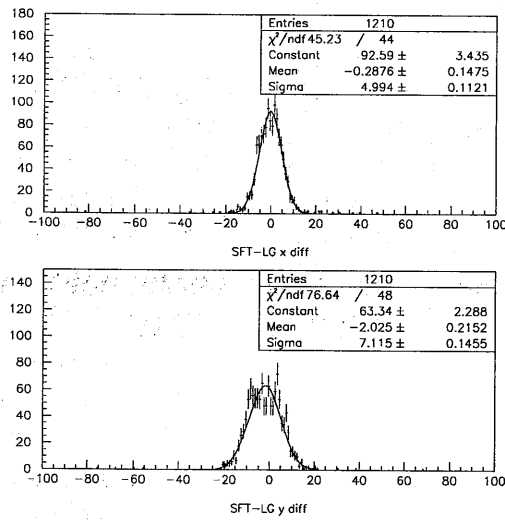
Figure 2.32: Trigger counter position residual distribution. The Upper figure is the horizontal direction, the lower one is the vertical direction.
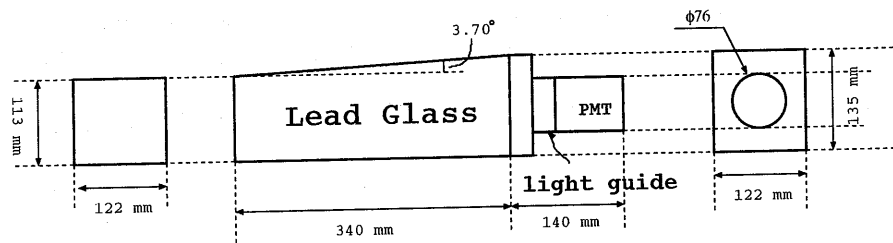
Figure 2.33: One cell of LG Calorimeter.

lead glass 12 x 5

Al support
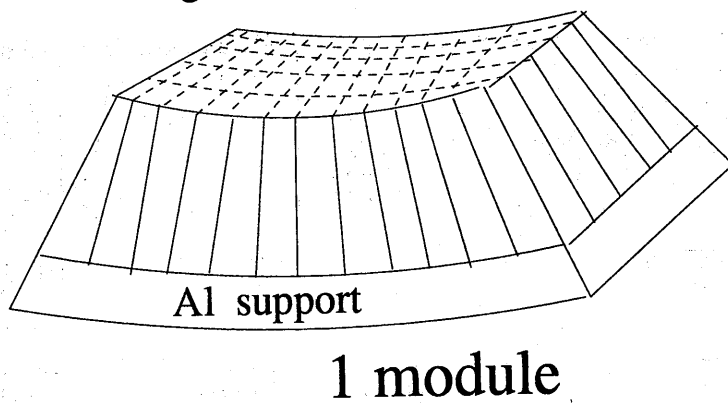
1 module

Figure 2.34: One module of the Lead Glass Calorimeter

in the pulse height distribution as is shown in Fig. 2.35 which is caused by a muon hitting the light guide.

Electron response was measured with the electron synchrotron at KEK-Tanashi in 1997. In this experiment, the absolute energy scale calibration was determined for electrons which covered the energy region from 50 MeV to 1.1 GeV.

Generally, the energy resolution σ is described as function of energy deposit E,

$$(\frac{\sigma(E)}{E})^2 = \frac{\sigma_0^2}{E^2} + \frac{\sigma_1^2}{E} + \sigma_2^2, \tag{2.4}$$

where σ_0 reflects effects from energy-independent electronics noises, σ_1 comes from photo-electron statistics, and σ_2 from energy leakage proportion to energy.

In the case of LG, the energy resolution is described only by the second term. Therefore, the energy resolution is;

$$\frac{\sigma(E)}{E} = \frac{\sigma_1}{\sqrt{E}}. \tag{2.5}$$

As shown in Figure 2.36, $\sigma_1 = 10\%$ at 1 GeV was obtained by the pre-calibration at KEK-Tanashi.

Position dependence for energy resolution is measured to be 4% as shown in Fig. 2.37.

Responses for muons were calibrated by cosmic-ray muon measurements at KEK, made from 1997 to 1998. In the cosmic ray measurement, relative pulse height peak for each PMT was adjusted to within 2% [107], while responses for charged pions were measured in the KEK beam test in 1998. In this beam test, the responses for pions were checked at different momenta (300 - 2000GeV/c), as shown in Fig. 2.38. They are in good agreement with the MC simulation.

The MC simulation processes are as follows:

1. The particles enter Lead Glass.

2. Cherenkov light photons are emitted in the Lead Glass body, when a charged particle is detected.

3. Cherenkov light photons are traced, assuming a refractive index n=1.804 is constant independent of Cherenkov photon energy.

4. The reflections from the LG cell and the light guide are taken into account, then the yield at the PMT surface is obtained. At this step, the reflection rate of the LG cell is set to 100%, while the reflection rate of light guide to 38%.

The simulated LG response is in good agreement with the cosmic ray data and the beam test data as shown in Fig. 2.38 and Fig 2.39, respectively.

Muon range chamber (MUC)

The muon range chamber (MUC) measures muon energy by tracking a muon trajectory. MUC has a sandwiched structure of iron plates and wire chambers as shown in Fig. 2.40.
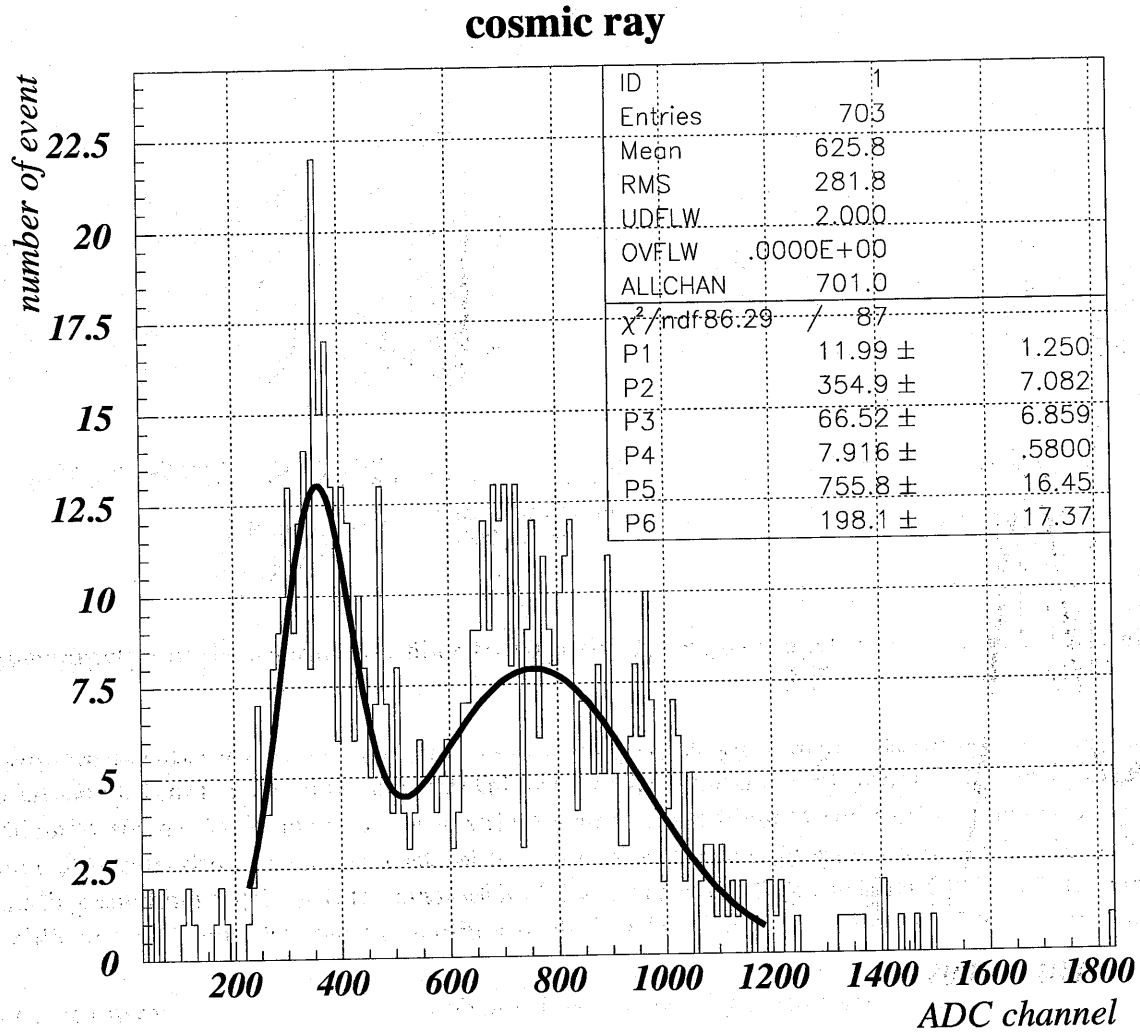
cosmic ray

Figure 2.35: Pulse height of a LG cell for cosmic-ray muons. The first peak around 350 counts, which is made by muons penetrate the LG cells without hitting the light guide, is employed to be adjusted in a cosmic-ray calibration. The second peak at 800 counts is made by muons hitting the light guide.
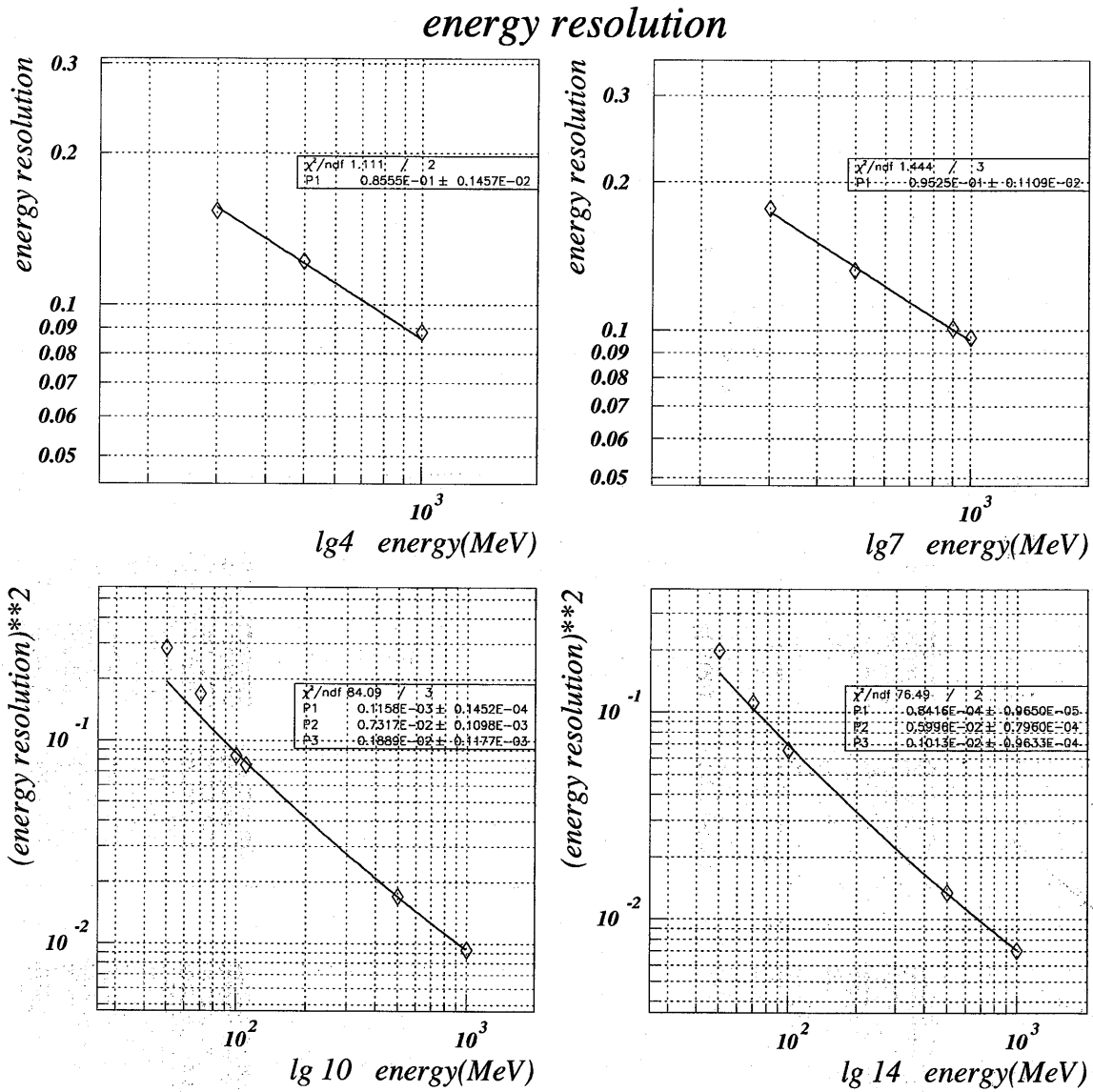
energy resolution

Figure 2.36: Energy resolution for electron beam.On the horizontal axis are incident energies and on the vertical are energy resolutions. The lines are fitting results.The upper figures use only σ_1 for fitting. As low energy region measurements had been conducted, The lower figures use the function $(\frac{\sigma(E)}{E})^2 = \frac{\sigma_0^2}{E^2} + \frac{\sigma_1^2}{E} + \sigma_2^2$ for fitting.

sigma/mean (X- pos. depend.)
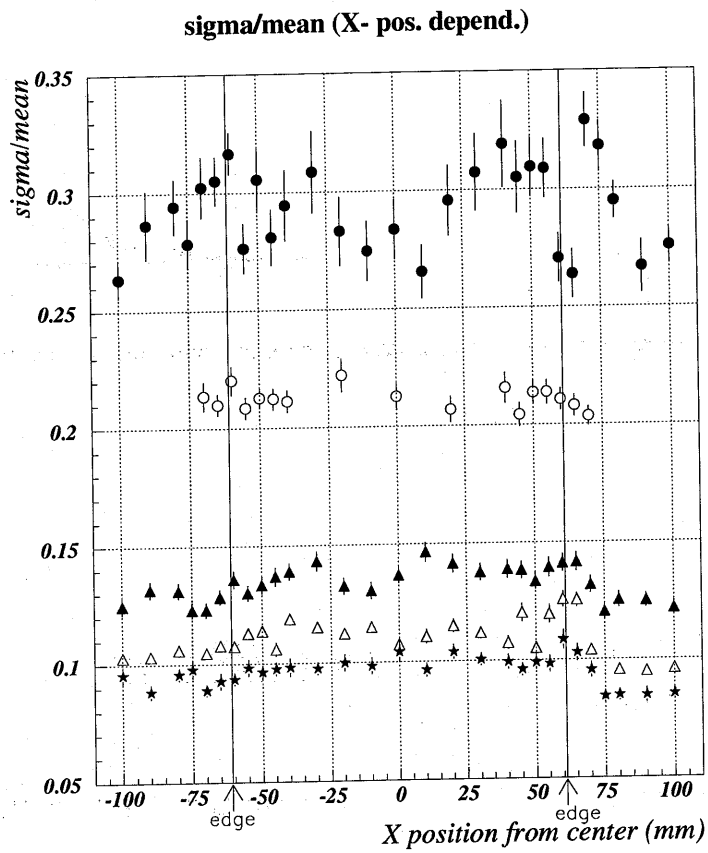
Figure 2.37: Dependence of energy resolution on incident position for electron beam. Electrons of different incident energies were measured. The black circles are $100MeV$, white circles are $200MeV$, black triangles are $500MeV$, white triangles are $800MeV$, and stars are $1000MeV$.
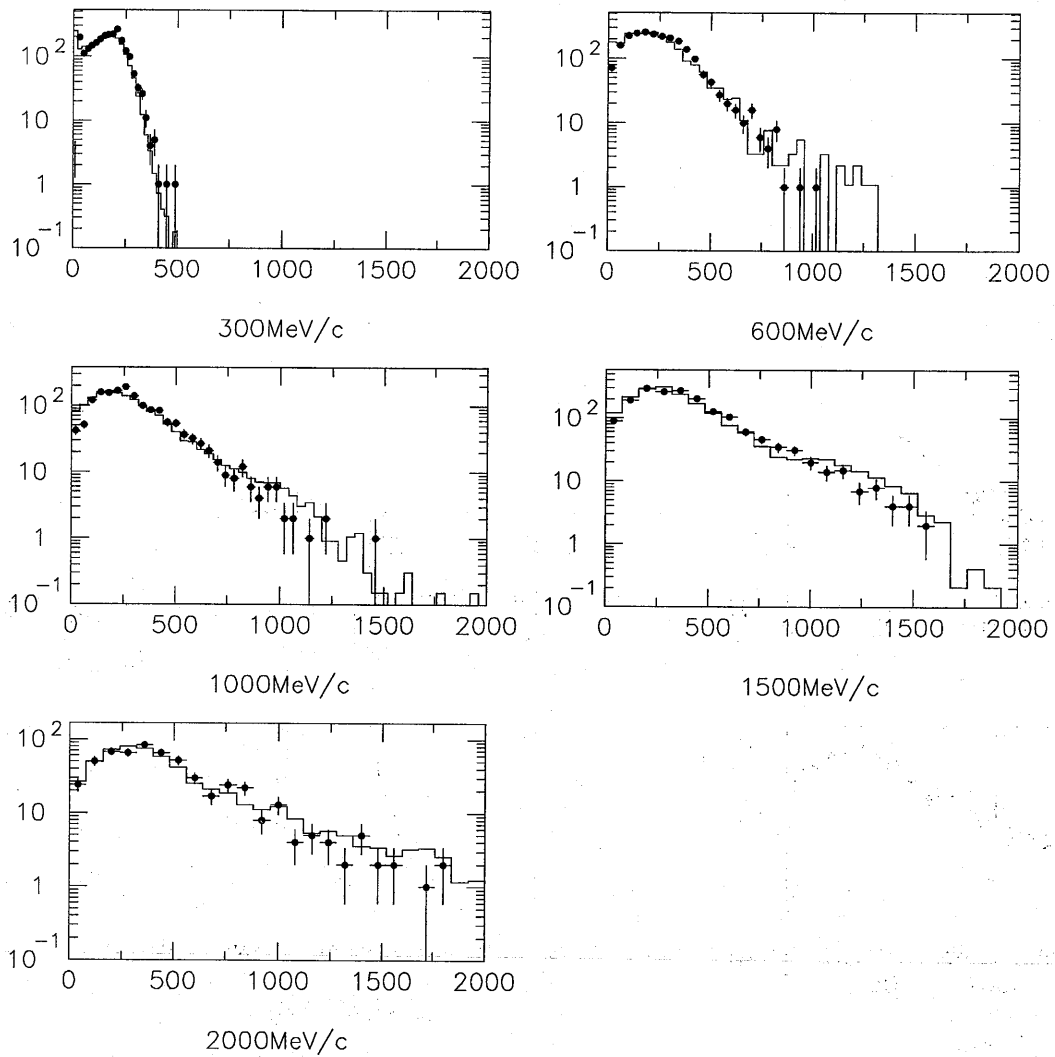
Figure 2.38: Responses for charged pions at different beam momenta. The filled circle with an error bar are data, the solid histograms are our MC simulation.
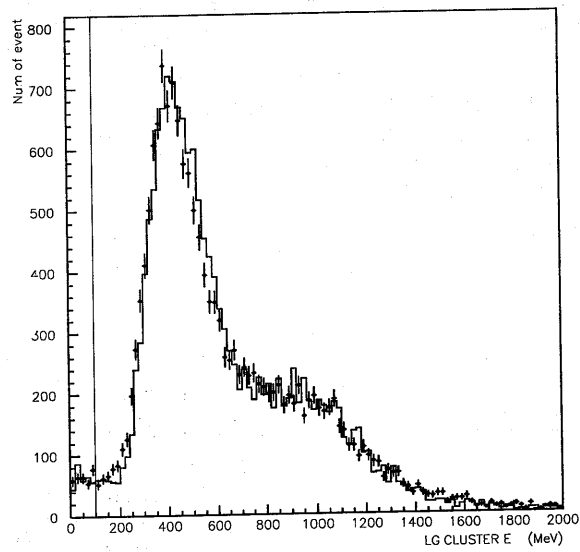
Figure 2.39: LG cluster energy distribution for cosmic-ray muons. Filled circles with error bars are the data, and solid histograms are our MC simulation.
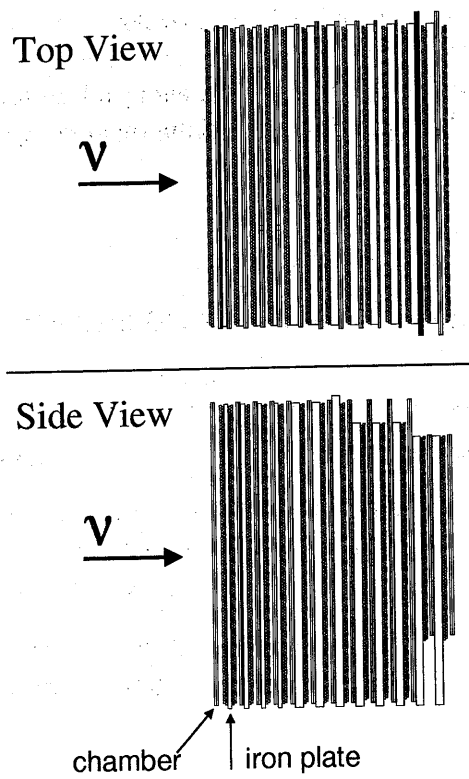
Figure 2.40: Schematic view of muon range detector.

We use 3 different iron plates in size:

4 7.5m(x)×7.5cm(y)×10cm(t),

3 7.5m(x)×7.5m(y)×20cm(t),

5 7.5m(x)×7.0m(y)×20cm(t).

The total iron mass is 1000 tons, and there are 6632 wire chambers (x and y directions). The P10(Ar 90% + CH$_4$ 10%) is employed. The electron drift velocity is expressed by "2.11×t(μs)+2.72×t^2" (cm/μs). These chambers were used in the VENUS experiment [50], [54] . The signal from each hit wire goes to the electronic box, it is transformed to an ECL level signal. Then, signal is sent to a memory module to measure the timing of the hit. Using timing and position information for the hit wires, a particle trajectory is tracked. The hit efficiency is more than 99 %, confirmed by the cosmic ray test. The tracker's tracking efficiency is shown in Fig. 2.41. Tracking efficiency is defendant on track length. When track length is more than 3 iron-plate long, it amount to 99%. The tracker algorithm is as follows:

1. Two or more hits are required in both upstream side and downstream side of an iron plate.

2. These hits are to be in the same 100nsec time intervals.

3. The straight line fit is applied to the hit group above.
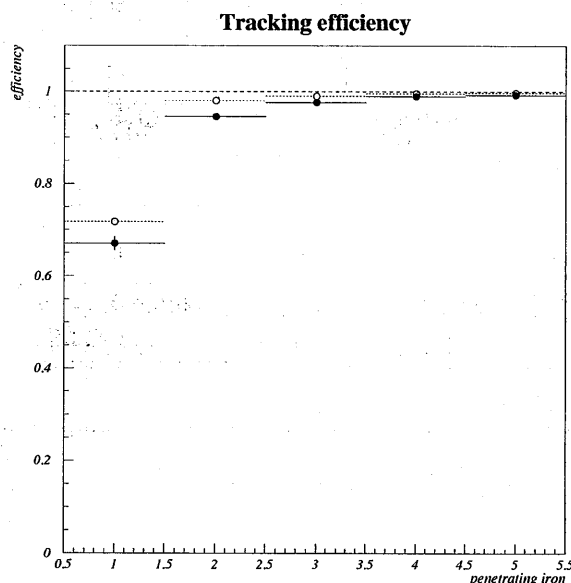
Figure 2.41: Tracking efficiency of the muon range chamber (MUC), as a function of number of iron plates transversed, where filled (open) circles are cosmic-ray data (our MC simulation).

The particle energy is calculated by its tracking length. As shown in Fig. 2.42, the tracker has the energy resolution of 146 MeV, position resolution of 12 cm and 7.6 cm for horizontal and vertical axes respectively and angular resolution of 0.13 radians.

Muon tracks at 200kA (MC, Cho-CERN)

Entries	24813
Mean	0.1139
RMS	11.53
UDFLW	737.0
OVFLW	1124.

fitx-truex

Entries	24813
Mean	-0.9591E-01
RMS	7.647
UDFLW	135.0
OVFLW	406.0

fitx-truex

Entries	24631
Mean	-0.1414E-01
RMS	0.1457
UDFLW	145.0
OVFLW	214.0

E_μ*(Fit-MC)*

Entries	24631
Mean	0.8960E-02
RMS	0.1352
UDFLW	538.0
OVFLW	910.0

angle(Fit-MC)
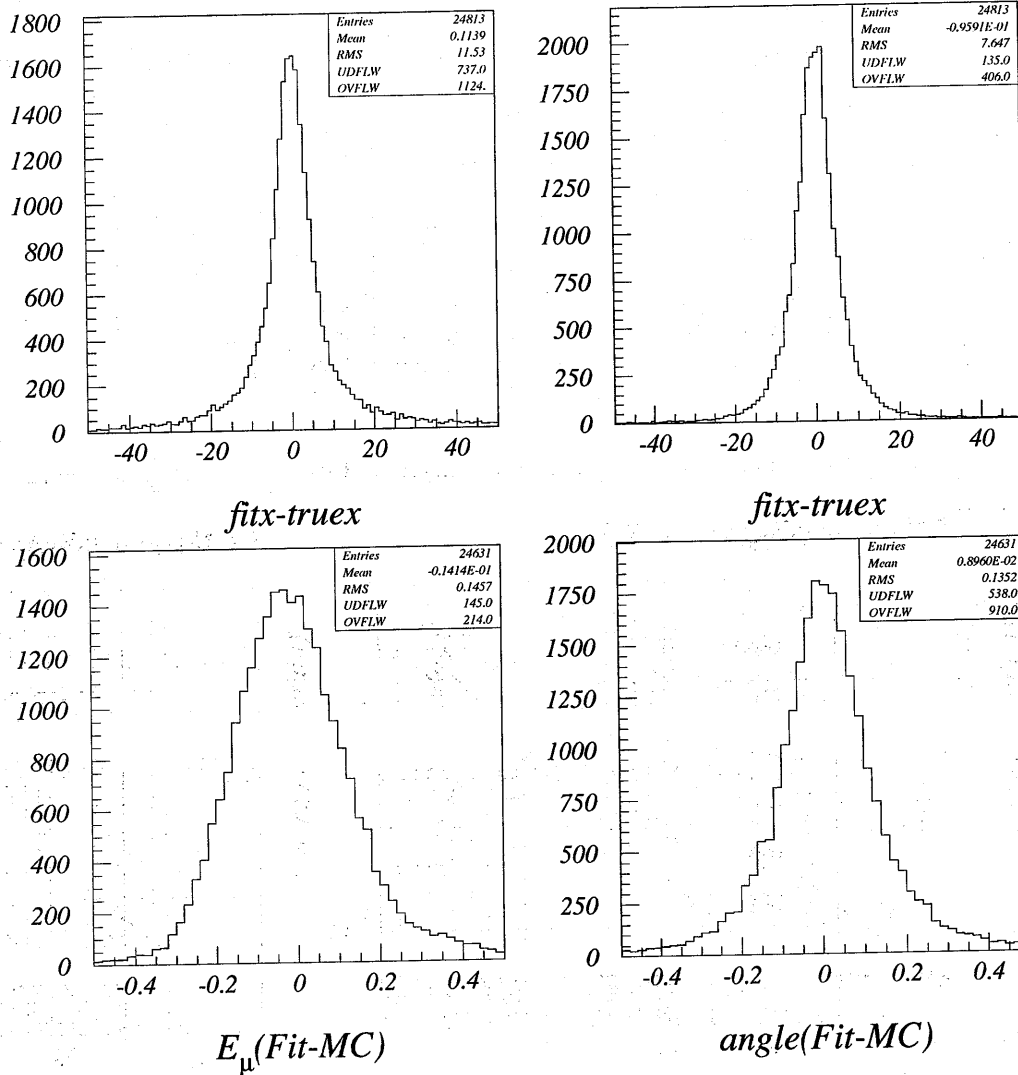
Figure 2.42: Tracking residual distribution of muon range chamber (MUC). The upper left figure is the position distribution in the horizontal direction, the upper right figure is the position distribution in the vertical direction, the lower left figure is the energy distribution and the lower right figure is the angular distribution.

Summary of Fine-Grained Detector

Each performance has been already reported in the section above. Here, we would like to summarize it in Table 2.2.

Energy resolution of trigger counter	8% for mip
Position resolution of trigger counter	$5cm$ for X, $7cm$ for Y
Energy resolution of Lead Glass	$\frac{10\%}{\sqrt{E}}$
Hit efficiency of muon chamber	$> 99\%$
Noise hit rate of muon chamber	0.4%
Tracking efficiency of muon chamber	$> 96\%$
Energy resolution of muon chamber	$146 MeV$

Table 2.2: Sub-detector performance

2.3.3 Data acquisition system of near detector

Each component of the near detector has a different readout system. Therefore, the data acquisition system(DAQ) for the near detector has an individual readout system for each component, and one event builder system.

The 1kton water tank DAQ system uses the TKO-ATM(Analog and Timing Module) system and the SUN-VME interface readout. All PMT signals go to ATM modules to get the charge information and timing information digitized. A SUN computer machine reads all the ATM information via the VME-TKO interface, and sends all the data to an event builder computer.

The fine-grained detector has two client processes in separate two on-board computers. One process reads the SFT detector data, and the other reads data pertaining to all other components: VETO, TG, LG, MUC.

The SFT readout system employs NIM-FADC(flash ADC) and VME-FIFO(first in; first out) modules to get image information from CCD cameras. There are 12 FADC modules. Each module has two channels. These channels correspond to the 2 IIT images. All 12 FIFO modules are connected to a single one FADC modules. The collector access to a VME-HPRT on-board computer to get all IIT information spill by spill. The gate width for ADCs is $100\mu sec$.

The veto and trigger counter system read out 3 types of information from each signal of the 120 PMTs. One is the charge information corresponding to the energy deposit. The readout system is the FASTBUS ADC (Lecroy 1810 module). Another type is the timing information. The VME-TMC modules are used. This module can record multi-hit signals within $3\mu sec$. The start timing of the TMC trigger is adjusted $1\mu sec$ before the beam time. Third type is also the timing information longer than TMC full scale.

The LG detector system reads out only the charge information. The readout system is the FASTBUS ADCs as the veto and trigger counters. The ADC gate width is $1.5\mu sec$.

The muon chamber signals are fed to the electronic boxes. The electronics box convert each wire analog signal to a digital pulse signal with timing information. Then, the TKO-Memory modules collect hit wire time information within $3\mu sec$ for the computer read-out.

Front detector DAQ
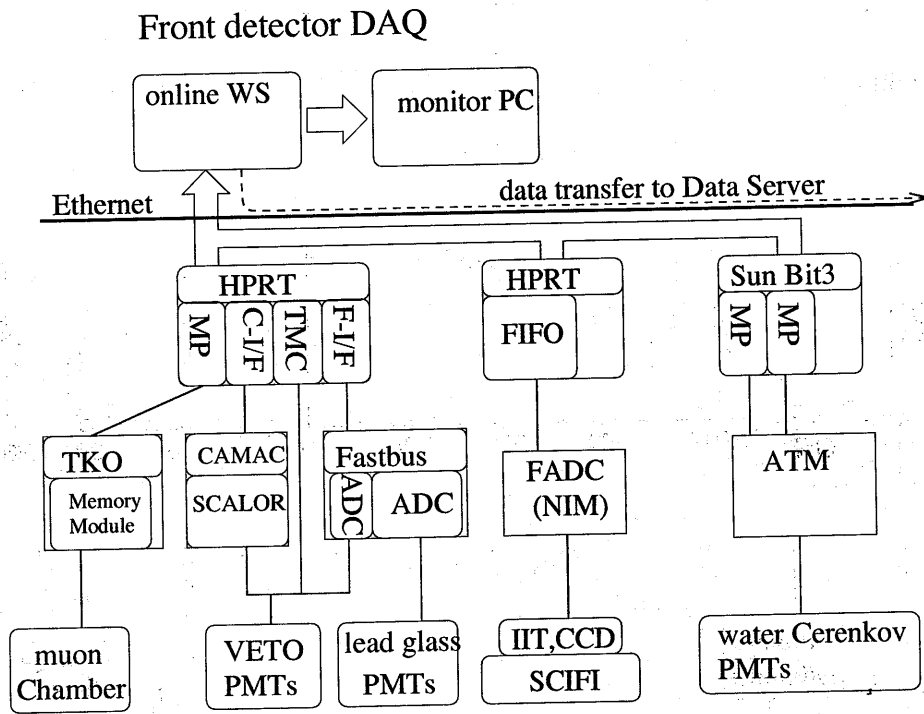
Figure 2.43: Near detector data acquisition system

The event builder collects all components of the near detector data using the spill number. The spill number is generated by TRG modules at the North Counter Hall, which counts up by a beam kicker signal from the accelerator. This process runs on a SUN workstation. Built data is sent to data server machines, then stored on DLT tapes. The data size of the near detector is about 1 MBytes per spill.

Chapter 3

Simulation

3.1 Monte-Carlo simulation for neutrino beam

The neutrino-beam simulation cover the region from the target to SK. Their components are as follows:

1. Protons are injected to the target with the measured beam emittance.

2. Secondary pions and kaons are generated using a hadron production model in the target.

3. Generated particles are traced in the magnetic field of the horns.

4. Pions, kaons and muons are made to decay into a neutrino and/or an anti-neutrino.

For this purpose, we adopted the GEANT[64] program which has been developed at CERN and commonly used in high-energy experiments.

We must take into account geometry difference between the June configuration and the November configuration in MC simulation since we changed the target part of the 1st horn, as described in Chapter 2. Since the injection of the proton beam was also changed, we also take it into account.

3.1.1 Proton Beam Profile at the Target

There are two SPICs between the last magnet and the target. The SPIC just after the 39th Vertical dipole magnet, is called as "V39 out SPIC" and that of just before the target is called "TARGET SPIC".

Figure 3.1 shows a typical x and y projection image of protons in June 1999. Each strip of "V39out SPIC" is 5 mm wide and that of "TARGET SPIC" is 1.27 mm, as summarized in Table 2.1. The emittance of proton beam is calculated assuming that protons do not cross over and the image of the proton beam is ellipse like.

Figure 3.2 shows the schematic view of this calculation and Figure 3.3 shows the results of this calculation in the June configuration where x and y stand for the position of the beam and dx and dy for the beam divergence.
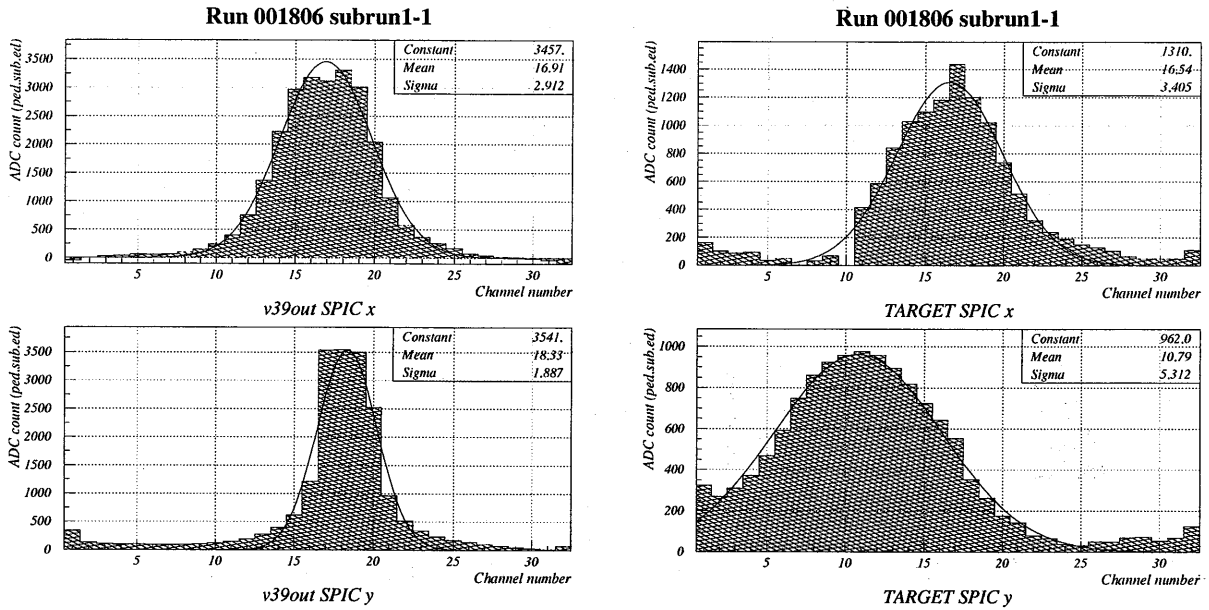
Figure 3.1: The Proton beam profiles measured by the two SPICs before the target. Strip width of "V39out" is 5 mm and that of "TARGET" is 1.27 mm
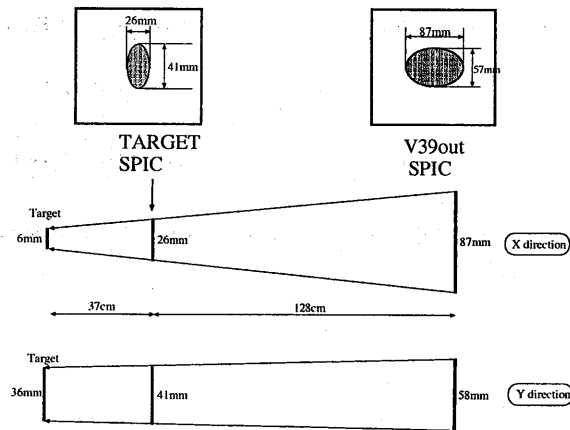
Figure 3.2: The schematic view of the proton beam emittance calculation. The shaded regions correspond to the 3σ contour given by a fit to the profile data assuming an Gaussian distribution.
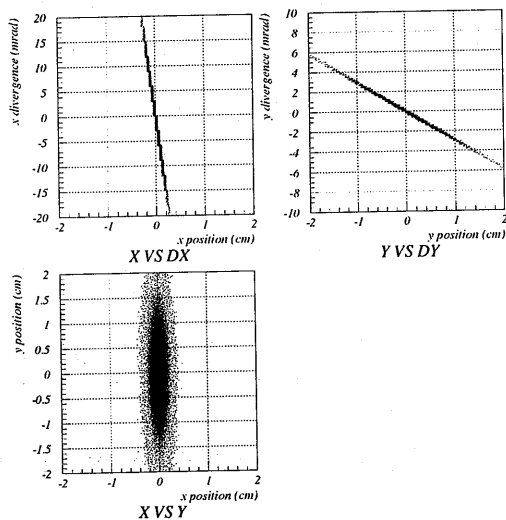
Figure 3.3: The results of the proton beam emittance calculation. Top-Left: x vs dx (x is the horizontal position, dx is the horizontal divergence of the beam), Top-Right: y vs dy, Bottom-Left: x vs y (proton beam profile at the target)

Figure 3.4 shows the same plots in the November configuration. The calculated proton beam profile at the target in the November configuration is wider than that in the June configuration in the horizontal direction.

3.1.2 Production of Secondary Pions and Kaons at the Target

Some hadron production models about secondary-pion production at the target can be chosen in this simulation. This is the largest ambiguity in this Monte Carlo simulation. There have been various pion production experiments in this energy region, however, the results of these experiments are different from one another.

Three kinds of pion production models are used to be compared.

1. GCALOR/FLUKA model [66] [65].

   This model has a larger cross section for the p-Al interaction than other models. It tends to produce higher energy secondary pions.

2. Fit to measurements (I), Sanford-Wang[67].
   This model used the results of the compilation of the measurements made by Lundy *et al.*(13.4 GeV)[68], Dekkers *et al.*(11.8, 18.8 and 23.1 GeV)[69], and Baker *et al.*(10.9, 20.9 and 30.9 GeV)[70]. The results of this compilation are described by Yamamoto and used by him for a comparison with his measurements [71]. Yamamoto's measurements agreed well with this compilation.
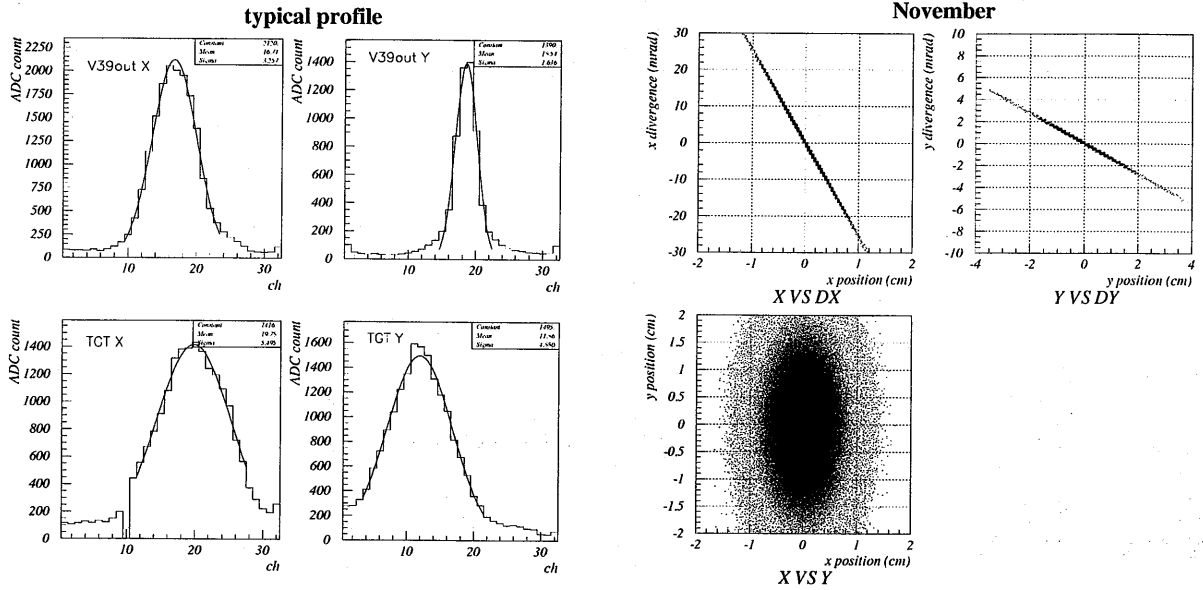
Figure 3.4: The Proton beam profiles measured by the two SPICs and the results of the proton emittance calculation.(November)

3. Fit to Measurements (II), Cho[72].

This uses the result of the measurements performed by the Cho's group few years later to resolve a question of low cross sections measured by Lundy *et al.*[68] on the same proton beam at Argonne and to have a better understanding of their neutrino beam. This experiment uses the spectrometers to measure the accurate differential cross sections $(d^2\sigma/d\theta dp)$. The results are fitted using Sanford-Wang formula with other experimental ([73],[74],[75],[76]) results.

Sanford-Wang formula is an empirical formula which gives a quantitative description of the secondary particle production based on the characteristics of experimental data[67]. This formula has 8 parameters and is represented in Ref.[72] as follows;

$$\frac{d^2n}{d\theta dp} = C_1 \cdot p^{C_2}\left(1 - \frac{p}{p_B - 1}\right) \cdot exp\left(-\frac{C_3 \cdot p^{C_4}}{p_B^{C_5}} - C_6 \cdot \theta(p - C_7 \cdot p_B cos^{C_8}\theta)\right), \quad (3.1)$$

where, $d^2n/d\theta dp$ is the differential particle yield per interacting proton, the C_i's are the constants to be found by fitting, p is the momentum of the secondary particle, θ is the angle between the secondary particle and the beam axis and p_B is the beam momentum. Cho *et al.* fitted the particle yield instead of the cross section. Fitted result about π^+ production in reference[72] is summarized in Table 3.1. Their measurements[72, 73, 74, 75] and fit results for π^+ and π^- in Ref.[72] are shown in Fig. 3.5.

The GCALOR/FLUKA[1] model is interfaced to be a part of GEANT package. Thus, GEANT simulates everything using the GCALOR/FLUKA automatically. In other models,

---

[1]FLUKA model was called if incident particle is above 10 GeV even when GCALOR model was called.
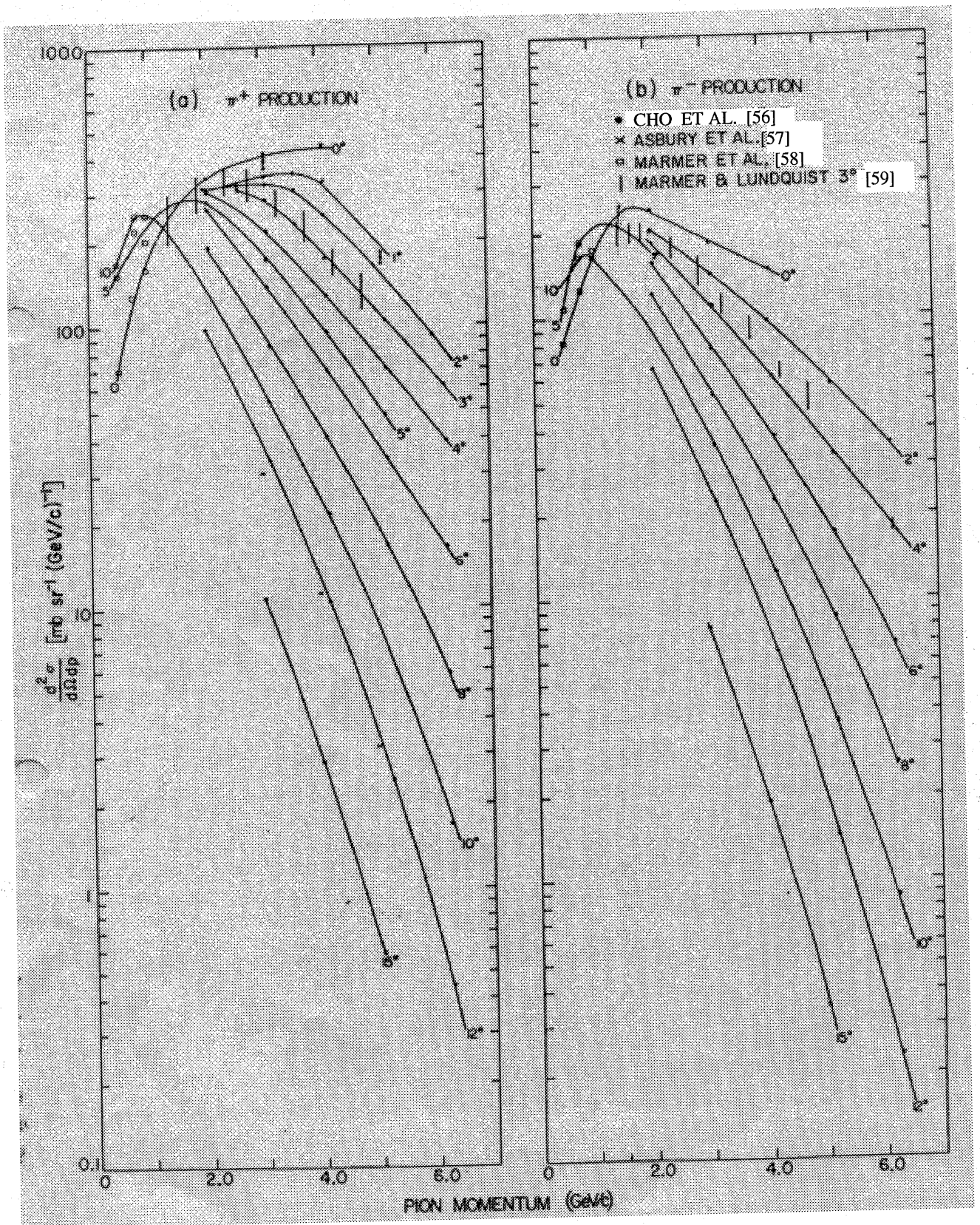
Figure 3.5: Results of the pion production measurements[72, 73, 74, 75] and fitted results by Sanford-Wang formula[67]. Left figure: π^+, right figure: π^-.

	C_1	C_2	C_3	C_4	C_5	C_6	C_7	C_8
2. SW	227	0.65	4.05	1.63	1.66	5.03	0.172	82.7
3. Cho	196	1.08	2.15	2.31	1.98	5.73	0.137	24.1

Table 3.1: The fitted parameters of the Sanford-Wang formula by Sanford-Wang and Cho *et al.*[67, 72]. Only for π^+ production is shown here.

only the interaction of protons more energetic than 10 GeV with the target aluminum is simulated according to Eq.3.1. And the less energetic interactions are simulated according to GCALOR model. When using the Sanford-Wang formula, we refer to [67] for kaon production.

The hadron production model dependence of the ν_μ flux is shown in Fig. 3.6. The Cho hadron production model is employed in our simulation.
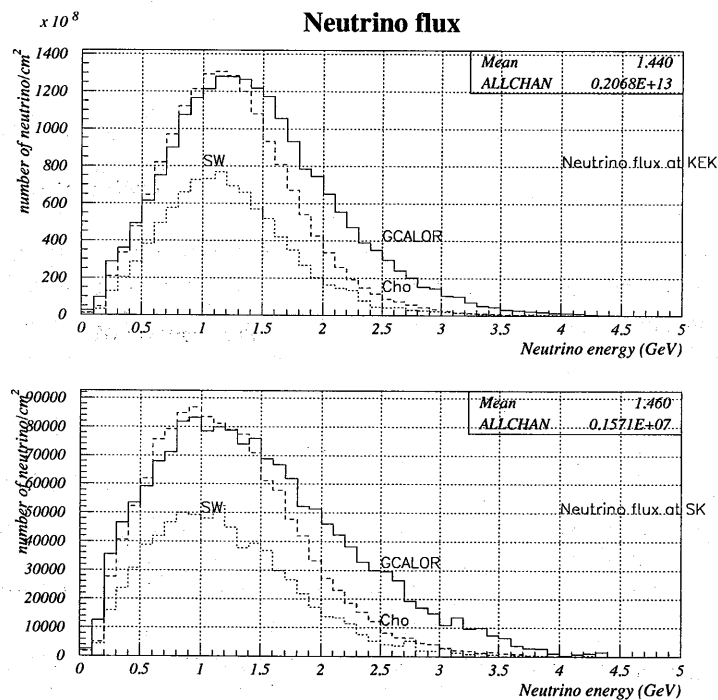
Figure 3.6: Hadron production model dependence of ν_μ flux.

3.1.3   Magnetic Field Generated by the Horn Magnets

As already explained, horns work as toroidal magnets to focus positively charged pions. This magnetic field has to be considered in this simulation.

Calculated magnetic fields in the horns are used in the simulation. A measurement of the magnetic field at the air part of the 1st horn confirmed the reliability of the calculation. [48]

The magnetic field inside the target is calculated with static approximation as a function of the radius. If one takes into account the skin effect, our magnetic field penetrates only ~ 5 mm into the target.

3.1.4 Treatment of Particle Decays in the Simulation

GEANT[64] makes particles decay only isotropically. Thus, the energy and angular distributions of the decay products in three-body weak decays of kaons and muons are simulated by our original code based on the V-A theory referring to [78, 79], while those in the other decays are simulated by GEANT.

The following decays are considered to produce neutrinos in the simulation.

Pions

Only one decay mode, $\pi^{\pm} \to \mu^{\pm} + \nu_{\mu}$ (abbreviated to $\pi^{\pm}\mu_2$), is taken into account since the branching ratio is almost 100%.

Kaons

The main contributions to the neutrino beam are as follows,

1. $K^{\pm} \to \nu_{\mu} + \mu^{\pm}$ (63.51 %) (abbreviated to $K^{\pm}\mu_2$)

2. $K^{\pm} \to \pi^0 + \mu^{\pm} + \nu_{\mu}$ (3.18 %) (abbreviated to $K^{\pm}\mu_3$)

3. $K^{\pm} \to \pi^0 + e^{\pm} + \nu_e$ (4.82 %) (abbreviated to $K^{\pm}e_3$)

4. $K_L^0 \to \pi^{\pm} + \mu^{\mp} + \nu_{\mu}$ (27.17 %) (abbreviated to $K^0\mu_3$)

5. $K_L^0 \to \pi^{\pm} + e^{\mp} + \nu_e$ (38.78 %) (abbreviated to K^0e_3)

In fact, the contributions of kaons to ν_{μ} are much smaller than that of pions, since the K/π ratio in this energy region is less than 1/10 and kaons have a smaller Lorenz boost factor than pions. For ν_e, muon decays are the dominant source.

ν_{μ}'s from the $K_{\mu3}^{\pm}$ and $K_{\mu3}^0$ modes are neglected, however other channels of kaon decays are taken into account.

Muons

Muons decay as "$\mu \to e + \nu + \bar{\nu}$", of which the branching ratio is almost 100%. The effect of μ polarization to the angular distribution of decay products is also taken into account.
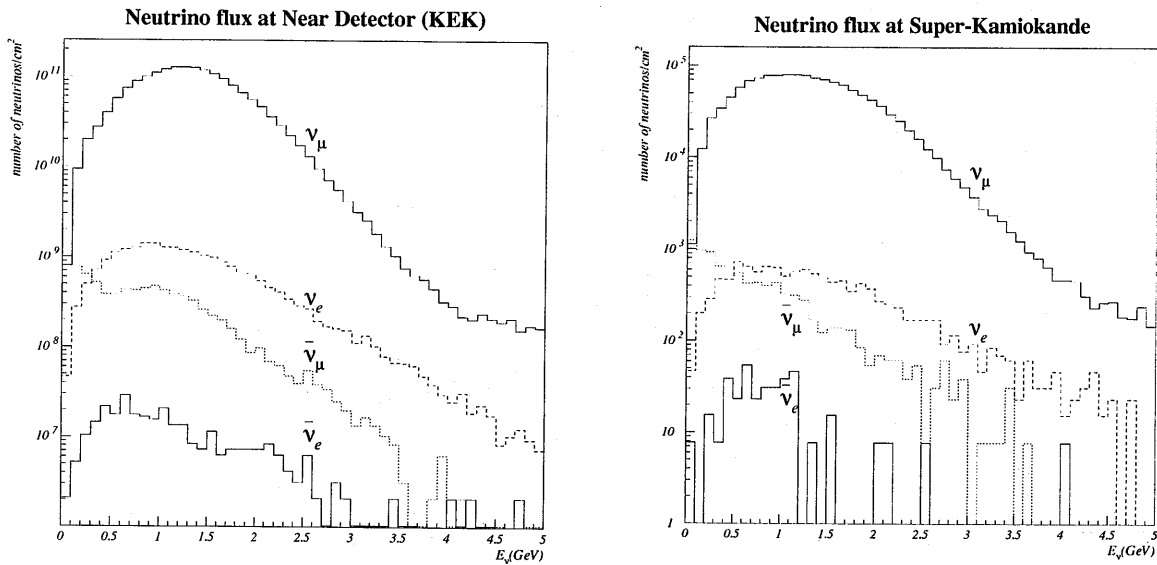
Figure 3.7: Neutrino flux calculation using the Monte Carlo simulation. (The Cho hadron production model is employed) Left figure: Neutrino flux at KEK, Right figure: Neutrino flux at SK

3.1.5 MC prediction of the Neutrino Properties at KEK and Kamioka

Considering the effects above, the neutrino flux at KEK and at SK are calculated. Figure 3.7 shows the results of the calculation in the November configuration. The average neutrino flux spreads over 25cm in radius at KEK and over 200m in radius at Super-Kamiokande.

According to this simulation, the ν_e/ν_μ, the $\bar\nu_\mu/\nu_\mu$, the $\bar\nu_e/\nu_\mu$ ratios are 1.3%, 0.5% and $\sim 2 \times 10^{-4}$, respectively.

Contributions from each decay mode (at KEK only) are shown in Fig. 3.8.

The ν_μ energy spectrum difference between in the June configuration and in the November one are shown in Fig. 3.9. The average neutrino beam energy is higher in the November configuration (1.30 GeV; SK) than in the June configuration (1.23 GeV; SK) because the current supplied to the horn magnets is higher in the November configuration than in the June configuration. The both absolute fluxes are consistent within 1.1% difference due to the higher pion absorption effect in the target in the November configuration, although the higher current can be affects the flux 15% higher.

3.2 MC Simulation for Neutrino Interactions

The average energy of the neutrino flux used in the K2K experiment is $\sim$1.3GeV. These neutrinos interact with the target materials through charged current (CC) and neutral current (NC) weak interactions. We have the following sorts of neutrino interactions;

- CC quasi-elastic scattering $\nu N \rightarrow l N'$
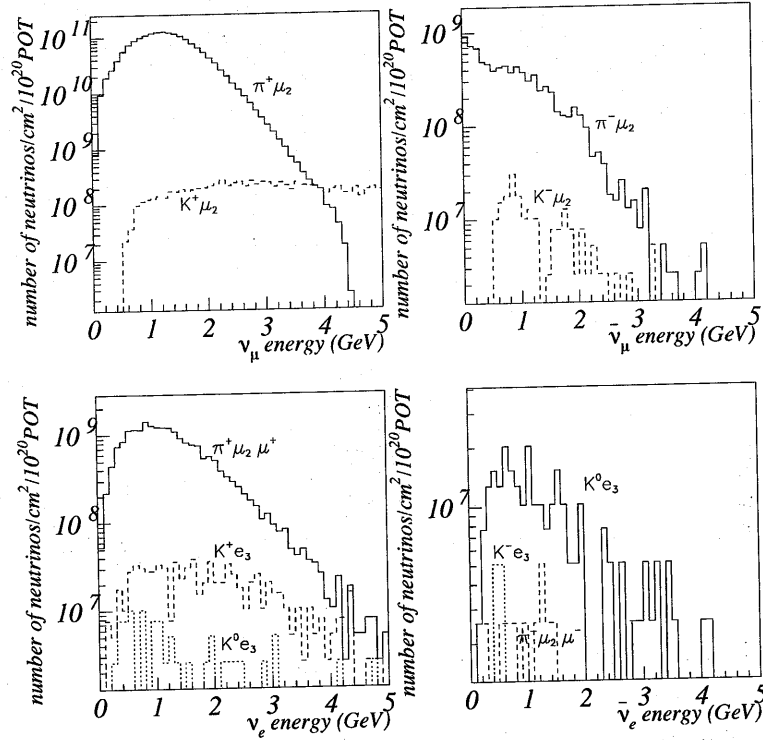
Figure 3.8: Contributions from each decay mode to the neutrino flux at KEK.
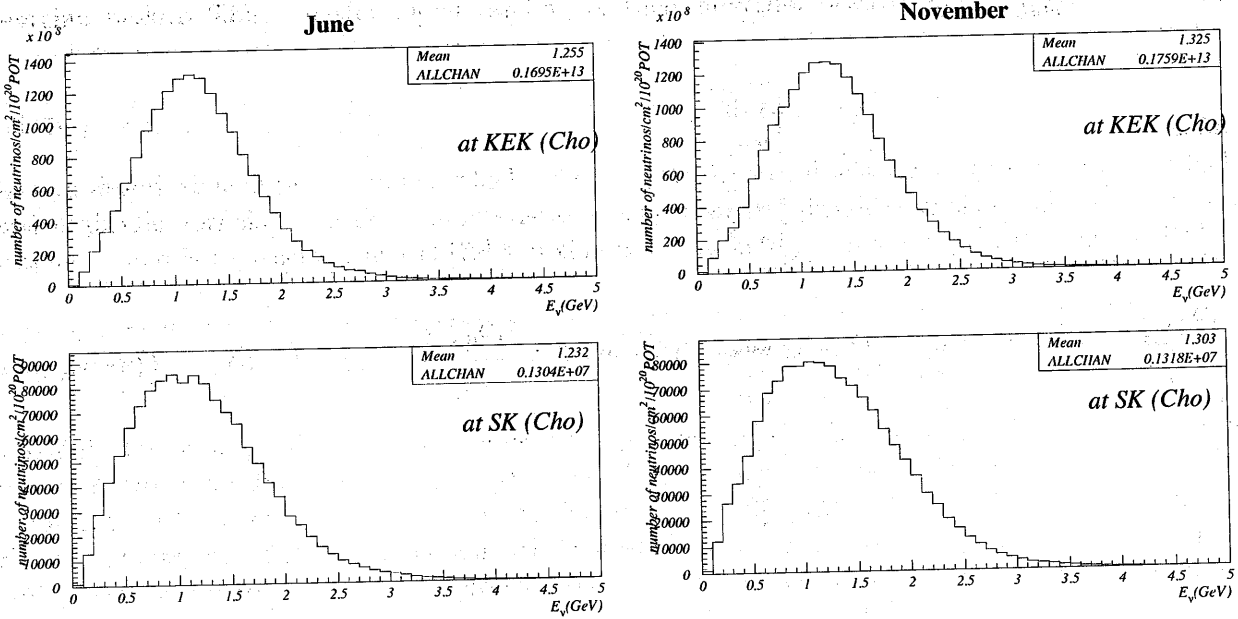
Figure 3.9: The ν_μ energy spectrum difference between in the June configuration and in the November one. Top figures: neutrino fluxes at KEK, bottom figures: neutrino fluxes at SK. Left figures: in the June configuration, right figures: in the November configuration

- NC elastic scattering $\nu N \to \nu N$

- CC single pion production $\nu N \to lN'\pi$

- NC single pion production $\nu N \to \nu N'\pi$

- CC multi pion production $\nu N \to lN'm\pi$ (m)

- NC multi pion production $\nu N \to \nu N'm\pi$ (m)

- CC coherent pion production $\nu^{16}O \to l^{\pm 16}O\pi^{\mp}$

- NC coherent pion production $\nu^{16}O \to \nu^{16}O\pi^0$

where N denotes a nucleon and l represents a charged lepton.

Since the neutrino cross section with an orbital electron is roughly 1/1000 of the above interactions, we neglect it.

Reference [63] summarizes the basic ideas of this simulation.

3.2.1 Quasi-Elastic Scattering Mode

This interaction occupies about 60% of the total neutrino interactions at an energy region around 1GeV. This scattering is a 2-body reaction, hence, out-going lepton momentum is definitely determined, once Q^2 ($Q^2 = -\mathrm{q}^2 = -(p_\nu - p_\mu)^2$ 4-momentum transfer) is given.

We take account of the form factors of nucleons since they have an internal structure. The hadron current part of the neutrino-nucleon interaction has the vector and axial vector form factors. This hadron current is expressed as follows[80];

$$< N'|J_{had}|N >= cos\theta_c \bar{u}(N')\Big[\gamma_\lambda F_V^1(Q^2) + \frac{i\sigma_{\lambda\nu}q^\nu \xi F_V^2(Q^2)}{2M} + \gamma_\lambda\gamma_5 F_A(Q^2)\Big]u(N), \qquad (3.2)$$

where F_V^1, F_V^2, F_A are the vector and axial vector form factors and expressed as follows.

$$F_V^1(Q^2) = \Big(1 + \frac{Q^2}{4M^2}\Big)^{-1}\Big[G_E^V(Q^2) + \frac{Q^2}{4M^2}G_M^V(Q^2)\Big], \qquad (3.3)$$

$$\xi F_V^2(Q^2) = \Big(1 + \frac{Q^2}{4M^2}\Big)^{-1}\Big[G_M^V(Q^2) - G_E^V(Q^2)\Big], \qquad (3.4)$$

$$G_E^V(Q^2) = \frac{1}{\Big(1 + \frac{Q^2}{M_V^2}\Big)^2}, \quad G_M^V(Q^2) = 1 + \frac{\xi}{\Big(1 + \frac{Q^2}{M_V^2}\Big)^2}, \quad \xi \equiv \mu_p - \mu_n = 3.71 \qquad (3.5)$$

$$F_A(Q^2) = \frac{-1.23}{\Big(1 + \frac{Q^2}{M_A^2}\Big)^2}, \quad M_V = 0.84(GeV^2/c^2), M_A = 1.01(GeV^2/c^2) \qquad (3.6)$$

where θ_c, M, M_V and M_A represent the Cabbibo angle, mass of nucleon, the vector mass and the axial vector mass. The latter two are determined by e-p and ν-p scattering experiments. The M_A value has a 10% uncertainty.

Finally, the Q^2 dependence of this reaction is expressed by following formula;

$$\frac{d\sigma^{\nu,\bar{\nu}}}{dQ^2} = \frac{M^2 G_F^2 cos^2\theta_c}{8\pi E_\nu^2}\Big[A(Q^2) \mp B(Q^2)\frac{(s-u)}{M^2} + C(Q^2)\frac{(s-u)^2}{M^4}\Big], \qquad (3.7)$$

where G_F is the Fermi constant, $(s-u) = 4ME_\nu - Q^2 - m^2$: m is the mass of lepton.

$$\begin{aligned}
A(Q^2) &= \frac{(m^2+Q^2)}{4M^2}\Big[\Big(4+\frac{Q^2}{M^2}\Big)|F_A|^2 - \Big(4-\frac{Q^2}{M^2}\Big)|F_V^1|^2 + \frac{Q^2}{M^2}|\xi F_V^2|^2\Big(1-\frac{Q^2}{4M^2}\Big) + \\
&\quad \frac{4Q^2 F_V^1 \xi F_V^2}{M^2} - \frac{m^2}{M^2}\Big(|F_V^1 + \xi F_V^2|^2 + |F_A|^2\Big)\Big], \\
B(Q^2) &= \frac{Q^2}{M^2}F_A\Big(F_V^1 + \xi F_V^2\Big) \\
C(Q^2) &= \frac{1}{4}\Big(|F_A|^2 + |F_V^1|^2 + \frac{Q^2}{M^2}|\frac{\xi F_V^2}{2}|^2\Big)
\end{aligned} \qquad (3.8)$$

Figure 3.10 shows the total cross section of $\nu_\mu n \to \mu^- p$ and $\bar{\nu}_\mu p \to \mu^+ n$ with M_A=1.01±0.10, compared with the experimental data. They are consistent within 10% uncertainty of M_A.

We take into account the Fermi motion and the Pauli blocking effect in nuclei. The Fermi momentum distribution is estimated from the e-^{12}C scattering experiments in the ^{16}O case. The Fermi gas model is adopted to simulate the Pauli blocking and the momentum of a recoil nucleon is restricted to be larger than the Fermi surface momentum. (217MeV/c in ^{16}O case)

We also take account of the NC elastic scattering although most of this interaction is invisible with our detector. The total cross section is estimated by the following ratio of NC to CC cross sections according to Ref.[84, 85] .

$$\begin{aligned}
\sigma(\nu p \to \nu p) &= 0.153 \times \sigma(\nu n \to e^- p) \\
\sigma(\nu n \to \nu n) &= 1.5 \times \sigma(\nu p \to \nu p) \\
\sigma(\bar{\nu} p \to \bar{\nu} p) &= 0.218 \times \sigma(\bar{\nu} p \to e^+ n) \\
\sigma(\bar{\nu} n \to \bar{\nu} n) &= 1.0 \times \sigma(\bar{\nu} p \to \bar{\nu} p)
\end{aligned}$$

3.2.2 Single Pion Production Mode

The single pion production mode is the next dominant interaction to the quasi-elastic scattering mode. This interaction produces one lepton and one pion through the following reactions.

- Charged current

$$\begin{aligned}
\nu n &\to l^- p\pi^0 & \bar{\nu} n &\to l^+ n\pi^- \\
\nu n &\to l^- n\pi^+ & \bar{\nu} p &\to l^+ n\pi^0 \\
\nu p &\to l^- p\pi^+ & \bar{\nu} p &\to l^+ p\pi^-
\end{aligned}$$
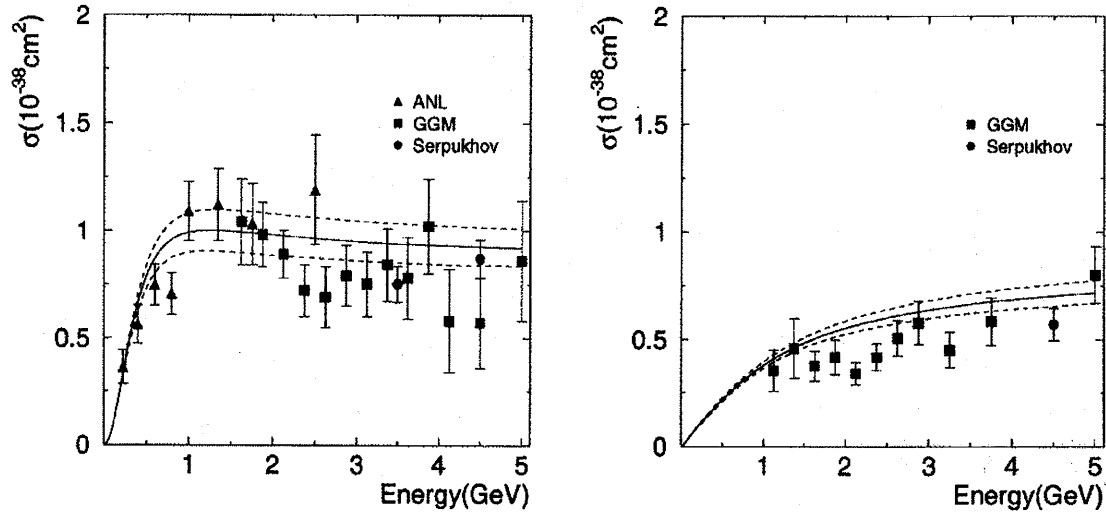
Figure 3.10: Calculated total cross sections of $\nu_\mu n \to \mu^- p$ (left) and $\bar{\nu}_\mu p \to \mu^+ n$(right) compared with the experimental data, ANL[81], GGM[82] and Serpukhov[83]. Upper and lower dashed lines show the cross section with M_A=1.11 and 0.91, respectively.

- Neutral current

$\nu n \to \nu n \pi^0$	$\bar{\nu} p \to \bar{\nu} p \pi^0$
$\nu p \to \nu p \pi^0$	$\bar{\nu} p \to \bar{\nu} n \pi^+$
$\nu n \to \nu p \pi^-$	$\bar{\nu} n \to \bar{\nu} n \pi^0$
$\nu p \to \nu n \pi^+$	$\bar{\nu} n \to \bar{\nu} p \pi^-$

This simulation is performed based on the Rein-Sehgal's model [86]. This model calculates the interaction through the following two parts;

$$\nu + N \to l + N^*$$
$$N^* \to \pi + N'$$

where, N^* is a baryon resonance state. In this model, $\Delta(1232)$ and other 17 resonance states with a mass below 2GeV/c^2 are considered.

To obtain the cross sections, the amplitude $|T(\nu N \to l N^*)|$ of each resonance production is calculated taking the interferences among the resonances into account and then multiplied by the probability of decay into one pion and one nucleon, where we restrict that the hadronic invariant mass W to be less than 2.0GeV/c^2 to keep consistency with the multi pion production mode described in Subsection 3.2.3.

Figure 3.11 and 3.12 shows the total cross sections for charged current and neutral current interactions, compared with the experimental data.
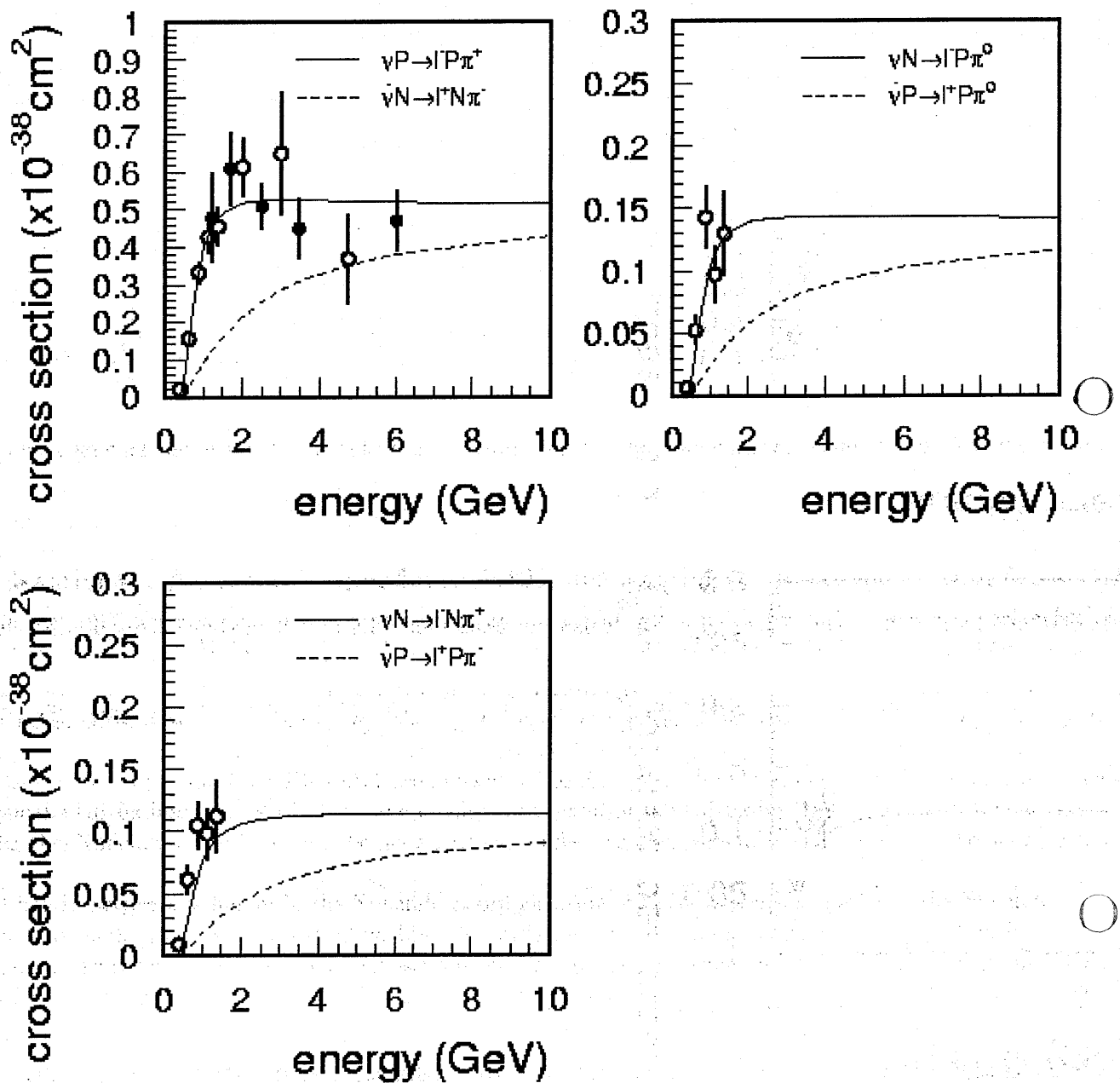
Figure 3.11: Calculated cross sections of the charged current single pion production reaction. Open circles with error bars show the result of the ANL experiment[81], and closed circles show that of the GGM experiment[82].

NC single-π production
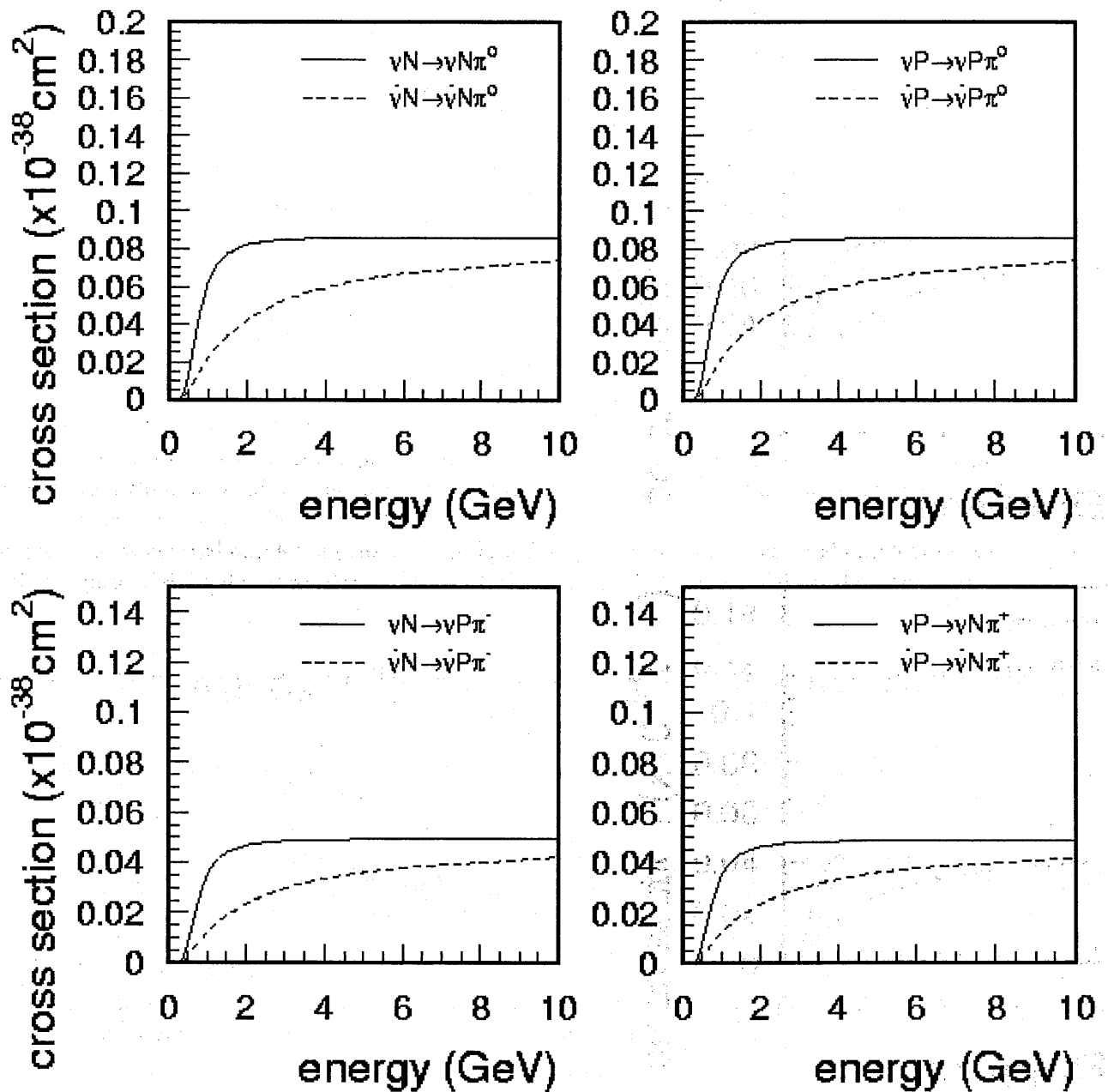
Figure 3.12: Calculated cross sections of the neutral current single pion production reaction.

The angular distribution of a pion from the $\Delta(1232)$ resonance is also calculated using the Rein Selgal's model. However, for other resonances, it is assumed to be isotropic in the rest frame of the πN system.

3.2.3 Multi Pion Production Mode

We assume that the multi pion production interaction occurs at $W > 1.4\text{GeV/c}^2$. The cross section and kinematics of this interaction is calculated based on the Bjorken scaling. The differential cross section using the Bjorken scaling parameters is expressed;

$$\frac{d^2\sigma^{\nu,\bar{\nu}}}{dxdy} = \frac{G_F^2 M_N E_\nu}{\pi} \cdot \left[(1 - y + \frac{1}{2}y^2 + C_1)F_2(x) \pm y(1 - \frac{1}{2}y + C_2)[xF_3(x)] \right]$$

where,

$$C_1 = \frac{m^2(y-2)}{4M_N E_\nu x} - \frac{M_N xy}{2E_\nu} - \frac{m^2}{E_\nu^2}$$

$$C_2 = -\frac{m^2}{4M_N E_\nu x}$$

(3.9)

where,

G_F	Fermi constant,
E_ν	neutrino energy,
M_N	mass of nucleon,
m	mass of lepton,
E_l	lepton energy,
x	Bjorken scaling parameter ($= Q^2/(2M(E_\nu\text{-}E_l)+M^2)$) and
y	Bjorken scaling parameter ($= (E_\nu\text{-}E_l)/E_\nu$).

The nucleon structure functions, $F_2(x)$ and $F_3(x)$, are calculated from the result of the GRV94[87] fitting. The CC total cross section is obtained by integrating the equation above. Results of the integration are shown in Fig. 3.13.

In the case $1.4\text{GeV/c}^2 < W < 2.0\text{GeV/c}^2$, final states of pions are taken into account employing the following facts;

1. Multiplicity of charged pions $\langle n_c \rangle$ was measured by a 15-foot bubble chamber at Fermi National Laboratory[89]. It is found to be $(0.06 \pm 0.06) + (1.22 \pm 0.03) lnW^2$. We estimated the averaged pion multiplicity $\langle n_\pi \rangle$ including neutral pions, as follows;

$$\langle n_\pi \rangle = 0.09 + 1.83 lnW^2$$

where, we assume $\langle n_{\pi^+} \rangle = \langle n_{\pi^-} \rangle = \langle n_{\pi^0} \rangle$ and $\langle n_{\pi^+} \rangle = 1/2\langle n_c \rangle$.
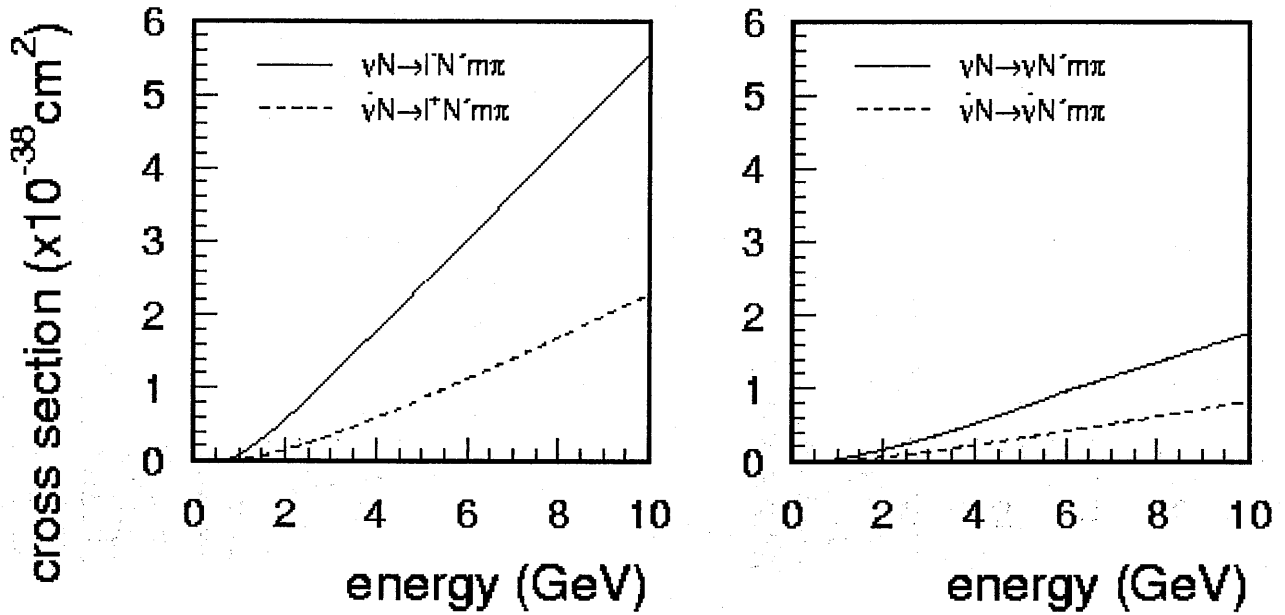
Figure 3.13: Calculated cross section of multi pion production interaction.

2. We adopt the Koba-Nielsen-Olesen(KNO) scaling which reproduces a reaction process $\bar{\nu}_\mu p \to \mu X^{++}$ in BEBC[90] data, in order to determine the pion multiplicity in each event.

3. The charge of each hadron is randomly chosen under the charge conservation.

4. We consider the Δ appearance phenomenon in the final state since a bubble chamber experiment in Argonne clearly measured the Δ production in multi-hadron final states[91]. This Δ effect modifies the phase space.

5. We also consider a forward-backward asymmetry measured by the BEBC data. $\langle n_\pi^F \rangle \langle n_\pi^B \rangle = (0.35+0.41 \, lnW^2)/(0.50+0.09 \, lnW^2)$

6. For the neutral current, the NC/CC cross section ratio is estimated by Reference[92] in an energy range of $E_\nu <3$GeV, and by Reference [93] in an energy range of $E_\nu >3$GeV.

$$\frac{\sigma(\nu N \to \nu X)}{\sigma(\nu N \to l^- X)} = \begin{cases} 0.26 & (E_\nu <3\text{GeV}) \\ 0.26 + 0.04(E_\nu/3 - 1) & (3\text{GeV}<E_\nu <6\text{GeV}) \\ 0.30 & (6\text{GeV}<E_\nu) \end{cases}$$

$$\frac{\sigma(\bar{\nu}N \to \bar{\nu}X)}{\sigma(\bar{\nu}N \to l^+X)} = \begin{cases} 0.39 & (E_\nu <3\text{GeV}) \\ 0.39 + 0.02(E_\nu/3 - 1) & (3\text{GeV}<E_\nu <6\text{GeV}) \\ 0.37 & (6\text{GeV}<E_\nu) \end{cases}$$

In a kinematical region $W >2.0\text{GeV}/\text{c}^2$, we use JETSET/PYTHIA[88] instead of the set above. Thanks to this adoption, kaons, etc. are automatically taken into account.

3.2.4 Coherent Pion Production Mode

The coherent pion production interaction means that a neutrino interacts with the whole nucleus coherently. We consider the following processes.

$$\nu N \to l^- N \pi^+$$
$$\bar{\nu}N \to l^+ N \pi^-$$
$$\nu N \to \nu N \pi^0, \quad \bar{\nu}N \to \bar{\nu}N \pi^0$$

where $l^\pm$ is a charged lepton and N is a nucleus. The angular distribution of the pions produced by this process has a sharper peak at the forward direction than other processes and the nucleus itself does not break up. The energy transfer in this interaction is negligible small.

The cross section and kinematics of this interaction is calculated employing the Rein-Sehgal model[94]. This model refers to the Adler's partially conserved axial vector current theory[95].

$$\frac{d^3\sigma}{dxdyd|t|} = \frac{G_F^2 M_N E_\nu}{\pi^2} \frac{1}{2} f_\pi^2 A^2 (1-y) \frac{1}{16\pi} \left[\sigma_{tot}^{\pi N}\right]^2 (1+r^2) \left(\frac{M_A^2}{M_A^2 + Q^2}\right)^2 e^{-b|t|} F_{abs}$$

$$r = \frac{Re f_{\pi N}(0)}{Im f_{\pi N}(0)}$$

where,

G_F	Fermi constant,
E_ν	neutrino energy,
M_N	mass of nucleon,
E_l	lepton energy,
x	Bjorken scaling parameter ($= Q^2/(2M(E_\nu-E_l)+M^2)$),
y	Bjorken scaling parameter ($= (E_\nu-E_l)/E_\nu$),
t	momentum transfer to nuclear ($=(p_\pi-q)^2$) and
f_π	decay constant of pion.
b	80GeV^{-2}
A	nucleon number of the nucleus
F_{abs}	$F_{abs} = e^{-<x>/\lambda}$, $\lambda^{-1} = \sigma_{inel}^{\pi N}\rho$, ρ is nucleus density,
$<x>$	Mean free path of the pion in nucleus

Figure 3.14 shows the total cross section of the coherent pion production reaction on ^{16}O as a function of neutrino energy. As explained before, the coherent pion production mode is neglected in iron case.
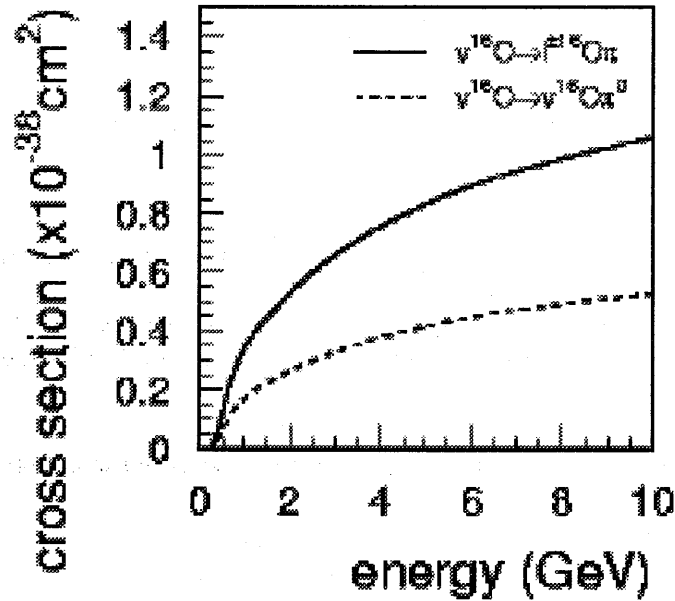
Figure 3.14: Calculated cross section of coherent pion production off ^{16}O nuclei.

3.3 Simulation of Super-Kamiokande

Super-Kamiokande detects Cherenkov light photons generated by charged particles and reconstruct images of the Cherenkov rings. We adopted the GEANT[64] codes to trace the particles and the photons and to simulate the detector response.

The CALOR[66] program is used for the hadronic interactions in water. However, in an energy range of $E_\pi < 500$ MeV, the CALOR does not reproduce experimental data well [123]. Therefore when the pion momentum is less than 500 MeV/c, we developed our own program which use the $\pi - {}^{16}O$ cross section estimated by the data from the $\pi - {}^{12}C$ scattering [124] and the $\pi - p$ scattering [125] experiments.

The tracking of the photons are made by our original codes after the GEANT program simulates the emittion of Cherenkov light photons by charged particles. For photons with short wavelength, an interaction with water molecules or particles of which size is smaller than wavelength, the Rayleigh scattering, is dominant. For longer wavelength, an absorption and a scattering with particles which is roughly same in size as the wavelength, The Mie scattering. In our simulation, we consider the Rayleigh scattering, the Mie scattering and the absorption. Figure 3.15 shows the attenuation length of Cherenkov light photons in our
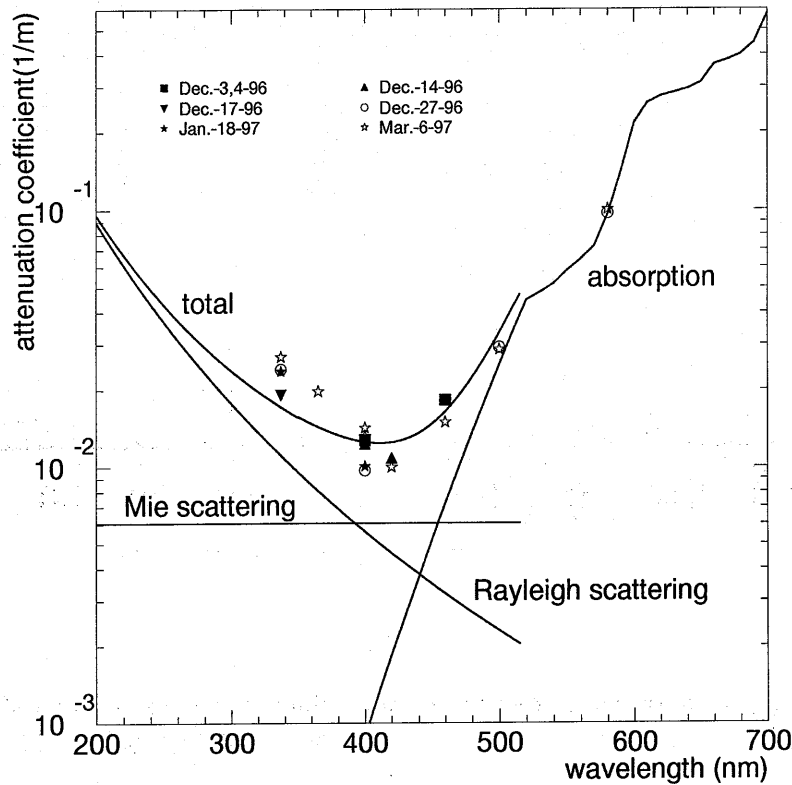
Figure 3.15: Various marks show the measured attenuation coefficient as a function of wave length. Solid lines show the attenuation coefficient used in the Monte Carlo program.

simulation program, as a function of wavelength. Absorption is dominant above 450 nm in wavelength. We used the data given by Ref. [126] for the attenuation coefficient of absorption. The absolute re-normalization factors of the scattering are tuned to reproduce the experimental results measured by a laser calibration system (Fig 3.15).

The reflection and absorption at the surface of the PMTs and the black sheets as a function of incident angle are included in the simulation program taking the photon polarization effect into account. The quantum efficiency and the response of a PMT have been measured. We also take them into account in the Monte Carlo simulation.

Chapter 4

Measurement of Electron Neutrino Contamination at the Near Site

4.1 Outline of the analysis

In this chapter, we measure the ν_e contamination in the ν_μ beam by using the Fine Grained Detector at the near site, KEK. The expected $\nu_e(\nu_\mu)$ interaction rate averaged in the whole material of the scintillating fiber tracker (SFT), which consists of water target (5.6 ton) and the others (2.7 ton), is 1.63×10^3 (1.22×10^5) interactions/10^{20} protons on target (POT). The ν_e/ν_μ interaction ratio at the near site is expected to be only 1.3% from our beam simulation.

Electrons generated by ν_e charged current (CC) interactions in SFT are expected to go through the scintillator plane of the trigger counter (TG) and to stop in the lead glass calorimeter (LG) which has more than 20 radiation lengths along the beam axis, while muons with momentum more than approximately 360MeV/c should penetrate LG and the chambers in front of the first iron plate of MUC which is called "the first layer of MUC". In order to reduce backgrounds from low energy muons and pions, we required large energy deposit in both TG and LG for the stopping particles in LG. The number of ν_e interactions to be selected is comparable to the background from ν_μ interactions after these cuts.

On the other hand, we collect muons from ν_μ CC interactions in SFT requiring TG hits, LG hits and a muon track in MUC for normalization of our MC simulation.

After selection of electron and muon candidates, we calculate the ν_e/ν_μ interaction ratio at the near site.

4.1.1 Data for the analysis

The normal data taking started on June 3 in 1999. The target diameter was 20mmϕ in June and has been changed to 30mmϕ to increase the horn current from 200kA to 250kA since November 1999. The neutrino yield and energy spectrum should be different between the June and November configurations. In this chapter, the data taken in the November configuration (from Nov. 1999 to June 2000) is employed to measure the flux ratio of electron and muon neutrinos.

The total number of protons delivered to the target for the period between November 1999 and June 2000 was 2.1×10^{19}POT without beam tuning. After selection of runs with good FGD condition, Total number of spills used for analysis with FGD is 2,688,825 spills which corresponds to 1.44×10^{19} POT.

The neutrino beam is generated by the accelerator in $1.1\,\mu$sec pulse with a duty cycle of 2.2sec. An event trigger is generated in synchronization with the beam extraction timing signal, called spill gate, sent from the accelerator. Only one neutrino interaction can occur in a spill since the rate is expected to be ~0.005 interactions/spill. Thus, we consider one neutrino-induced event corresponds to one spill in this analysis. Afterwards in this chapter, we use the word event in counting the spills.

4.2 Selection for neutrino-induced muons and electrons

In the first place, low-energy beam-induced neutron events and low-energy cosmic-ray particles are rejected by requairing a mimimum energy deposit in the trigger counter (TG) and the lead glass counter (LG).

The remaining background, i.e., cosmic-ray muons hit LG and TG without hitting VETO and MUC. To eliminate them, we reconstruct the particle track by using the hits in LG and TG. If the extrapolated track is out of geometric acceptance of VETO and MUC, the event is rejected.

4.2.1 Selection criteria common to muons and electrons

1. Require the energy deposit > 5 MeV in the central region of the trigger counter within a time gate of beam spill to reject low-energy beam-induced neutron or cosmic-ray muon events.

   The particles produced in the material of the scintillating fiber tracker (SFT) are required to penetrate the trigger counter. The hit timing and position in the trigger counter is calculated from the time information of PMTs at both ends of the scintillator. The energy deposit in the trigger counter is required to be larger than 5 MeV, while the average energy deposit by a muon is expected to be 8 MeV. Furthermore, to select the neutrino interactions, we require the hit timing in the trigger counter is inside a spill gate with 1150 nsec time width as shown in Fig. 4.1. In this figure, 9-bunch structure is clearly seen.

   It is also required that the hit position is inside the central $200\,\text{cm} \times 200\,\text{cm}$ region of the scintillator plane of the trigger counter because SFT is 240 cm in width and 240 cm in height. The deposit energy distribution after the timing cut and the position cut is shown in Fig. 4.2. A clear peak made by the penetrating particles can be seen. The energy threshold of the counter is low enough to detect muons.

2. Require the energy deposit in the lead glass calorimeter > 100 MeV to reject edge-clipping cosmic-ray particles.
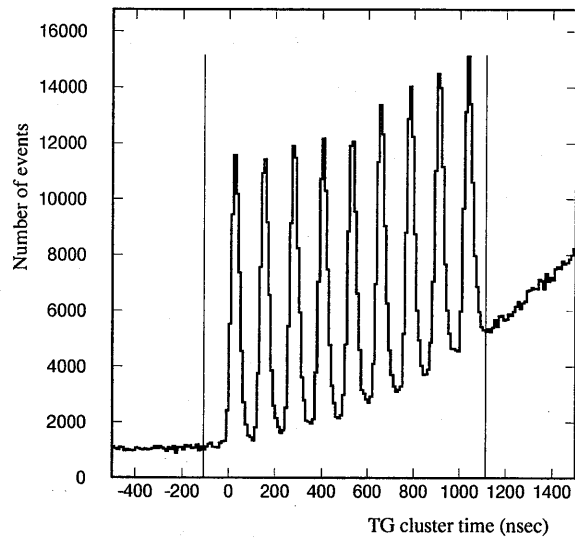
Figure 4.1: Timing distribution of the hit in the trigger counter. The spill gate is defined between -50nsec and 1100nsec.
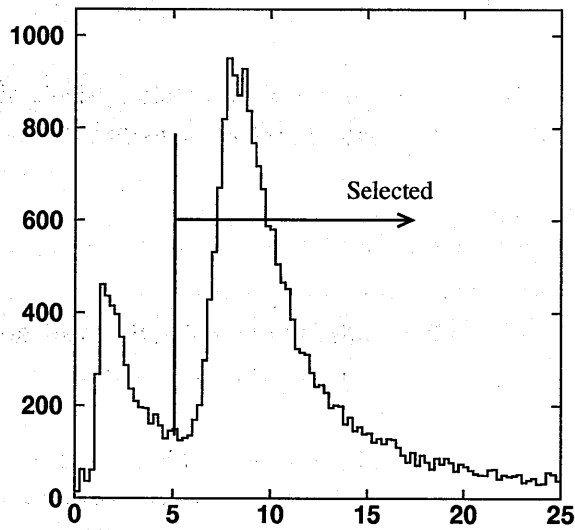
Figure 4.2: The deposit energy distribution of the trigger counter after the timing cut and the position cut. The low-energy cosmic ray or beam induced neutrons are rejected.

The particles penetrating the trigger counter are required to reach the lead glass counter. At least one cluster with larger than 100 MeV in the lead glass counter is required. Figure 4.3 show the energy distribution.
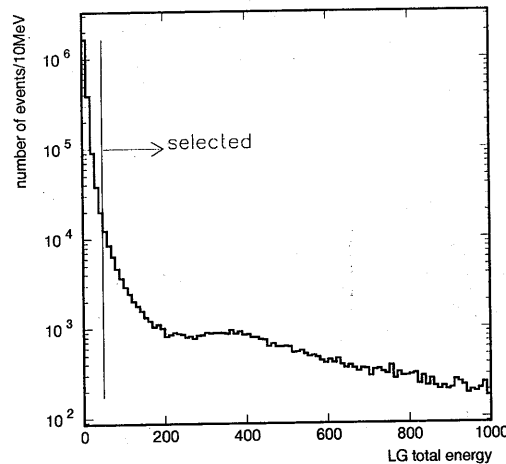
Figure 4.3: Energy distribution of LG clusters. Rejected low-energy backgrounds are thought to be clipping cosmic-ray particles.

3. Reject cosmic-ray muons which hit only the trigger counter and the lead glass counter.

The veto counter (VETO) is located upstream of the trigger counter (TG) and the lead glass calorimeter (LG), and the muon range chamber (MUC) is located downstream of them. The remaining background is cosmic-ray muons which hit both TG and LG without crossing VETO and MUC. To distinguish such cosmic rays from the neutrino-induced particles, we require that the exptrapolated line connecting the hit clusters of the lead glass calorimeter and the trigger counter should cross both the veto counter and the first layer of the muon range chamber.

For the extrapolated track to VETO, it should cross within ±150 cm in the horizontal and vertical axis, while VETO is 466 cm in width and 430 cm in height. In case of MUC, the extrapolated track should be within ±250 cm in both axes, while it covers ±380 cm in both axes.

4. Reject beam-induced and cosmic-ray muons coming from the upstream the veto counter (VETO cut).

The incoming beam-induced muons into SFT should hit the veto counter (VETO) in coincidence with hitting the trigger counter (TG). If one or more hits exist in VETO

within ±20 nsec near the TG hit time after time-of-flight (TOF) subtraction assuming the light velocity, the event is rejected. The distribution of the time difference between TG and VETO hits after TOF subtraction is shown in Fig. 4.4
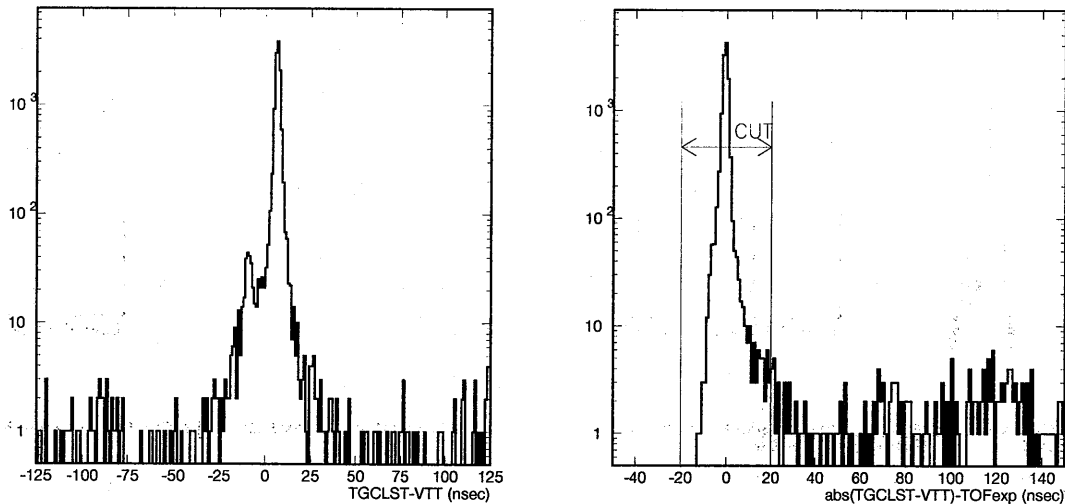
Figure 4.4: The time difference between the hits in TG and those in VETO (left) and the distribution after subtracting the time of flight assuming the light velocity (right). In the left hand figure, cosmic-ray muons which make the smaller peak around -10 nsec and neutrino-induced muons upstream of VETO corresponding to the larger peak around 10 nsec are rejected.

4.3 Muon Sample

4.3.1 Selection for the Muon Sample

A muon produced by a ν_μ CC interaction in the material of SFT penetrates LG and leaves a track in MUC starting from the first layer before the first iron plate. First of all, for the muon selection, tracks in MUC found by the MUC tracker are required to originate in the first layer and not to escape from MUC. The selection criteria are listed below:

1. Require the muons to enter MUC passing the effective area of the first layer.

   A muons penetrating LG leaves a track starting from the first layer in MUC. The MUC tracks starting before the first iron plate are selected. The effective area is defined as follows:

$$|MUCSTAX| < 300cm \quad and,$$

$$|MUCSTAY| \quad < \quad 300cm \quad and,$$
$$MUCSTAZ \quad < \quad 430cm, \tag{4.1}$$

where MUCSTAX, MUCSTAY and MUCSTAZ are the track starting position along the horizontal, vertical and beam axis fitted by the tracking program in MUC, respectively. The distribution of track starting points in MUC is shown in Fig. 4.5.
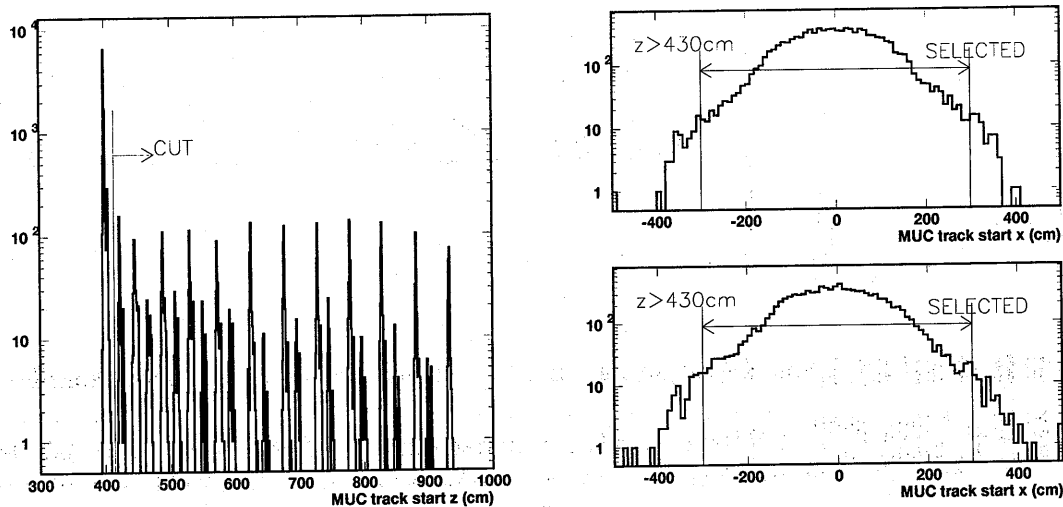
Figure 4.5: MUC track start position distribution. The left figure shows the distribution along the beam axis (z-position), and the upper (lower) right figure is a projection on to the horizontal (vertical) axis after the z-position cut. The neutrino interactions in the iron plate and incoming cosmic-ray muons are rejected by the z-position cut and the horizontal (vertical) position cut, respectively.

2. Require the muons to stop inside MUC.

The muons entering in front of MUC are required to stop inside it. The end point distribution after the start point cut required above is shown in Fig. 4.6. The muons stopping in the boxes shown in the figure are selected.

Finally, the matching between the track and the hit position of TG and LG is examined. The matching resolution between the LG cluster and the extrapolation from the selected MUC track is calibrated using muons coming upstream of SFT. Such muons are tagged by the time of flight measured by the scintillator planes of VETO and TG. All the conditions to select muon sample except for the TOF cut is also required. The matching resolution is estimated to be 10.7cm and 13.4cm for the horizontal and the vertical position, respectively. For the hit in the scintillator, TG, the resolution is 7.0cm and 6.2cm for the horizontal and the vertical position, respectively.
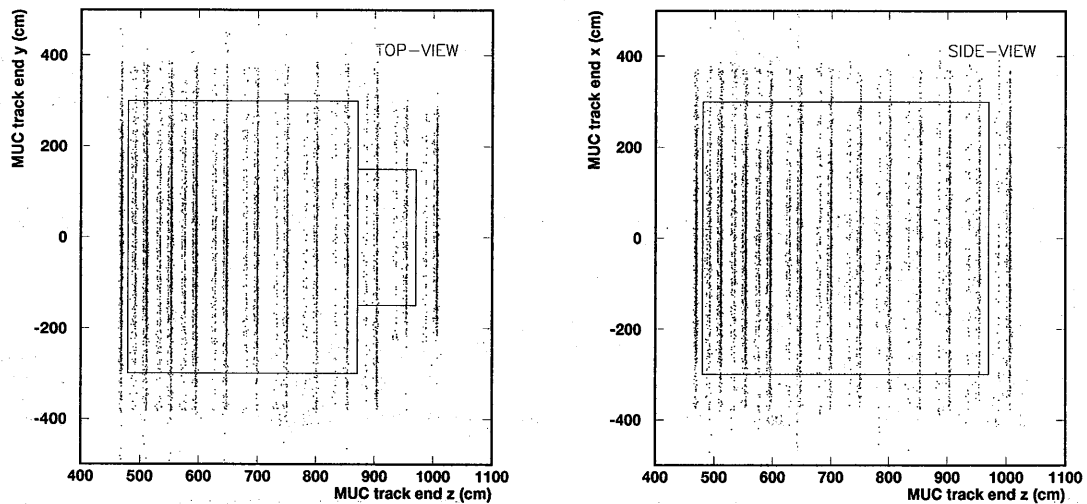
Figure 4.6: MUC track end position distribution after the start position cut. Dots show the end points of data and boxes shows the selected region. The vertical axis of the right (left) figure provides the x-z (y-z) view, where x axis is defined as the horizontal one and y axis as the vertical one. The horizontal axis of the both figures represents the stopping position along the beam axis. Cosmic-ray muons entering at the side or the upside MUC are rejected.

The extrapolation of tracks from MUC onto the front surface of the lead glass calorimeter (the trigger counter) is compared with the position of the LG (TG) hit cluster. To evaluate the matching of the TG,LG cluster positions to the MUC track, The χ^2 is defined as follows:

$$\chi^2_{MUCmatch} = \sum_i^{LG,TG} \left(\left(\frac{x_c^i - x_e^i}{\sigma_x^i} \right)^2 + \left(\frac{y_c^i - y_e^i}{\sigma_y^i} \right)^2 \right) , \qquad (4.2)$$

where x_c^i, y_c^i are the horizontal and vertical cluster position, x_e^i, y_e^i are the extrapolated position of the MUC track on the each detector surface. Muons are selected by requiring $\chi^2 < 7.78$ corresponding to 90% C.L. for 4 degrees of freedom.

The number of events at each reduction step is summarized in Table 4.1. A total of 1591 events are selected as the muon sample induced by ν_μ CC interactions in the neutrino target of SFT.

	data	ν_μ MC
Common selection for muons and electrons	3737	34641
MUC track start point	2346 (62.8%)	21851 (63.1%)
MUC track end point	1983 (84.5%)	18729 (85.7%)
MUC track matching	1591 (80.2%)	15132 (80.8%)

Table 4.1: The number of events in muon selection for data and ν_μ MC at each reduction step. The reduction factor at each step is also shown in the parentheses.

4.3.2 Background against ν_μ-induced muons in the Muon Sample

The ν_μ interactions in the detector material other than SFT may induce background muons against the ν_μ interactions in SFT. Monte-Carlo study shows approximately 14% (0.01%) of the ν_μ interactions in TG (LG) is expected to contaminate the muon sample.

If we normalize the MC sample to the muon data sample 1591 events, a total number of background muons is estimated to be 16 as listed in Table 4.2. Subtracting the small background, the number of muons induced by the ν_μ interactions in SFT is estimated to 1575 ± 40(stat.) events.

Target	number of events
SFT (Signal)	1575
TG (Background)	13
LG (Background)	3
Total	1591

Table 4.2: The contents of the muon sample estimated by the MC simulation normalized to the data.

4.4 Electron sample

4.4.1 Selection for the electron sample

The electrons by ν_e CC interactions in SFT are selected after the common selection for muons and electrons described in Sub-section 4.2.1.

A ν_e event is not accompanied with a muon track in the muon range chamber (MUC), because almost all the produced charged pions stop at the first iron plate of MUC and are not recognized as muons. An electron coming from SFT is expected to stop in the lead glass calorimeter, while a muon can punch it through with the momentum larger than $\sim$360 MeV/c. Furthermore, an electron produced by ν_e interactions has a larger energy deposit than the secondary particles induced by ν_μ.

Therefore, we can select electrons induced by ν_e CC interactions in SFT by applying the following selection. The selection is divided into 3 steps, i.e., (1) muon track rejection (2) LG-stopping particle selection (3) energy deposit cut. The details of each step are described below.

Muon track rejection

If a muon track in MUC is associated with the hit cluster in LG, the event is rejected in order to cut the ν_μ CC events. The matching is examined between all the tracks starting from the MUC first layer (MUSTAZ < 430cm) and all the LG clusters. If at least one track matches the LG cluster within 32.1cm in the horizontal and within 40.3cm in the vertical direction corresponding to the 3σ confidence level, the event is rejected.

Selection for electrons stopping in LG

The most upstream chamber layer of MUC is composed of 4 sublayers (2 horizontal and 2 vertical) before the first iron plate of MUC. Since all of the electrons are expected to stop in LG, they cannot hit chamber cells of MUC located behind LG, although the electric noise may induce one or more hits. On the other hand, muons which go through LG can hit 4 or more chamber cells in the first layer.

Thus, we search for a combination of the LG and TG clusters which have no or one sublayer hit in MUC within 100 cm around the extrapolated line between them as shown in Fig. 4.7. If at least one such combination exists, the event is selected as an electron event.

Energy Deposit Cut

A muon leaves a lower energy deposit than an electron in LG, around 400 MeV electron-equivalent energy as confirmed in the cosmic-ray test. In order to reduce the contamination of ν_μ interactions in the electron sample, an energy cut is applied to the selected combination of the LG and TG clusters. The energy threshold is set to 20 MeV for the TG clusters, and 1 GeV for the LG clusters. Figure 4.8 shows the energy distribution of the TG clusters and
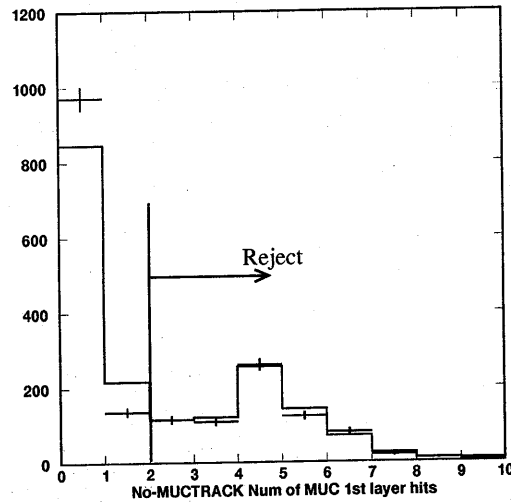
Figure 4.7: The number of hit cells in the MUC first layer distribution. The histogram corresponds to the ν_μ MC normalized to the data by entries.

the LG clusters for the particles stopping in LG (LG-stopping sample). A total of 25 events remained as the electron event candidates.

The electron sample selection is summarized in Table 4.3.

	data	ν_μ MC	ν_e MC
Common selection for muons and electrons	3737	3710.1	47.6
Muon Track Rejection	1627	1611.1	47.2
LG-stopping	978	933.5	43.6
Energy Deposit Cut	25	10.2	10.2

Table 4.3: Summary of the electron selection. The results for ν_μ and ν_e MC (generated corresponding to 1.37×10^{20}POT) normalized to the muon data sample (1.44×10^{19}POT) are also shown.

4.4.2 Background against ν_e events in the electron sample

As listed in Table 4.3, a total of 10.2 ν_μ interactions in SFT make backgrounds against ν_e events.

Furthermore, the neutrino interactions in the detector material other than SFT have to be considered. When a neutrino generates pions or other particles in LG backward, they are regarded as contamination to the electron sample. In the MC simulation, five events out of
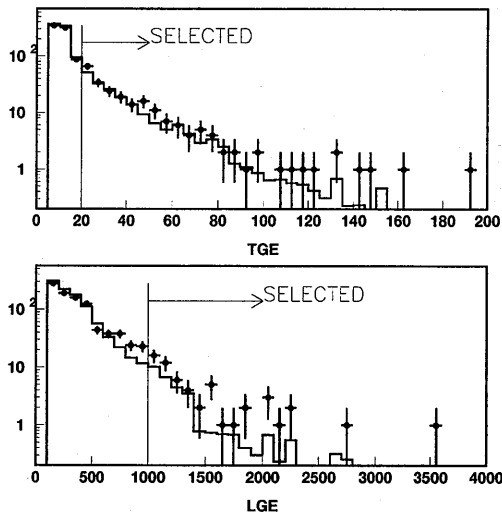
Figure 4.8: The energy distribution of the TG (upper figure) and LG (lower figure) clusters. The histogram shows the ν_μ MC normalized by the muon sample.

148,981 ν_μ interactions in LG (corresponding to 8.11×10^{19}POT) pass the electron selection criteria. If we normalize the number of interactions in LG by 1.44×10^{19}POT (present data), the number of background in LG is estimated to be $0.87 \pm 0.40(MCstat.)$ events by the MC simulation. Also ν_μ interactions in the TG counters are considered and 0.21 events are selected in the electron sample. The number of generated MC events in TG is 16858 corresponding to 26×10^{20}POT.

In total, the background is estimated to be 11.3 events, which is consistent with the observed number of ν_e events of $13.7 \pm 5(stat.)$.

4.5 Observed ν_e/ν_μ interaction ratio at the near site

The number of neutrino interactions can be calculated from the number of muons and electrons by the following formula:

$$R\left(\frac{N_{\nu_e}}{N_{\nu_\mu}}\right) = \frac{(N_e - N_{eBG})/\epsilon_e}{(N_\mu - N_{\mu BG})/\epsilon_\mu} , \tag{4.3}$$

where N_{ν_e}, N_{ν_μ}, N_e, N_μ, N_{eBG} and $N_{\mu BG}$ are the number of ν_μ, ν_e interactions in SFT, observed number of events in the electron and muon sample, and expected number of background events in the electron and muon sample, respectively. The detection efficiency for ν_e (ν_μ) is represented by ϵ_e (ϵ_μ).

The detection efficiency for ν_e and ν_μ is summarized in Table 4.4.

	ν_μ	ν_e
Common selection	21.5%	21.4%
Muon selection	9.32%	0.0516%
Electron selection	0.0541%	4.64%

Table 4.4: The detection efficiency for ν_μ and ν_e interactions in SFT.

The observed number of interactions in SFT is $(1.690 \pm 0.044(\text{stat.})) \times 10^4$ for ν_μ and $(2.97 \pm 1.08(\text{stat.})) \times 10^2$ for ν_e respectively. Therefore, the measured ν_e/ν_μ interaction ratio in SFT is $(1.76 \pm 0.62(\text{stat.}))$ %.

4.6   Estimation of systematic errors

Various systematic errors in the ν_e/ν_μ interaction ratio are estimated in this section. According to Eq. 4.3, the uncertainty in the common selection for muons and electrons cancel out since the efficiency difference is very small (21.5% vs 21.4%). However, the muon selection and the electron selection have different systematics in general to be investigated.

4.6.1   The uncertainties in the Electron Selection

MUC First Layer Hits

The electron events are required to have one or no hits in the MUC first layer. However, there is some discrepancy between the data and MC in the distribution of the number of the MUC first layer hits shown in Fig. 4.7. There seems to exist some additional hits around the extrapolated point from the connecting line between the TG and LG hits in MUC. To estimate the fraction which has more than 2 additional hits, the distribution for the muon sample is used. If a muon goes through the MUC first layer, there should be 4 hits typically since there are 4 sublayers of chamber cells in front of the first iron plate. The fraction which has 6 or more hits is 9.4% for data and 10.3% for MC (Fig. 4.9), and the difference is 9.1%. The difference in the fraction is taken to be the systematic error in the MUC first layer hits.

Energy deposit of ν_μ events

There is systematic difference in the LG and TG responses between the data and MC for the events induced by ν_μ interactions. The ν_μ enriched sample is selected in the low energy region of the TG and LG counters.

The systematic error in the TG response is estimated by using the LG-stopping events of which energy deposit in LG is less than 1 GeV. The difference in the survival efficiency in the TG energy cut between the data and MC is 9% as shown in Fig. 4.10, We assign $\pm 9\%$ to the systematic error in the TG energy cut.

Also the LG-stopping sample which deposit less than 20 MeV in TG is employed to estimate the systematic error in the LG energy cut. As shown in Fig. 4.11, The data has 59% larger
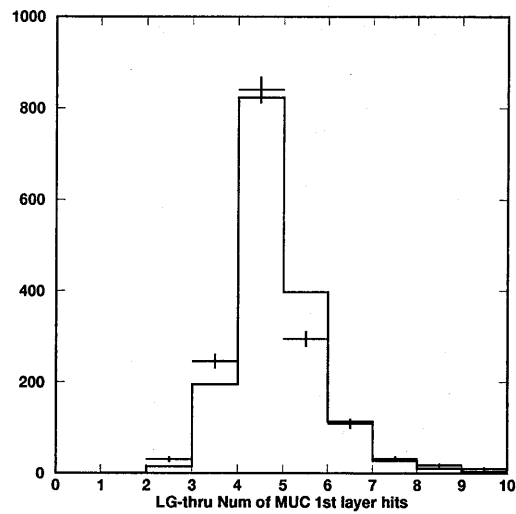
Figure 4.9: The number of hit cells in the MUC first layer distribution. The histograms correspond to the ν_μ MC normalized to the data by entries.
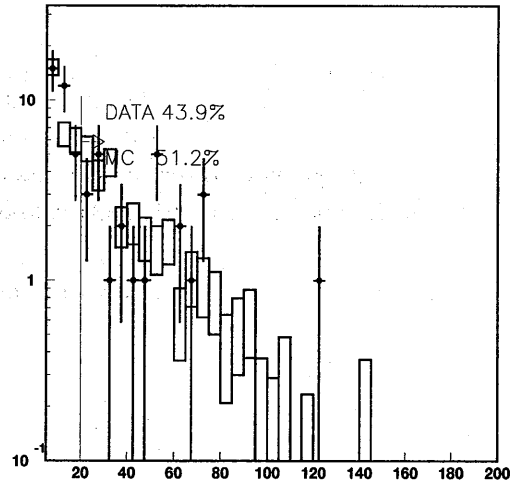
Figure 4.10: Energy distribution of the TG counter for the stopping particles in LG with less energy deposit than 1 GeV.
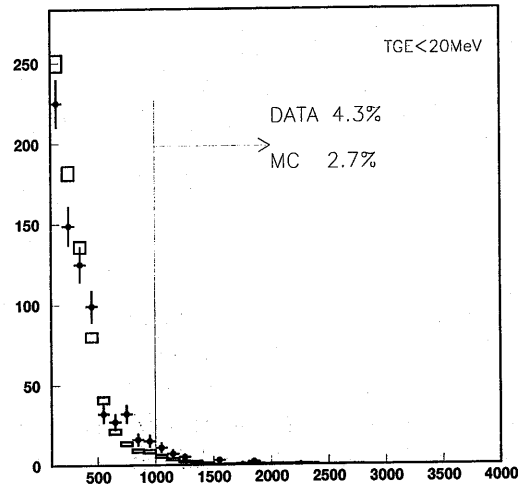
Figure 4.11: Energy distribution of the LG calorimeter for the stopping particles in LG with energy deposit in TG less than 20 MeV.

fraction in the high energy region $> 1\,\mathrm{GeV}$ than MC. Presuming the 59% excess in the data is due to background events, the ν_e/ν_μ interaction ratio becomes 44% lower. Thus $^{+0\%}_{-44\%}$ is assigned to the systematic error due to the LG response uncertainty in the ν_e/ν_μ interaction ratio.

LG Energy Scale

The LG energy scale for electrons was calibrated using the electron beam as described in Section 2.3.2. Its systematic error is estimated to be 5% from the uncertainty in gain shift between the electron calibration and the cosmic-ray muon calibration. If the LG energy scale changes by 5% at 1 GeV, the number of electron events to which the LG energy cut has been applied changes by 12%.

MC Normalization

The background against the electron sample originating from ν_μ interactions is estimated by the MC sample normalized to the muon data sample. If the normalization changes by the statistical error in the muon sample, the background rate changes by 3%.

As described in Section 4.3.2, 1% of the muon sample come from the neutrino interactions in the detector materials other than SFT. One more possible background source may be caused by the beam-induced muons which come from upstream of SFT due to the inefficiency of VETO. The efficiency of VETO was studied using the neutrino induced muons which penetrated the whole SFT along the beam axis and left tracks in SFT. It was found to be better than 97%. A

total of 2341 upstream muons are selected after the same selection criteria as the muon sample except for the requirement of the TOF cut. Due to the 3% inefficiency of VETO, approximately 70 events caused by the upstream muons can contaminate the muon sample. We assign the ratio of the contamination to the muon data sample, $70/1575 = 4.4\%$, to the systematic error in the number of events in the muon sample.

The systematic error in the ν_e/ν_μ interaction ratio due to the MC normalization uncertainty is calculated to be 5% by adding the errors above in quadrature.

Pion Production Model at the Target

The incident neutrino spectrum depends on the pion production models at the target in our beam simulation described in Section 3.1. To estimate the effect we change various input parameters by an reasonable amount in the pion production model in Eq. 3.1, where the background rate and the efficiency of the muon sample selection for ν_μ events correlatively varies. The uncertainty in the measured ν_e/ν_μ interaction ratio due to the uncertainty in the pion production modelling is estimated to be $^{+0.50}_{-0.42}$ %.

4.6.2 K/π Production Ratio at the Target

Neutrinos from kaons produced at the target give a small contribution to the neutrino production. In our beam simulation, approximately 7% of the background events in the electron sample induced by ν_μ interactions come from kaon decays. The whole contributions by kaons are taken into account in the systematic error in the background estimation for the electron sample conservatively. The error in the ν_e/ν_μ interaction ratio is calculated to be $^{+24}_{-18}$ %.

4.6.3 Neutrino Cross Section

The interaction types of the background events in the electron sample coming from ν_μ interactions are summarized in Table 4.5. Almost all the ν_μ background events come from the pion production interactions, among which 78% have energetic neutral pions greater than 1 GeV. Therefore, we estimate the uncertainty in ν_e/ν_μ interaction ratio due to pion production cross section uncertainties,

ν_μ interaction type	electron sample	muon sample
CC Quasi-Elastic	1%	52%
CC Single Pion	14%	38%
CC Multi Pion	38%	10%
NC Single Pion	26%	$\ll 1\%$
NC Multi Pion	21%	$\ll 1\%$
total	100%	100%

Table 4.5: Interaction type of the background in the electron sample by ν_μ interactions estimated by MC.

If the CC single- and multi-pion production and NC cross sections changes by $\pm 30\%$ independently, the ν_e/ν_μ interaction ratio is affected by $^{+11}_{-8}\%$.

4.7 Summary of ν_e analysis at the near site with the fine grained detector

The systematic errors in the $R\left(N_{\nu_e}/N_{\nu_\mu}\right)$ measurement with FGD is summarized in Table 4.6.

Source	Systematic error (%)
MUC First Layer Hits	9%
TG Response for ν_μ	8%
LG Response for ν_μ	$^{+0\%}_{-44\%}$
LG Energy Scale	12%
MC Normalization	5%
Pion Production at the target	$^{+29\%}_{-24\%}$
K/π ratio	$^{+24\%}_{-18\%}$
Neutrino Cross Section	$^{+11\%}_{-8\%}$
Total	$^{+43\%}_{-57\%}$

Table 4.6: Table of the systematic errors in the measurement of the ν_e/ν_μ interaction ratio in SFT.

As a result, the ν_e/ν_μ interaction ratio in SFT is measured to be:

$$R\left(N_{\nu_e}/N_{\nu_\mu}\right) = 1.76 \pm 0.62(\text{stat.})^{+0.76}_{-1.00}(\text{sys.})(\%) , \qquad (4.4)$$

while the prediction from our beam simulation is 1.33%.

Thus, it is confirmed that the ν_e contamination in our ν_μ beam is well reproduced by the beam simulation. Therefore, we use out MC simulation to estimate the ν_e contamination at Super-Kamiokande in Chapter 7.

Chapter 5

Measurement of Muon Neutrino Interaction Rate at KEK

The measurement of ν_μ interaction rate in water in the 1 kilo-ton water Cherenkov detector (KT) at the near site is described in this chapter. The measured ν_μ interaction rate in KT is extrapolated to that in the far detector, Super-Kamiokande. As KT has the same detection principle and target atoms as Super-Kamiokande, most of the systematic errors from the uncertainties in the ν_μ spectrum and neutrino-nucleus cross sections are expected to cancel out. Therefore only the experimental systematic errors proper to KT is explained in this chapter. Those which can cancel out will be described in Chapter chp:skexp.

5.1 Event selection

5.1.1 First reduction

The time structure of the neutrino beam reflects that of the accelerator beam. It comes in pulses with the $1.1\,\mu$s time width in every 2.2 s periodically. An event trigger is generated synchronizing to the beam extraction timing signal, called spill gateAt this stage, the on-spill events, which are the data taken in the spill gate, are stripped off the stored raw data which contain the calibration data together with the on-spill data.When cosmic-ray particles hit the KT detector leaving large energy deposit, a false signal created at the cable connection could be induced to the electronics at a time 1.1μs after the cosmic ray signal. In order to avoid the serious background caused by such reflection pulses, especially in the data taken before installation of buffer amps which can eliminate them without decreasing charge from PMTs, we require a condition that there should be no detector activity within the $1.2\,\mu$s interval preceding the beam spill by using the trigger timing signal recorded by TMC.

5.1.2 Single event selection

The readout electronics cannot distinguish multiple events in one beam spill correctly due to its 300ns ADC gate width and the subsequent dead time (300ns). Therefore, an analog

sum of signals from all the PMTs is recorded by transient digitizer (called "FADC") with a sampling rate of 500 MHz.

The analog sum signal (PMTSUM) from inner detector PMTs is recorded by FADC as a function of time. The pulse hieght distribution should have a peak corresponding to the time at which a neutrino interaction occurs. The height of the peak reflects the total number of photoelectrons of the inner PMTs. When multiple successive interactions occur in a spill, we can see corresponding peaks in the PMTSUM distribution recorded by FADC, while the other readout electronics (ATM) cannot record the events properly due to its dead time. In order to distinguish such multiple events in a spill, we developed a program to identify each peak in the pulse height distribution. About 3% of all the spills is expected to contain multiple interactions with ~ 100 nsec time widthin the same one bunch. In this case, we have no way to distinguish these events. This is taken into account in the systematic error.

We search a peak which exceed the threshold pulse height corresponding to 1000 photo-electrons (p.e.). Figure 5.1 shows a typical ADC threshold curve for the FADC peak selection. This threshold in the peak search is ≈ 100 MeV for an electron and can remove the contamination from μ-decay electrons by cosmic-ray stopping muons entering KT just before the beam spill. Each peak in the FADC signal is regarded as an event in KT. The number of interactions in a beam spill is counted after the first reduction and the spills which contain a single interaction are selected. Figure 5.2 shows the number of peaks recorded by FADC in a beam spill and the FADC peak time distribution of the selected events which have the clear 9-bunch structure in a spill and thus guarantee that the peaks in FADC is originated from our proton beam which have the 9-bunch micro structure.
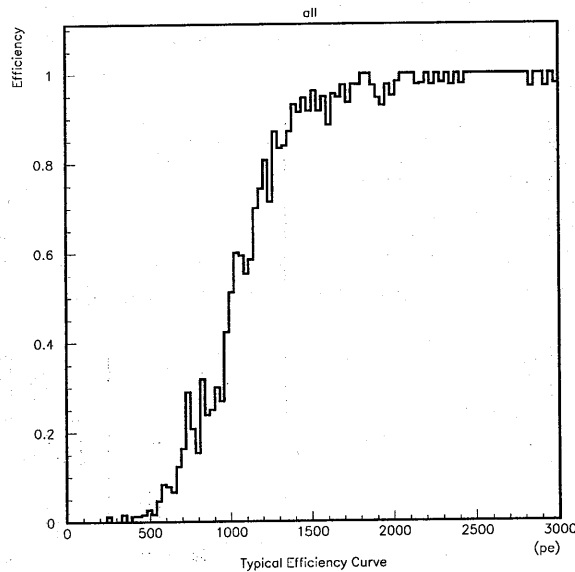
Figure 5.1: Typical threshold curve of FADC cut as a function of number of collected photoelectrons by inner PMTs.
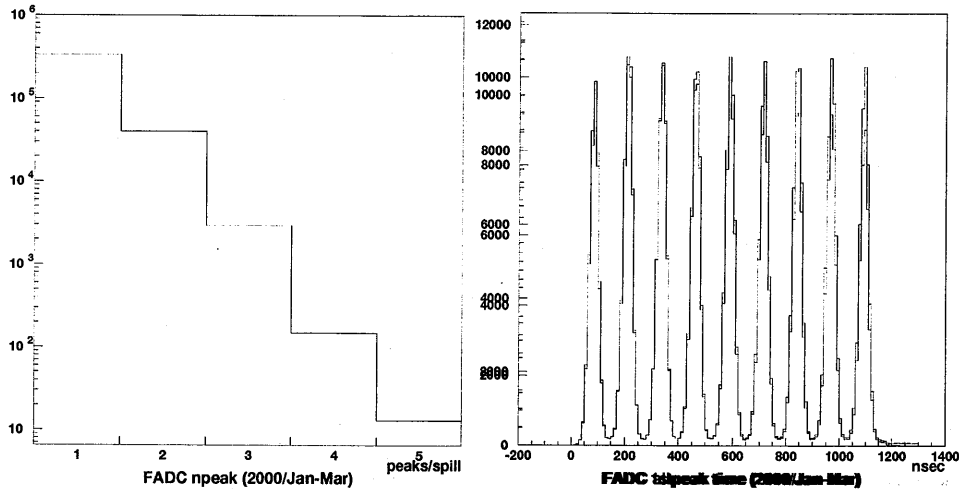
Figure 5.2: Number of peaks recorded by FADC (left figure) and the time distribution of the peaks (right figure). Only single peak events in a beam spill are selected for analysis.

5.1.3 Fiducial volume cut

We need the event vertex position reconstruction to distinguish neutrino interactions in KT from incoming background events. The vertex position fitting method is based on arrival time information of Cherenkov light photons and the same method has been used in the Super-Kamiokande atmospheric neutrino analysis[127]. Details of the fitting algorithm is explained in Appendix A.

The observed neutrino events are required to have their vertex position in the fiducial volume of which the boundary is set far from the inner PMT wall enough to veto incoming background events. The cylindrical fiducial volume, 2m in radius and 2m in height, is defined along the beam axis and laid in the upstream half of the KT tank to avoid mis-fitting of vertex positions for outgoing muons (Fig. 5.3). The total fiducial mass is 25 t. The reconstructed vertex position distributions along the horizontal and vertical axes just before the fiducial volume cut are shown in Fig.5.4 and agree with our Monte-Carlo simulation.

5.1.4 Background

The average number of peaks recorded by FADC which exceed the threshold ($\sim$1000 p.e. $simeq$ 100MeV for an electron) is about 0.2/spill including entering background events due to cosmic-rays or ν_μ induced muons upstream. A part of the neutrino candidates after the fiducial volume cut was visually scanned by physicists and found 0.5% of them are found to be ν_μ induced incoming muons upstream of KT and misjudged on in-fiducial-volume event by vertex position mis-fitting. The background due to cosmic-ray muons is estimated to be 1.0% of the total neutrino candidates in the fiducial volume confirmed by applying the same cut on random triggered data as neutrino data. In June 1999 and Nov. 1999 before the installation of buffer amps, the reflection pulse in a signal cable caused by an incoming muon was not
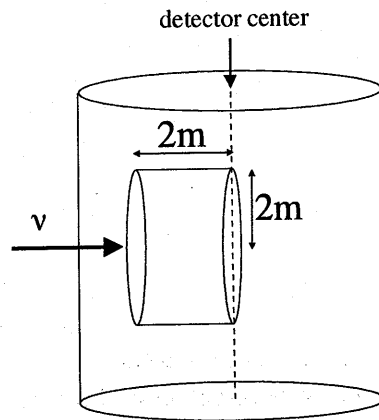
Figure 5.3: The definition of fiducial volume in KT
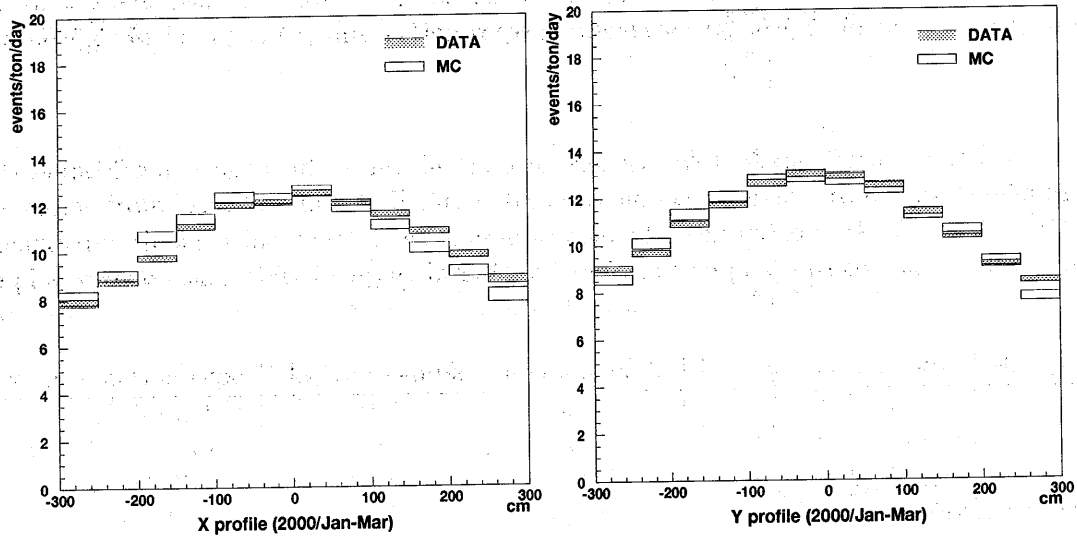
Figure 5.4: Horizontal (left figure) and vertical (right figure) vertex distributions of observed neutrino interactions at KT. The open boxes show the data and shaded boxes show the MC simulation. The vertical size of each box corresponds to its statistical error.

eliminated completely and contribute to the background events. Therefore, the background rate in June 1999 and Nov. 1999 is estimated to be 2.6% from cosmic-ray and 0.5% from ν_μ induced incoming muons slightly larger than the other months. In total, 3.1% of the observed neutrino events are regarded as the background for these 2 months.

5.2 Measured Neutrino Interaction Rate with KT

The total number of ν_μ interactions in the KT fiducial volume (N_ν^{tot}), including multiple interactions in one beam spill, is calculated from the number of neutrino events with single peak in the FADC signal (N_ν^1) observed in fiducial volume. Figure 5.5 shows the long-term stability of the event rate (N_ν^1) and it is very stable as expected.
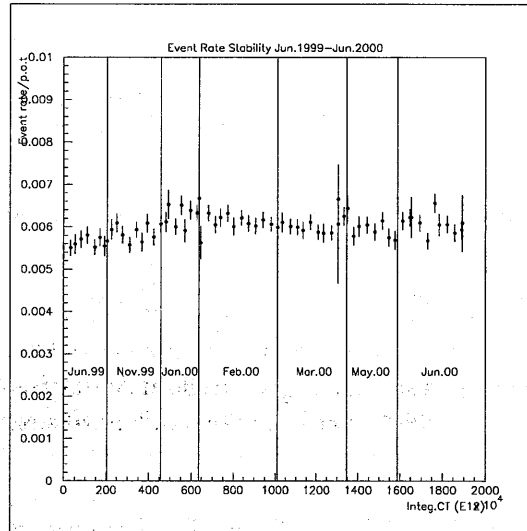
Figure 5.5: Long-term stability of the neutrino event rate observed at KT. Each point represents an event rate averaged over 2 days with a statistical error bar. In June '99, the neutrino beam intensity is lower than the other months due to the lower current in the horn magnet. In November '99, the detector configuration was slightly changed from the other period and the event rate looks slightly lower.

N_ν^{tot} should be proportional to the total number of FADC peaks in the whole on-spill data (N_{peak}^{tot}) as long as they are induced by the neutrino beam regardless of their vertex position. Therefore, we can convert the single interaction rate in a beam spill to the multiple interaction rate. The calculation is performed as follows:

$$N_\nu^{tot} = \frac{N_\nu^1}{\epsilon} \cdot \frac{N_{peak}^{tot}}{N_{peak}^1} \cdot \frac{1}{1 + R_{BG}} \, ,$$

where ϵ is the detection efficiency for ν_μ interactions in KT, N_{peak}^1 is the number of spills with single peak in the FADC signal and R_{BG} is the fraction of background in the observed ν_μ candidates.

Table 5.1 shows the summary of KT analysis for neutrino data taken from June 1999 to June 2000, where the ν_μ interaction rate is calculated each month.

In May and June 2000, the stop-timing signal to FADC from a gate-generator module were found to be drifted depending on the temperature in the electronics hut and the last 8th or 9th bunch in a beam spill, which has 9 bunches during $1.1\,\mu s$, sometimes went outside of the recording time range of FADC. Therefore, the event rate in this period is derived from the first 7 bunches by masking the last 8th and 9th bunches and scaled to the one which is expected if we could take the whole 9 bunches. The correction factor R_{9b}^{7b} is estimated from the time distribution of peaks in FADC taken in the same period where the 9th bunch can be detected with more than 99% efficiency. The formula to calculate the interaction rate in this period (May 2000 and June 2000) is modified as follows:

$$N_\nu^{tot} = \frac{N_\nu^1}{\epsilon} \cdot \frac{N_{peak}^{tot}}{N_{peak}^1} \cdot \frac{1}{1 + R_{BG}} \cdot R_{7b}^{9b} ,$$

where R_{7b}^{9b} is the correction factor to extrapolate the result of 7-bunch analysis to the 9-bunch case.

month	Jun.99	Nov.99	Jan.00	Feb.00	Mar.00	May.00	Jun.00	Total
POT ($\times 10^{18}$)	2.60	2.62	1.81	3.74	3.35	2.42	3.16	19.70
N_ν^1	4282	4923	3505	6986	6080	3574	4745	
N_{peak}^1	89782	96304	67641	140740	122651	74135	95652	
N_{peak}^{tot}	109119	118321	85238	177437	155778	88558	114739	
ϵ	0.706	0.708	0.719	0.724	0.719	0.718	0.718	
R_{BG}	0.031	0.031	0.015	0.015	0.015	0.015	0.015	
R_{7b}^{9b}	-	-	-	-	-	1.282	1.283	
N_ν^{tot} ($\times 10^4$)	0.7150	0.8286	0.6052	1.1985	1.0581	0.7510	1.0021	6.159
$N_\nu^{tot}/$POT ($\times 10^{15}$)	2.755	3.169	3.338	3.207	3.161	3.100	3.170	3.126

Table 5.1: Summary of the neutrino event rate in KT. The 7-bunch analysis described in the text is applied for May 2000 and June 2000 data. The event rate in June 1999 is lower than the other months due to lower current in the horn magnet.

5.3 Systematic Errors in KT Event Rate

The systematic errors in ν_μ interaction rate measured by KT is estimated in this section.

Fiducial Volume

The event rate is defined in the fiducial volume of $-200cm < z < 0cm$ where the profile of the reconstructed vertex shows a good agreement between the data and MC (Fig. 5.6). There are systematic difference in the vertex position distribution outside the fiducial volume, which come from mis-fitting of outgoing muons. The systematic error from the vertex position resolution is estimated by comparing the observed event rate in several fiducial volume definitions

with MC (Table 5.3). The $\pm 4\%$ spread including statistical error from the standard cut is assigned as the systematic error of the vertex position reconstruction.
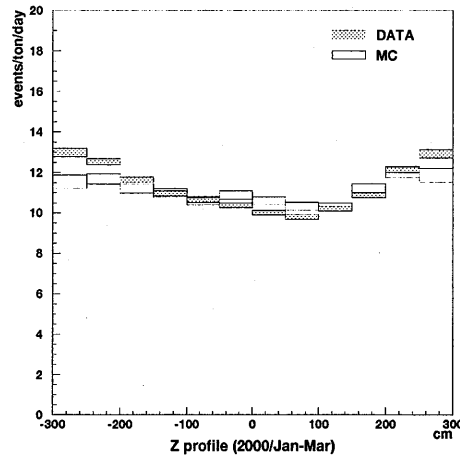
Figure 5.6: The profile of the observed events along the beam axis. The upstream part, $-200cm < z < 0cm$, is defined as the fiducial volume. The open boxes show the data and the shaded boxes show the MC. The vertical height of each box corresponds to its statistical errors.

z window	DATA/MC
$-200cm < z < 0cm$	1.00
$-300cm < z < 0cm$	$1.03 \pm 0.01(stat)$
$-200cm < z < 200cm$	$0.97 \pm 0.01(stat)$
$-200cm < z < 300cm$	$0.99 \pm 0.01(stat)$
$-200cm < z < 450cm$	$1.02 \pm 0.01(stat)$

Table 5.2: Comparison of the event rate with several fiducial volume cuts. The z coordinate with its origin set at the KT detector center is defined along the beam axis

FADC threshold

The threshold of FADC is set at 1000 p.e. of all the inner PMTs and its fluctuation is estimated to be 10%. When the threshold in the MC sample changes by 10% from 1000 p.e., the event rate to be observed changes by less than 1%, thus we assign $\pm 1\%$ for the systematic error in the FADC single peak cut.

Energy Scale

The energy scale of the KT detector is calibrated to 5% accuracy confirmed by cosmic-ray through-going and stopping muons. If the energy scale of the MC sample changes by 5%, the

ν_μ event rate changes by less than 1%. Therefore, we assign $\pm$1% systematic error in the ν_μ event rate due to the energy scale uncertainty.

Multiple Interactions in One Bunch

When two or more interactions occur in the same bunch of a beam spill, the peak search algorithm in the FADC signal sometimes fails to identify them and regards them as a single peak event. Adding the ν_μ interaction rate 0.39 events/spill to the background event rate (cosmic-ray or ν_μ induced muons produced upstream) 0.12 events/spill, the probability that one bunch contains two or more ν_μ interactions or incoming muons is about 3%. Therefore, 3% of the total number of ν_μ interactions with a single peak recorded by FADC may have multiple interactions in one bunch. Hence, the fraction 3% is assigned to the systematic error in the measurement of ν_μ event rate in KT.

Background events

The statistical error in the background estimation due to incoming cosmic-ray muons and ν_μ induced muons is taken as the systematic error in the background rate R_{BG}. 1% is assigned in Jun 1999 and Nov 1999 data and 0.5% to the other months.

Correction Factor for 7-bunch Analysis

To May and June 2000 data, the 7-bunch analysis masking the last 8th and 9th bunches in a spill is applied. The statistical error in the calculation of the correction factor R_{7b}^{9b} is 1%. For estimation of the validity of this analysis method, the other data from Jan. 2000 to Mar. 2000 is analyzed by this method and the difference between the 7-bunch analysis and the 9-bunch analysis is found to be at most 0.4%.

Also, the vertex position mis-fitting caused by the signals belonging to the masked bunches is considered. When FADC signals in the 8th and 9th bunches are masked, the signals recorded by ATM which are regarded as a single FADC peak event in the 7-bunch analysis are sometimes accompanied by those from interactions belonging to the 8th or 9th bunches because the ADC gate width of ATM is about 300ns corresponding to 3 bunches in a beam spill. In such case, the vertex position fitter failed by approximately 0.6% of the events selected by the 7-bunch analysis. In total, 1.2% is assigned to the systematic error caused by masking the 8th and 9th bunches in May and June 2000 data.

1/4 disconnection to FADC (FADC error)

In Nov. 1999, one of the cables which bring an analog-summed signal of the one forth of inner PMTs to FADC is disconnected by mistake. This affected the detection efficiency slightly ($\sim$ 1%) lower, thus 1% is assigned to another systematic error in the FADC peak search.

ν_μ spectrum and cross section

The fraction of neutral current (NC) in the total ν_μ-nucleus cross section has a large

uncertainty[92, 93]. When we change the fraction of NC by 30%, the ν_μ detection efficiency in KT changes by $^{+4.2\%}_{-5.1\%}$.

Also the ν_μ energy spectrum affects the detection efficiency. The effect is estimated to be $^{+2.6\%}_{-3.1\%}$ for the overall detection efficiency by taking into account the uncertainty in the PIMON analysis[100], which measure the pion kinematics just after the production at the target in this experiment.

Summary of the KT Systematic Error

The experimental systematic errors in the measurement of ν_μ interaction rate in KT are summarized in the Table 5.3.

		Jun.99	Nov.99	Jan.00	Feb.00	Mar.00	May.00	Jun.00
(A)	Fiducial Volume	4%	4%	4%	4%	4%	4%	4%
(B)	FADC threshold	1%	1%	1%	1%	1%	1%	1%
(C)	Energy Scale	1%	1%	1%	1%	1%	1%	1%
(D)	Multi Interaction	3%	3%	3%	3%	3%	3%	3%
(E)	Background	1%	1%	0.5%	0.5%	0.5%	0.5%	0.5%
(F)	R^{9b}_{7b}	-	-	-	-	-	1.2%	1.2%
(G)	FADC error	-	1%	-	-	-	-	-
(H)	ν_μ spectrum	$^{+2.8\%}_{-4.0\%}$	$^{+2.0\%}_{-1.8\%}$	$\rightarrow$	$\rightarrow$	$\rightarrow$	$\rightarrow$	$\rightarrow$
(I)	NC/CC	$^{+4.2\%}_{-5.1\%}$	$^{+4.2\%}_{-5.1\%}$	$\rightarrow$	$\rightarrow$	$\rightarrow$	$\rightarrow$	$\rightarrow$
$(A)-(H)$	Total	$^{+6.0\%}_{-6.6\%}$	$\pm5.7\%$	$^{+5.6\%}_{-5.5\%}$	$^{+5.6\%}_{-5.5\%}$	$^{+5.6\%}_{-5.5\%}$	$\pm5.7\%$	$\pm5.7\%$
$(A)-(I)$	Total	$^{+7.3\%}_{-8.4\%}$	$^{+7.1\%}_{-7.6\%}$	$^{+7.0\%}_{-7.5\%}$	$^{+7.0\%}_{-7.5\%}$	$^{+7.0\%}_{-7.5\%}$	$^{+7.1\%}_{-7.6\%}$	$^{+7.1\%}_{-7.6\%}$

Table 5.3: Summary of the experimental systematic errors in KT measurement for each month.

Chapter 6

Neutrino Events at Super-Kamiokande

6.1 Selection Criteria for Neutrino Events at SK

Neutrinos produced by the accelerator at KEK propagate through the 250 km thick rock layer in the Earth and are then detected by the Super-Kamiokande detector located 250km downstream of KEK. The Super-Kamiokande detector is operated in the self-trigger mode by itself as is described in Chapter 2. A self-triggered event is stored with the Universal Time Coordinated (UTC) time stamp from the global positioning system (GPS) at Super-Kamiokande. Also the UTC start time of each spill is recorded using the GPS system at KEK. In order to identify the beam-induced events in Super-Kamiokande, the time difference $\Delta(T)$ is defined as:

$$\Delta(T) \equiv T_{SK} - T_{KEK} - TOF \; ,$$

where TOF is the time of flight of a neutrino, T_{KEK} is the KEK-PS beam spill start time and T_{SK} is the SK trigger time. The neutrino induced events with $\Delta(T)$ distributing around the beam spill gate with $1.1\mu s$ time width are regarded as the events induced by the neutrino beam coming from KEK. Since the uncertainty in the synchronization accuracy between the two sites measured by the atomic clock is $< 200\,ns$, the beam-induced events are selected conservatively in a $1.5\,\mu s$ gate.

Data reduction and event reconstruction similar to those used in the atmospheric neutrino analyses in SK[128, 129] are applied to select fully contained (FC) neutrino interactions.

The details of selection criteria are explained below:

1. Decay electron cut

   We require that there should be no event during the $30\mu s$ time interval preceding the event to remove decay electron events from in-coming cosmic-ray muons. Dead time factor caused by this selection is less than 1/1000 since the total event rate triggered by the inner detector except the SLE trigger is typically $\sim$10Hz. The time window is set to $|\Delta(T)| < 500\mu s$ at this stage to display the distribution of parameters to select neutrino events used in the following selection.

2. PE(300ns) > 200 $p.e.$

PE(300ns) is defined as the maximum of total number of photo-electrons observed in the inner detector in a sliding 300nsec window. It is required that PE(300ns) is larger than 200. This cut is applied to reduce low-energy background events from gamma rays from the surrounding rock and so on (200 p.e. corresponding to approximately 20 MeV deposited energy). This 300ns time window reduces noise hits while keeping the signal hits high. Fig. 6.1 shows the distribution of PE(300ns) for the data and for the MC sample.
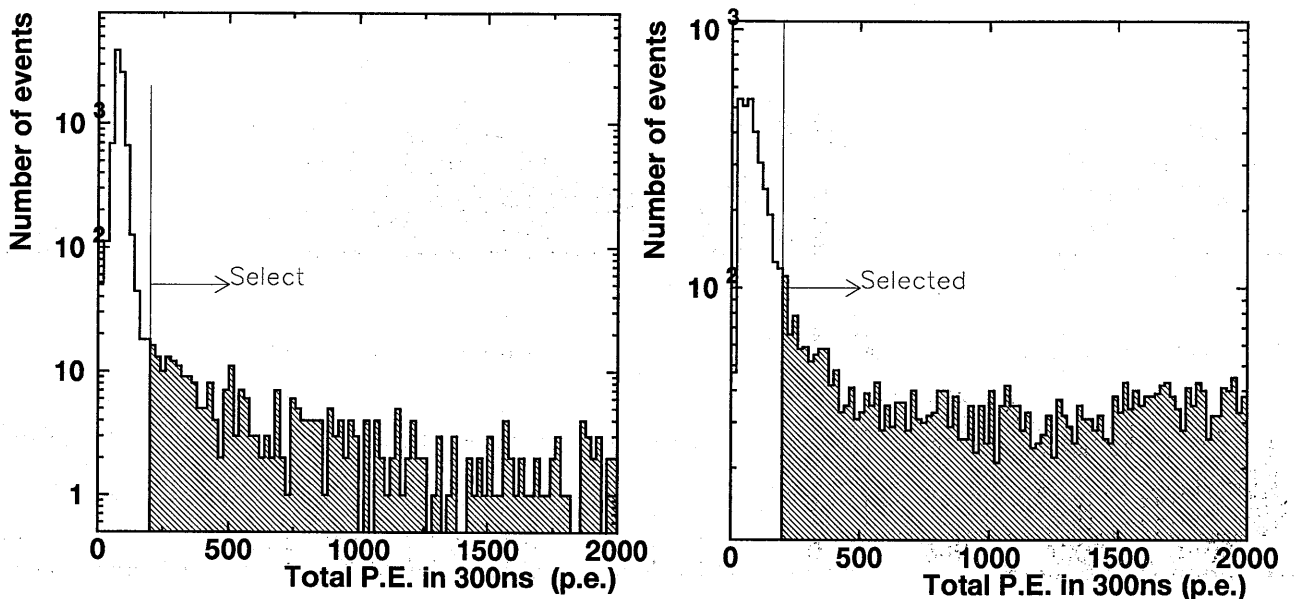
Figure 6.1: Number of total photo-electrons in 300ns time window in SK for data (left figure) and for MC (right figure) after the decay electron cut. Most of unselected events in the MC sample are generated by NC interactions, while these in data are from the low-energy events like gamma rays from the rock.

3. Flasher cut

After the PE(300ns) cut, most of the remaining background against the beam-induced neutrino events are noise events called "flasher" which are caused by a discharging PMT. One effective way to reduce the flashers is the requirement of the following condition:

$$PEMAX/PE(300ns) < 0.2,$$

where PEMAX is the maximum number of photo-electrons recorded by one inner detector PMT in an event. This rejects events in which majority of total photo-electrons in the inner detector is observed in a single PMT. The other method is also applied to eliminate the flashers. It is the same as that used in the atmospheric neutrino analysis in Super-Kamiokande using the characteristics of the flasher event like the PMT hit timing distribution in a event. From Monte-Carlo study, the efficiency decreases by only 0.8% from the situation in which the flasher cut is not applied.

4. Select fully-contained (FC) events.

   The number of hit PMTs in the largest hit cluster in the outer detector (OD) is required to be less than 10. Figure 6.2 shows distributions for the number of hit PMTs in the largest OD hit cluster. Most of cosmic-ray muon events are rejected from the data. Rejected events in the MC sample are neutrino-induced out-going muon events from the inner detector.
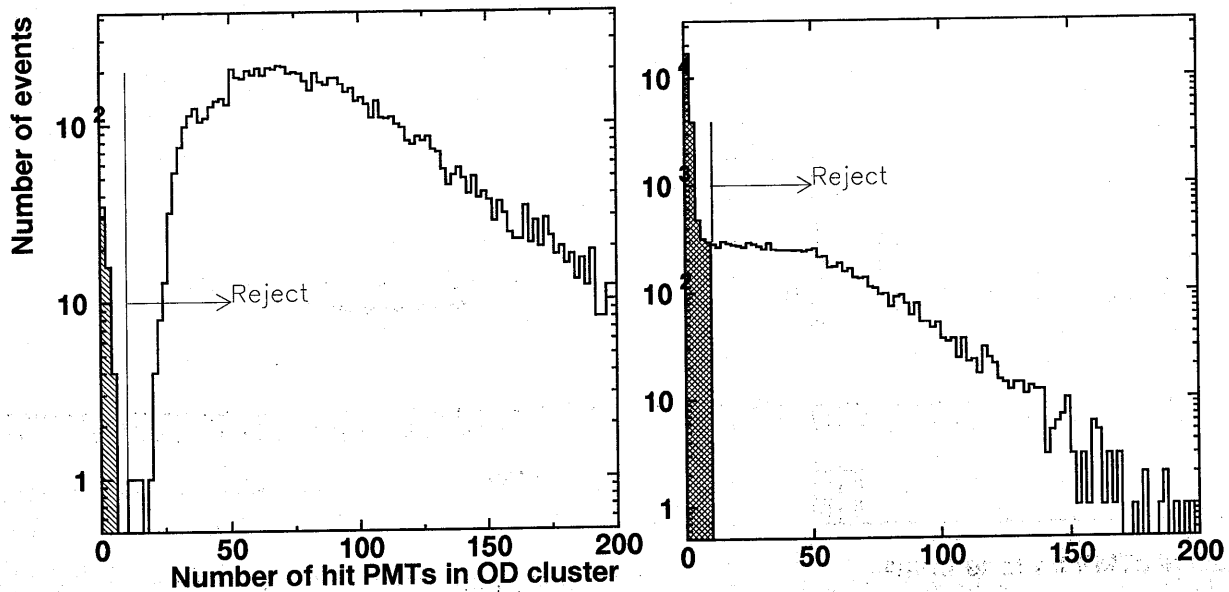
Figure 6.2: The number of PMTs in the largest OD hit cluster distribution of SK events for data (left) and for MC (right) after flasher cut. Rejected events in the MC sample are neutrino induced out-going muon events, while those of the data are cosmic-ray muon events.

5. Select the events which have an reconstructed electron-equivalent energy $\geq$ 30 MeV

   The events are required to have an energy larger than 30MeV for an electron. Instead of total number of photo-electrons, the reconstructed energy is employed, as it takes into account the vertex position, water transparency and so on. Figure 6.3 shows the reconstructed electron-equivalent energy distribution of FC events within 10 μs time window.

6. Select the events inside a tighter time window using GPS.

   The selection gate is set to $-0.2\,\mu s < \Delta(T) < 1.3\,\mu s$. Figure 6.4 shows the $\Delta(T)$ distribution at various stages of the reduction. A clear peak coincident with the neutrino beam from KEK-PS is observed in the analysis time gate. 42 FC events are observed in the inner detector (32kton).

7. Select the events in the fiducial volume.

   A fiducial volume cut is applied accepting only events with fitted vertex position inside the same 22.5 kt fiducial volume as used in the SK atmospheric neutrino analysis. The boundary of the fiducial volume is set at 2 meter distant from the nearest inner detector
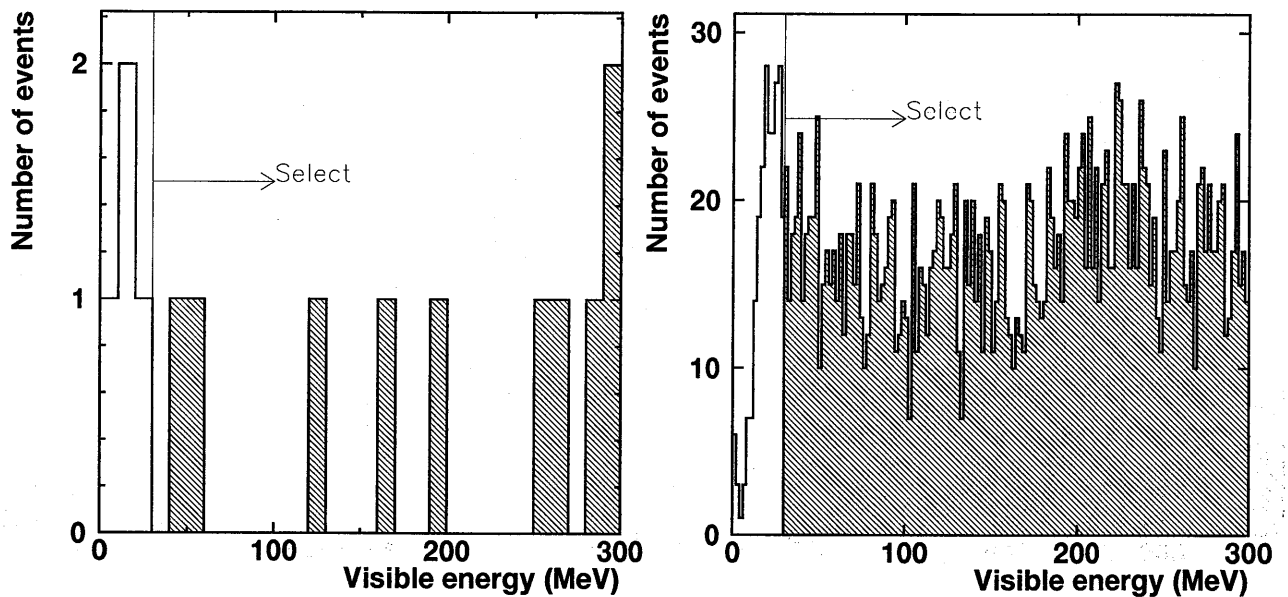
Figure 6.3: Reconstructed electron-equivalent energy distributions of SK FC events for data (left) and for MC (right) after the fiducial volume cut. Most of the unselected events in the MC sample are NC events.
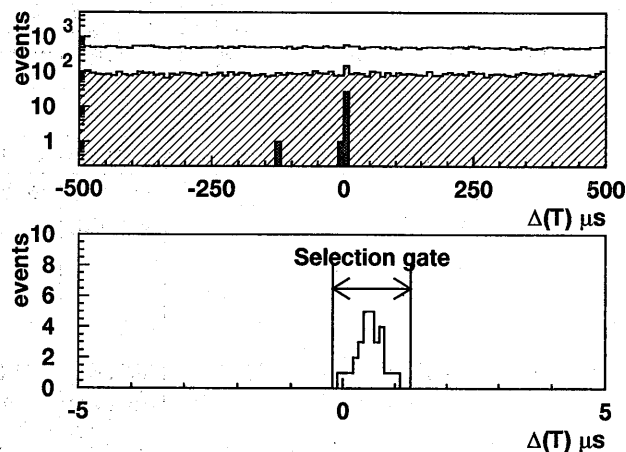
Figure 6.4: The time difference $\Delta(T)$ distribution at each step of the event selection. (top) $\Delta(T)$ distribution over a $\pm 500\,\mu s$ window. Solid histograms show the events after the decay-electron cut (criterion 1). Hatched histograms show the events after the energy cut (criterion 2). Shaded histograms show the events after fiducial volume cut (criterion 4). One off-timing event around $-130\mu s$ is thought to be an atmospheric neutrino event. The cut criteria are described in the text. (bottom) Expanded view of $\Delta(T)$ distribution within a $\pm 5\,\mu s$ window for FC events with their vertex position in the fiducial volume.
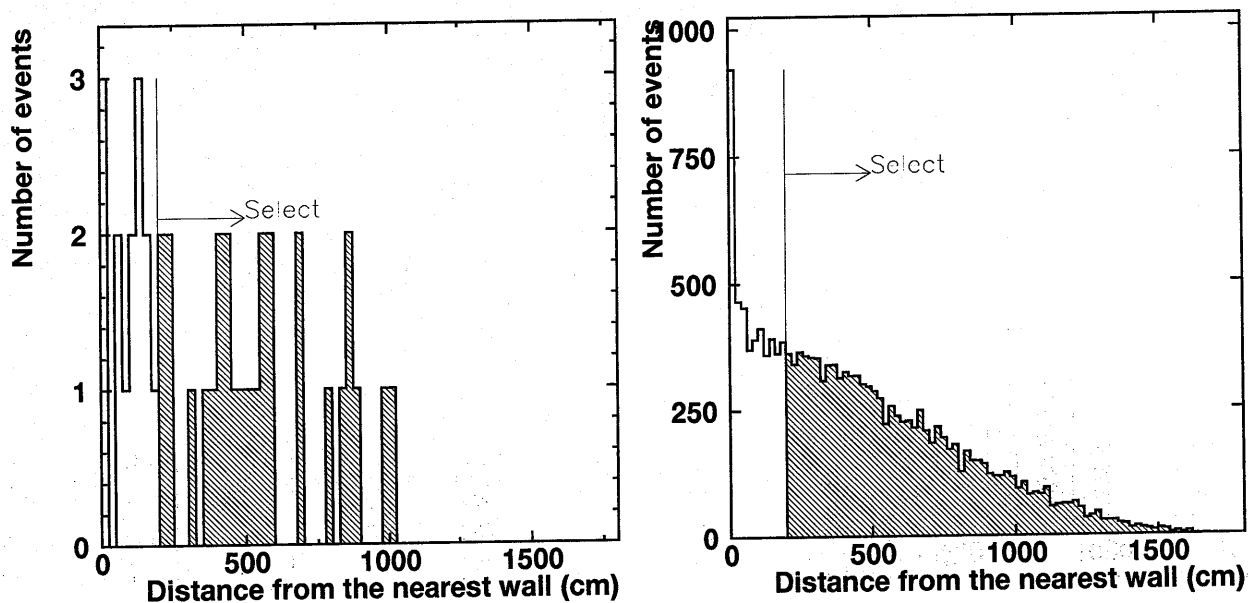
Figure 6.5: The distribution of distance from the fitted vertex position to the nearest inner wall for data (left) and for MC (right).

wall. Figure 6.5 shows a distribution of distance from the fitted vertex position to the nearest inner detector wall.

8. Select single-ring events

The events which have only one Cherenkov ring are selected to enhance CC quasi-elastic interaction events. The number of Cherenkov rings are reconstructed and counted by the same program as used in the SK atmospheric neutrino analysis[128, 129]. Figure 6.6 shows a distribution of the number of rings of the selected beam-induced FC events. The MC reproduces the data well after normalization.

9. Select e-like events with electron energy 100MeV

Finally, we require the single Cherenkov ring in a selected event should be identified as e-like, i.e. caused by electro magnetic showers of which deposit energy is larger than 100MeV by the same particle type ID program as used in SK atmospheric neutrino analysis[128, 129]. Figure 6.7 shows a particle type likelihood distribution assigned to the Cherenkov ring in the selected beam-induced FC events together the beam MC prediction, where a positive (negative) likelihood corresponds to μ-like (e-like) events. Figure 6.8 shows the expected energy distribution of the single-ring e-like MC events. The low-energy gamma-ray events produced by NC interactions can be eliminate by the 100MeV energy threshold cut.

Number of selected events at each reduction step is summarized in Table 6.1. The number of selected events fitted in the fiducial volume induced by the neutrinos produced by the accelerator at KEK is 28. Expected number of background events due to the atmospheric
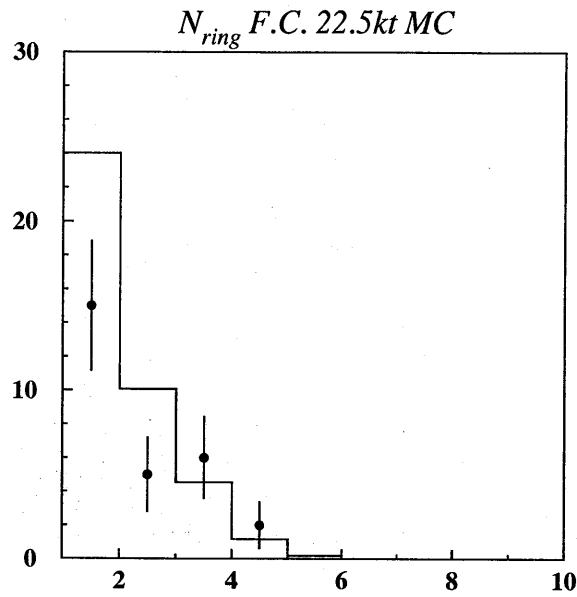
Figure 6.6: Number of Cherenkov rings distribution of the selected beam-induced FC events for data (filled circles with an error bar) and for MC (solid histograms).
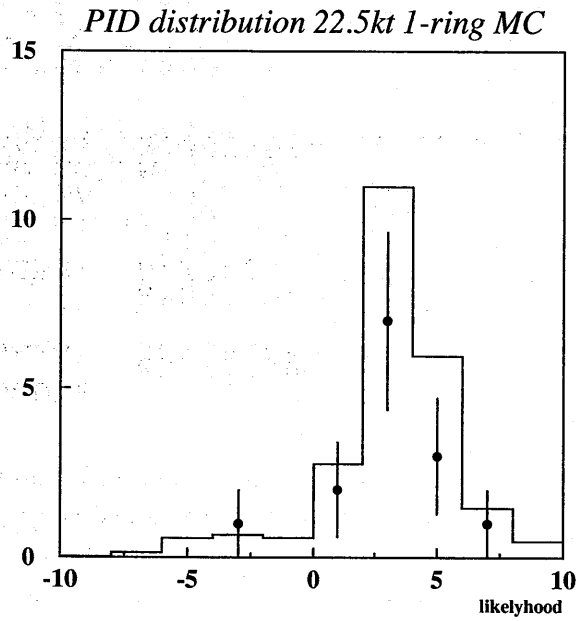
Figure 6.7: Particle type likelihood distribution of the selected beam-induced FC single-ring events, together with the MC prediction (solid histograms).
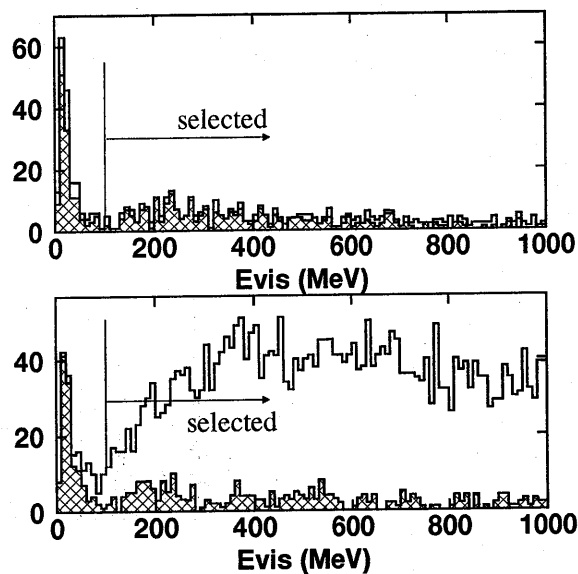
Figure 6.8: The energy distribution of FC single-ring e-like MC events. The upper (lower) figure represents that of ν_μ (ν_e) MC. Solid (Shaded) histograms show the CC (NC) interaction events. The low-energy events induced by NC interactions below 100MeV are rejected.

Selection criteria	Data	MC
analyzed number of spills	4404180	
generated		30495
$\|\Delta(T)\| < 500\,\mu s$		
HE trigger		
Decay electron cut	17102	
P.E. with 300 ns window cut	8944	18739
Flasher cut	8809	18190
Nhit PMTs in OD cut	51	15917
Reconstructed energy > 30MeV	46	15448
$-0.2\,\mu s < \Delta(T) < 1.3\,\mu s$	42	
Fiducial volume cut	28	10937
Single ring	15	6570
e-like > 100MeV	1	488

Table 6.1: Summary of the number of selected events at each step.

neutrinos are 8×10^{-4} within $1.5 \mu s$ time window [1], since we have used 4.40×10^6 spills for this analysis.

Finally, one sigle-ring e-like event is found which is consistent with the beam MC prediction of $1.92^{+0.89}_{-0.88}(sys.)$ events detailed in Chapter 7. In other words, the possible sources of this event are misidentification of a muon or a pion, an energetic neutral pion and an electron induced by beam contamination ν_e. Figure 6.9 shows the event display of this event. The reconstructed energy and direction of the ring in this event is 594MeV and 16.4 degrees from the beam axis, respectively. The reconstructed direction of this event is consistent with that on the assumption of a neutrino-neucleaon scattering, in which the variance of the neutrino-neucleaon scattering angle (σ_θ) is approximately 40 degree at 600MeV.

---

[1]The observed event rate by the atmospheric neutrinos is approximately 10 events/day in the fiducial volume of SK.

☆ Super Kamiokande ☆
NUM   1
RUN   8071
SUBRUN   41
EVENT   5487540
DATE   99-Nov- 6
TIME   15:17: 5
TOT PE: 5647.
MAX PE: 39.2
NMHIT :   2116
ANT-PE: 31.5
ANT-MX: 9.8
NMHITA: 29

90/00/00:NoYet:NoYet
90/00/00:NoYet:NoYet
90/00/00:NoYet:NoYet
90/00/00:NoYet:NoYet
90/00/00:NoYet:NoYet
90/00/00:;R= 0:NoYet
   R   :   Z   : PHI : GOOD
  0.00:   0.00: 0.00:0.000°
CANG : RTOT : AMOM : MS

RunMODE:NORMAL
TRG ID :00000111
T diff.: 644.
FEVSK :81002803
nOD YK/LW: 2/ 3
SUB EV :   0/ 0
Dec-e: 0(0/ 0/
CT: 1203
SKGPS: 94186902
          92850054
RN: 2150SP:
PSGPS: 94186902
          92767476
GPSDIF: -19.u

Comnt;

Figure 6.9: The event display of the singl-ring e-like FC event observed in Super-Kamiokande. The deposit energy is 594MeV/c. It points back to the KEK-PS ν beam with an angular deflection of 16.4 degrees.

Chapter 7

Expected Number of Neutrino Events at Super-Kamiokande

7.1 Expected number of ν_μ events at Super-Kamiokande

The expected number of ν_μ events to be observed in Super-Kamiokande is calculated in this section. The calculation of the expected number is made in the following 3 steps:

1. The ν_μ energy spectrum at Super-Kamiokande and also at a near detector, KT, is predicted by the beam simulation. The predicted spectrum and relative flux between the far site and the near site is guaranteed by PIMON analysis[100].

2. The ν_μ interaction with water target is simulated and the result is passed to the detector simulator. The ν_μ interaction and the detector simulator for KT consists of the same method as that used in Super-Kamiokande atmospheric analyses except for the size of the detector.

3. The MC sample for Super-Kamiokande is normalized by comparing the observed number of events in KT and the MC prediction and then the expected number of events at Super-Kamiokande is obtained.

The actual formula is as follows:

$$N_{\text{SK}}(\text{expected}) = \epsilon_{\text{SK}}^{\nu_\mu} \times N_{\text{SK}}^{\nu}, \tag{7.1}$$

$$N_{\text{SK}}^{\nu_\mu} = N_{\text{KT}}^{\nu_\mu} \times \frac{\eta_{\text{SK}}}{\eta_{\text{KT}}} \times \frac{POT_{\text{SK}}}{POT_{\text{KT}}}, \tag{7.2}$$

$$\eta \equiv M_{\text{fid}} \times \int dE_\nu \phi \times \sigma, \tag{7.3}$$

where $N_{\text{KT}}^{\nu_\mu}$ is the measured number of ν_μ interactions at the KT detector, $\epsilon_{\text{SK}}(\epsilon_{\text{KT}})$ is the overall detection efficiency of Super-Kamiokande (KT), $\frac{\eta_{\text{SK}}}{\eta_{\text{KT}}}$ is the Near-to-Far ratio of the number of ν_μ interactions, and $POT_{\text{SK}}(POT_{\text{KT}})$ is the integrated number of protons on target used for the analysis of Super-Kamiokande (KT), M_{fid} is the fiducial mass of each detector, ϕ

is the ν_μ flux at each detector, σ is the ν_μ cross-section and E_ν is the energy of ν_μ, respectively. In this thesis, the fiducial mass of Super-Kamiokande (KT) is 22.5 kt (25 t).

The parameters used to obtain the expected number of events and resultant expected number of events are summarized in Table 7.1 for each month. In total, we expect to observe 37.8 events induced by ν_μ interactions at Super-Kamiokande.

	Jun.99	Nov.99	Jan.00	Feb.00	Mar.00	May.00	Jun.00	Total
POT_{KT} ($\times 10^{18}$)	2.60	2.62	1.81	3.74	3.35	2.42	3.16	19.70
POT_{SK} ($\times 10^{18}$)	3.10	3.57	2.22	4.04	3.71	2.56	3.75	22.95
N_{KT}^{ν} ($\times 10^{3}$)	7.150	8.286	6.052	11.985	10.501	7.510	10.020	
$\eta_{\mathrm{SK}}/\eta_{\mathrm{KT}}$ ($\times 10^{-4}$)	6.81	6.71	6.71	6.71	6.71	6.71	6.71	
N_{SK}^{ν}	5.809	7.584	4.971	8.700	7.860	5.999	7.984	48.91
ϵ_{SK}	0.781	0.785	0.785	0.785	0.785	0.785	0.785	
N_{SK}	4.537	5.954	3.902	6.830	6.170	4.173	6.267	37.83

Table 7.1: Table of the parameters employed in the ν_μ event rate calculation each month and the resultant expected number of ν_μ events at Super-Kamiokande.

7.2 Systematic errors in number of ν_μ events

The systematic errors in the expected number of ν_μ induced events to be observed in Super-Kamiokande are summarized in Table 7.2.

Source	Jun.99	Nov.99	Jan.00	Feb.00	Mar.00	May.00	Jun.00	total
N_{KT}^{ν}	$+6.0\%$ -6.6%	$\pm 5.7\%$	$+5.6\%$ -5.5%	$+5.6\%$ -5.5%	$+5.6\%$ -5.5%	$\pm 5.7\%$	$\pm 5.7\%$	
POT normalization	1.0%	1.9%	1.1%	0.4%	0.7%	0.3%	1.0%	
$\eta_{\mathrm{SK}}/\eta_{\mathrm{KT}}$	$+13.6\%$ -9.9%	$+5.6\%$ -7.3%	$\rightarrow$	$\rightarrow$	$\rightarrow$	$\rightarrow$	$\rightarrow$	
ϵ_{SK}	3%	$\rightarrow$	$\rightarrow$	$\rightarrow$	$\rightarrow$	$\rightarrow$	$\rightarrow$	
NC/CC	$+0.6\%$ -0.8%	$\rightarrow$	$\rightarrow$	$\rightarrow$	$\rightarrow$	$\rightarrow$	$\rightarrow$	
Total	$+15.2\%$ -12.4%	$+9.4\%$ -10.5%	$+8.5\%$ -5.5%	$+5.6\%$ -5.5%	$+5.6\%$ -5.5%	$+6.8\%$ -6.6%	$+6.8\%$ -6.6%	$+3.67$ -3.90
δN_{SK}	$+0.690$ -0.560	$+0.562$ -0.625	$+0.334$ -0.379	$+0.581$ -0.660	$+0.526$ -0.597	$+0.390$ -0.431	$+0.588$ -0.650	

Table 7.2: Systematic errors in the expected number of ν_μ induced events in Super-Kamiokande.

Each item is explained one by one below.

Systematic error from KT measurement

The systematic error in the measurement of number of ν_μ interactions by KT ($N_{\mathrm{KT}}^{\nu_\mu}$) has been already listed in Table 5.3. The items (A) to (H) in the table except for the error from the NC/CC ratio are considered in $N_{\mathrm{KT}}^{\nu_\mu}$.

Systematic error of POT normalization

We apply the monthly average event rate for the correction of the monthly dead time of the KT detector. The stability of the event rate in a month is monitored by the KT detector as already shown in Fig. 5.5. The fluctuation of the event rate is measured monthly. The error in POT normalization is estimated by (root mean square of event rate in KT)×(dead time) for each month.

Uncertainty in the Near-to-Far flux ratio

The KT measurement is extrapolated to the number of ν_μ interactions in Super-Kamiokande using the Near-to-Far ratio of the number of ν_μ interactions (η_{SK}/η_{KT}). The systematic error in this ratio is estimated using the systematic error in the Near-to-Far flux ratio predicted by the PIMON measurement[100]. The MC-predicted number of events in each energy bin multiplied by one sigma error of the flux ratio is linearly summed up for the error in total number of events. The error in the observed total number of events is estimated to be $^{+13.6\%}_{-9.9\%}$ for June 1999 data and $^{+5.6\%}_{-7.3\%}$ for data since Nov. 1999.

Systematic error in SK efficiency

- The observed events in Super-Kamiokande are required to originate in the 22.5kt fiducial volume. To reconstruct the event vertices of the particles, we have two different vertex position fitters. One is called "TDC-fit" which is based on the arrival time of Cherenkov light photons and is commonly used in both Super-Kamiokande and KT. Another fitter is applied to single ring events in Super-Kamiokande after particle identification and momentum reconstruction. These fitters reconstruct the vertices of the particles by means of different ways and the number of events reconstructed in the fiducial volume differs by 2% from each other. we assign this difference as the systematic error in the fiducial volume of SK.

- The number of selected MC events in the fiducial volume is 11010, while 13938 events are generated in fiducial volume. The statistical error of MC is about 1%.

- To select ν_μ induced events in Super-Kamiokande, we apply several selection criteria like energy cut, outer detector cut and so on. Even if we change the selection criteria by a reasonable amount, the number of events to be observed change by less than 1%.

- In total, eventually we assign 3% as the systematic error in the SK detection efficiency.

NC/CC ratio

The uncertainty in the NC/CC cross section ratio is expected to cancel out when we compare the event rates between in KT and in Super-Kamiokande. The residual uncertainty after taking the ratio is less than 1% as shown in Table 7.3.

Source		$\epsilon_{KT}^{\nu_\mu}$	$\epsilon_{SK}^{\nu_\mu}$	N_{SK}
NC/CC	+30%	−4.2%	−3.6%	+0.6%
	−30%	+5.1%	+4.3%	−0.8%

Table 7.3: Correlated systematic error from the uncertainty in the ratio of NC/CC cross section. $\epsilon_{KT}^{\nu_\mu}$ and $\epsilon_{SK}^{\nu_\mu}$ are the detection efficiencies for ν_μ induced events in KT and Super-Kamiokande, respectively. N_{SK} is the expected number of events to be observed in Super-Kamiokande.

7.3 Expected number of electron candidates in Super-Kamiokande

In this thesis, a ν_e signal oscillating from ν_μ is searched for by counting an electron candidate in Super-Kamiokande. An electron candidate is defined by a single-ring e-like fully-contained (FC) event which is regarded as an electro magnetic shower induced by an electron. One source of the background against the oscillation search is the mis-identification of ν_μ-induced muons or pions.

The expected number of electron candidates induced by ν_μ is calculated by the following formula:

$$N_{SK}^{BG\nu_\mu} = \epsilon_{SK}^{BG\nu_\mu} \times N_{SK}^{\nu_\mu} , \qquad (7.4)$$

where $\epsilon_{SK}^{BG\nu_\mu}$ is the survival efficiency for ν_μ interactions to be mis-identified as an electron candidate in Super-Kamiokande and $N_{SK}^{\nu_\mu}$ is the number of ν_μ interactions estimated to be 48.91 in the previous section. The total survival efficiency for ν_μ is estimated to be 3.5% from MC study. The total number of ν_μ induced single-ring e-like FC events is calculated to be 1.71 events.

Another source of background is electron neutrinos produced by muon decays in the decay pipe and kaon decays near the target, which are called "beam ν_e". They are expected to contaminate in our neutrino beam by 1% level. The ν_e energy spectrum at Super-Kamiokande is predicted by the beam simulation as shown in Fig. 7.1.

The expected number of electron candidates caused by the beam ν_e ($N_{SK}^{BG\nu_e}$) is calculated by the following formula:

$$N_{SK}^{BG\nu_e} = \epsilon_{SK}^{BG\nu_e} \times R^{\nu_e} \times N_{SK}^{\nu_\mu} , \qquad (7.5)$$

where $\epsilon_{SK}^{BG\nu_e}$ is the efficiency for beam ν_e as an electron candidate in Super-Kamiokande, R^{ν_e} is the ratio of the number of ν_e interactions to that of ν_μ and $N_{SK}^{\nu_\mu}$ is the number of ν_μ interactions used in Eq.7.3.

Figure 7.1 shows the efficiency as a function of ν_e energy. The efficiency of the beam ν_e is 87.2% for CC quasi-elastic interactions by ν_e, 42.5% for CC inelastic interactions and 9.2% for NC interactions. The overall efficiency is 45.0%. The beam simulation predicts the ratio R^{ν_e} to be 0.947% at Super-Kamiokande. Under this assumption, the number of electron candidates in Super-Kamiokande induced by the beam ν_e is expected to be 0.208 events/2.29×10^{19}.

To summarize this section, the expected number of beam-induced $\nu_\mu + \nu_e$ background electron candidate events against ν_e appearance search is expected to be:

$$N_{SK}^{BG\nu_\mu} + N_{SK}^{BG\nu_e} = 1.71 + 0.208 = 1.92 \, \text{events}/2.29 \times 10^{19} \text{POT} .$$
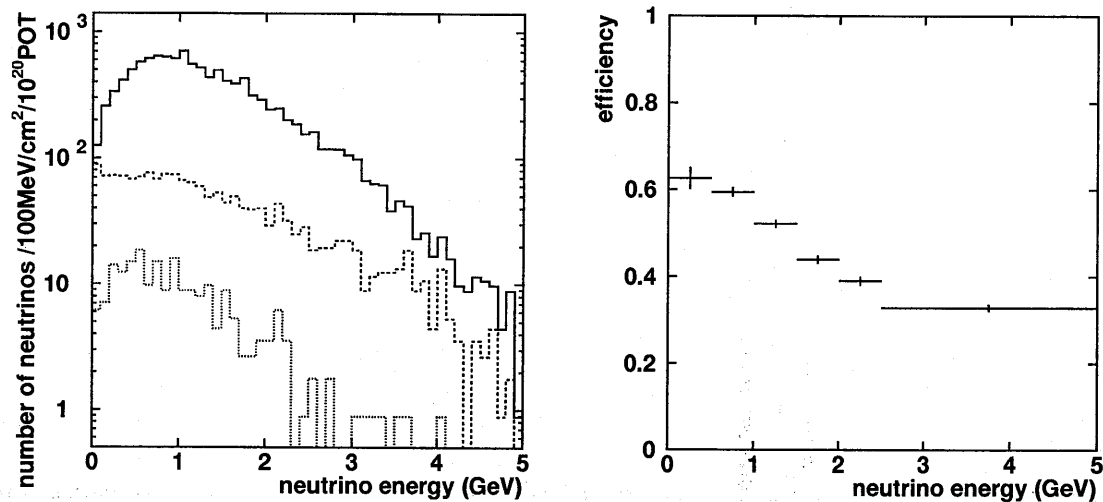
Figure 7.1: (Left) ν_e energy spectrum predicted by the beam simulation. Solid histograms show all the flux and dashed(dotted) histogram shows the component from $K^{\pm}e3(K^0e3)$ decay. (Right) Efficiency curve for the beam ν_e as a function of neutrino energy (GeV).

7.4   Systematic Errors in the Electron Candidates

7.4.1   Systematic errors in ν_μ-induced electron candidates

The systematic errors in the number of ν_μ induced background events against ν_e appearance search is estimated and summarized in Table 7.4.

The total systematic error is $^{+47.2\%}_{-47.6\%}$, while details are described below.

- $N^\nu_{\rm SK}$,POT normalization
  These terms are the same as those in Section 7.2.

- $\eta_{\rm SK}/\eta_{\rm KT}$
  The error of the extrapolation from KT to Super-Kamiokande is estimated for the ν_μ induced electron candidates. The calculation method is the same as in Section 7.2. The estimated error in the total number of events to be observed is $^{+14.4\%}_{-10.5\%}$ for June 1999 data and $^{+5.6\%}_{-7.6\%}$ for data since Nov. 1999.

- $\epsilon^{BG\nu_\mu}_{\rm SK}$
  The number of selected MC events in the fiducial volume is about 500 events. We assign 5% as the systematic error from MC statistics.

We set an energy threshold at 100MeV in the electron selection. When the energy scale changes by 10%, the number of selected events changes by about 1%. Also the uncertainty

Source	Jun.99	Nov.99	Jan.00	Feb.00	Mar.00	May.00	Jun.00	total
N_{KT}^ν	+6.0% −6.6%	±5.7%	+5.6% −5.5%	+5.6% −5.5%	+5.6% −5.5%	±5.7%	±5.7%	
POT normalization	1.0%	1.9%	1.1%	0.4%	0.7%	0.3%	1.0%	
η_{SK}/η_{KT}	+14.4% −10.5%	+5.6% −7.6%	→	→	→	→	→	
$\epsilon_{SK}^{BG\nu_\mu}$	6%	→	→	→	→	→	→	
NC/CC	+4.6% −7.3%	→	→	→	→	→	→	
CC single-π	+4.5% −3.8%	→	→	→	→	→	→	
CC multi-π	±0.4%	→	→	→	→	→	→	
Ring Counting	6%	→	→	→	→	→	→	
PID	±45%	→	→	→	→	→	→	
Total	+48.8% −48.2%	+47.0% −47.5%	+46.9% −47.5%	+46.9% −47.5%	+46.9% −47.5%	+46.9% −47.5%	+46.9% −47.5%	+47.2% −47.6%

Table 7.4: Systematic errors in the expected number of ν_μ induced electron candidates in Super-Kamiokande.

in the fiducial volume is considered to affect $\epsilon_{SK}^{BG\nu_\mu}$ by 2% as is described in Section 7.1. In total, 6% is assigned to the systematic error from the SK detection efficiency except for the ring counting and particle identification which is separately described below.

- Ring Counting
  Only the events with single Cherenkov ring are selected for an electron candidate in Super-Kamiokande. The number of rings in an event is obtained automatically by the ring-counting program. In order to estimate the systematic uncertainty in the ring-counting program, the standard result is compared with that from a different ring-counting program and also with that from eye-scan by physicists. The difference is estimated to be 6%.

- Particle Identification (PID)
  The capability of the particle identification with a water Cherenkov detector, which is a miniature of the Super-Kamiokande detector, was investigated in the KEK-PS E261a experiment[101] using muon beam generated by the accelerator. In the E261a experiment, less than 3% of muons with larger than 250 MeV/c momentum is identified as an electron. We expect that the Super-Kamiokande detector has better ability to identify particle types than the detector in the E261a experiment because the photo-cathode coverage of inner wall of Super-Kamiokande detector is about twice as that of the detector used in the E261a experiment.

  From Monte-Carlo study, Gamma-rays from neutral pion decay induced by ν_μ interactions can make single-ring e-like FC events. The number of single-ring e-like events which contain no neutral pions is 0.30 events while all single-ring events without neutral pions is 20.0 events as shown in Table 7.5. The mis-identification probability is calculated to be 1.5%. Suppose that the mis-identification probability is 3%, the number of ν_μ induced electron candidates increases by 17%. And it decrease by 17% if the contribution from

interaction mode	single-ring	single-ring e-like
CC quasi-elastic	10.84 (0.01)	0.13 (0.00)
CC single-π	6.98 (0.34)	0.25 (0.16)
CC multi-π	1.87 (0.44)	0.25 (0.21)
CC others	0.09 (0.04)	0.01 (0.01)
NC	1.56 (1.07)	1.06 (1.03)
Total	21.33 (1.90)	1.71 (1.42)

Table 7.5: Number of ν_μ induced single-ring events predicted by Monte-Carlo simulation for each interaction mode. The number of events which contain one or more neutral pions is shown in the parenthesis.

Source		$\delta\epsilon_{KT}$	$\delta\epsilon_{SK}^{BG\nu_\mu}$	$\delta N_{SK}^{BG\nu_\mu}$
NC/CC	+30%	−4.2%	−11.5%	−7.3%
	−30%	+5.1%	+9.7%	+4.6%

Table 7.6: Correlated systematic error from the uncertainty in the NC/CC cross section ratio.

those events are neglected,

The other hand, The single-ring events by neutral pions should be taken as electron candidates. However 1/4 of such events are identified as muons due to accompanying muons and charged pions. Conservatively we assign this fraction as the systematic error, ±0.48 events.

Consequently we assign ±0.77 events (±45% of 1.71 events) for the systematic error from the uncertainty in the particle identification.

- NC/CC
  This term is expected to largely cancel out if we take the SK/KT event ratio. The residual uncertainty after the cancellation is less than $^{+4.6\%}_{-7.3}$% as shown in Table 7.6.

- CC single-π, CC multi-π
  The efficiency for CC inelastic interactions in the electron selection by Super-Kamiokande is quite different from that in the neutrino rate measurement by KT, because we require that only one Cherenkov ring exists in an event to select the electron. The detection efficiency is 3.2% for CC single pion production process and 1.8% for CC multi pion production process. Therefore, we consider the systematic error from the uncertainty in inelastic cross section not to cancel out if we take the SK/KT event ratio. The errors are estimated to be 3% to 5% from 30% uncertainty.

7.4.2 Systematic errors in ν_e-induced electron candidates

The systematic error in the number of electron candidates in Super-Kamiokande induced by the beam ν_e. The main source is the uncertainty in the ν_e/ν_μ interaction ratio at Super-

Source	Error
fiducial volume	2%
MC stat.	2%
energy threshold	$\ll 1\%$
cross section	$+7\%$ -8%
ring counting	6%
PID	0.4%
$N_{SK}^{\nu_\mu}$	$+9\%$ -10%
$R_{SK}^{\nu_e}$	$+34\%$ -22%
ν_e energy spectrum	$+16\%$ -12%
kaon production	14%
Total	$+42\%$ -32%

Table 7.7: Systematic errors in the expected number of ν_e induced electron candidates in Super-Kamiokande.

Source	Jun.99	Nov.99	Jan.00	Feb.00	Mar.00	May.00	Jun.00	total
$N_{\mathrm{KT}}^{\nu_\mu}$	$+6.0\%$ -6.6%	$\pm 5.7\%$	$+5.6\%$ -5.5%	$+5.6\%$ -5.5%	$+5.6\%$ -5.5%	$\pm 5.7\%$	$\pm 5.7\%$	
POT normalization	1.0%	1.9%	1.1%	0.4%	0.7%	0.3%	1.0%	
$\eta_{\mathrm{SK}}/\eta_{\mathrm{KT}}$	$+13.4\%$ -9.7%	$+5.7\%$ -7.2%	$\rightarrow$	$\rightarrow$	$\rightarrow$	$\rightarrow$	$\rightarrow$	
Total	$+14.7\%$ -11.8%	$+8.3\%$ -9.4%	$+8.1\%$ -9.1%	$+8.0\%$ -9.1%	$+8.0\%$ -9.1%	$+8.1\%$ -9.2%	$+8.1\%$ -9.2%	$+8.88\%$ -9.49%

Table 7.8: Systematic errors in the number of ν_μ interactions ($N_{SK}^{\nu_\mu}$) in Super-Kamiokande for each month. The number of ν_e interactions is calculated by multiplying efficiency and ν_e/ν_μ interaction ratio on $N_{SK}^{\nu_\mu}$.

Kamiokande and the total systematic error is estimated to be $+42\%_{-32\%}$ as listed in Table 7.7. Each item in the table is explained below.

- $N_{SK}^{\nu_\mu}$

  The number of ν_e interactions is calculated from the number of ν_μ interactions extrapolated from the measurement by KT. The error in the extrapolation is estimated in the same way described in Section 7.2 . As shown in Table 7.8, the systematic error is estimated to be $+9\%_{-10\%}$.

- $R_{SK}^{\nu_e}$

  The ν_e/ν_μ interaction ratio is estimated by the beam simulation using the pion production model as shown in Eq. 3.1. When the parameters in Eq. 3.1 change within their 90% C.L. limits, the ν_e/ν_μ interaction ratio changes between 0.74% and 1.26%. Thus, $+34\%_{-22\%}$ is assigned to the systematic error.

- ν_e energy spectrum
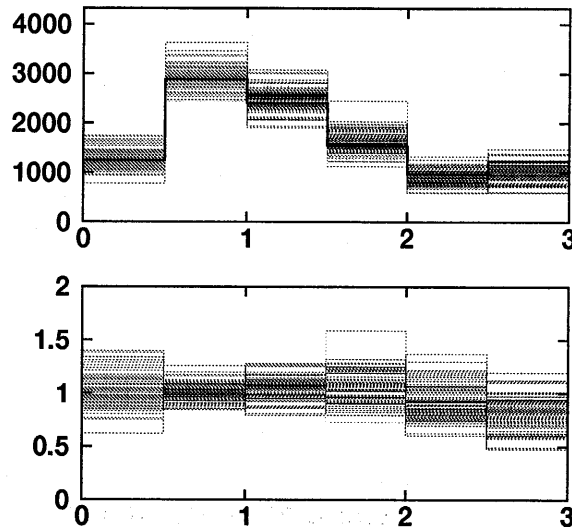
Figure 7.2: The beam ν_e energy spectra assuming various reasonable input parameters in the pion production model (Eq. 3.1). The upper figure shows the energy spectrum and the lower shows the ratio of them to that with the standard parameter set in each energy bin in our beam simulation.

The uncertainty in the ν_e energy spectrum is estimated by the same method as in the previous item, $R^{\nu_e}_{SK}$. Figure 7.2 shows the ν_e energy spectra assuming various reasonable input parameters in the pion production model. The number of ν_e induced electron candidates has the uncertainty of $^{+16\%}_{-12\%}$, when we employ the full spread in each energy bin as its 1σ standard bin-by-bin error.

- Kaon production

  Another source of the beam ν_e is kaons produced at the target. The parameters in Eq. 3.1 for the kaon production in our beam simulation is derived from Ref. [67]. Figure 7.3 shows the kaon contribution in the selected MC events as a function of ν_e energy. The beam ν_e from kaons is expected to induce 14% of selected electron candidates. We assign this contribution of kaons to the systematic error.

- fiducial volume, MC statistics, energy threshold

  We select the events with their vertex position reconstructed in the fiducial volume at an energy threshold of 100MeV. The systematic error in the number of events coming from the fiducial volume cut is 2% as described in Section 7.2 and the error from the energy cut is estimated to be negligible by the Monte-Carlo study. The statistical error of the generated ν_e MC events is 2%.

- cross sections

  The systematic error arising from the uncertainty in the neutrino-nucleus cross section is estimated for each interaction mode. When we change the cross section for NC, CC single-π production and CC multi-π production by 30%, the number of selected events
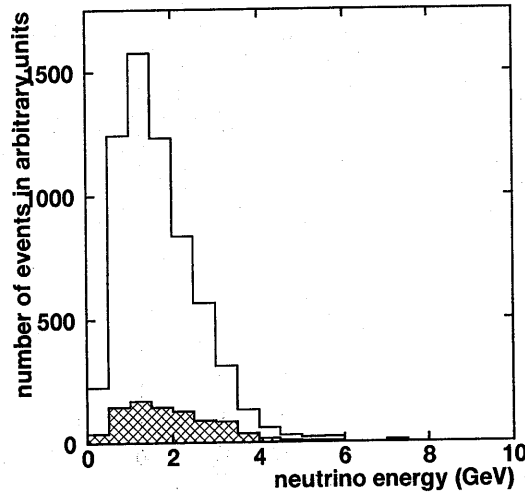
Figure 7.3: The kaon contribution in the selected MC events induced by ν_e as a function of ν_e energy. Blank histogram corresponds to the selected MC events induced by ν_e from pion decays and shaded histogram corresponds to that from kaon decays.

changes $^{+6.6\%}_{-5.7\%}$, $^{+2.1\%}_{-2.5\%}$ and $^{+3.0\%}_{-2.6\%}$, respectively. We assign $^{+7\%}_{-8\%}$ to the systematic error coming from the uncertainty in the cross sections.

- ring counting
  This term has been already explained in Section 7.4.1.

- particle identification (PID)
  The systematic error caused by PID is estimated by the mis-identification of charged current quasi-elastic events induced by ν_e interaction which passed all selection criteria except for PID. Figure 7.4 shows the distribution of particle ID parameter for ν_e induced events. The misidentification probability is estimated to be 0.4% for CC quasi-elastic events.

7.5 Summary for the Expected Number of Events at Super-Kamiokande

As a result of detailed discussions, the expected numbers of neutrino-beam-induced background electron candidates are summarized in the followings:

$$N_{\text{SK}}^{\text{BG}\nu_\mu} = 1.71^{+0.807}_{-0.814}\text{events,} \tag{7.6}$$

$$N_{\text{SK}}^{\text{BG}\nu_e} = 0.208^{+0.087}_{-0.067}\text{events.} \tag{7.7}$$
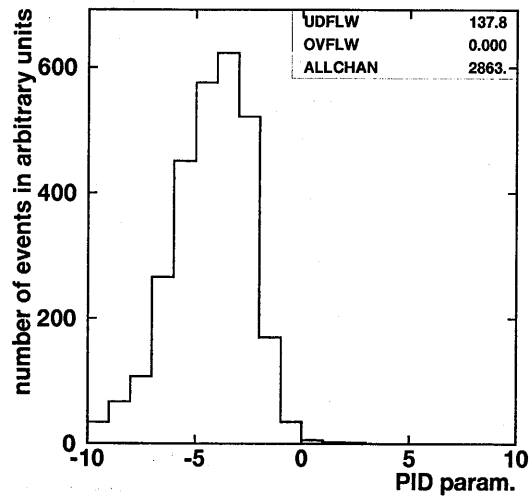
Figure 7.4: Particle ID parameter for fully-contained 1-ring MC events induced by the beam ν_e CC quasi-elastic interactions. The negative (positive) value of the parameter corresponding to showering (non-showering) particle type. Misidentification probability is 0.5% for this sample.

When the systematic errors are linearly added, the expected number of electron candidates which are observed as the background against the ν_e appearance search is calculated to be:

$$N_{\text{SK}}^{\text{BG}\nu_\mu} + N_{\text{SK}}^{\text{BG}\nu_e} = 1.92^{+0.89}_{-0.88}(\text{syst.})\ \text{events} .$$

— 7.3 7.4

Chapter 8

Results

8.1 Comparison between the observation and the expectation

As a result of the ν_e event search at Super-Kamiokande, we found one single-ring e-like FC event, while the expectation is $1.92^{+0.89}_{-0.88}$ events.

If neutrino oscillations occur with an adequately large mixing angle, we will observe an excess of ν_e signal against background events coming from ν_μ and beam ν_e contaminations. However, there found to be no excess in our electron sample. Thus we conclude that there is no evidence for $\nu_\mu \to \nu_e$ oscillations. The 90% C.L. upper limit of the signal excess is 2.7 events, where the expected number of events is assumed to follow the Poisson distribution of which mean is smeared by the Gaussian distribution with variance $\sigma = 0.89$.

The excluded region will be set in the following section assuming the neutrino oscillation hypothesis in the $\nu_\mu \to \nu_e$ mode.

8.2 Neutrino Oscillation Analysis

The possibility of the 3-flavor mixing neutrino oscillations with one mass scale dominance is discussed in this section. The probability for a muon neutrino of energy E_ν to oscillate to an electron neutrino is given by:

$$P(\nu_\mu \to \nu_e) = \sin^2 2\theta_{\mu e} \sin^2 \left(1.27 \frac{\Delta m^2 L}{E_\nu} \right) \tag{8.1}$$

Using average neutrino energy $\langle E_\nu \rangle \simeq 1.3\text{GeV}$ and flight length $L = 250\text{km}$, the most sensitive Δm^2 is expected to be:

$$\frac{\pi/2}{1.27L/\langle E_\nu \rangle} = 7 \times 10^{-3} eV^2 . \tag{8.2}$$

To test the ν_e appearance, we reconstruct a ν_e energy E^{rec} from the momentum and the direction of the selected event assuming a quasi-elastic interaction and mapped them into 6 bins. The range of E^{rec} is from 0 to 2.5 GeV for the first 5 bins. The events larger than 2.5 GeV are mapped in the last bin.

To determine the expected number of background events induced by ν_μ and beam ν_e after oscillation, we assume $\sin^2 2\theta_{23} = 1$, which means that muon neutrinos oscillate only to tau neutrinos with $sin^2 2\theta_{\mu\tau} = 1$ when $\theta_{13} \ll 1$. According to Eq. 1.19 and Eq. 1.20, the mixing parameters under this assumption are as follows:

$$\sin^2 2\theta_{\mu e} = \frac{1}{2}\sin^2 2\theta_{13} \quad \sin^2 2\theta_{\mu\mu} = 1 - \sin^4 \theta_{13}$$

$$\sin^2 2\theta_{ee} = \sin^2 2\theta_{13},$$

The oscillation probability for ν_μ and beam ν_e and possible appearing ν_e via neutrino oscillations is calculated according to Eq. 1.16 and Eq. 1.16 with these mixing parameters.

The neutrino oscillation hypothesis is examined in the parameter region of $0 < \sin^2 2\theta_{13} < 1.0$ and $10^{-4} < \Delta m^2 < 10^{-1}$ by the following procedures:

- Calculate the number of single-ring e-like FC events expected to be observed assuming the oscillations

  The ν_e flux from neutrino oscillations is calculated by multiplying the ν_μ flux, which is derived in Chapter 7 with no oscillation hypothesis, by $P(\nu_\mu \to \nu_e)$ as a function of neutrino energy. The systematic error in the absolute normalization is estimated to be 10% as listed in the 7th row of Table 7.7.

  To estimate the number of background events from ν_μ and beam ν_e, the number of charged current interactions in the MC sample normalized to the prediction by the KT measurement described in Chapter 7 is decreased by multiplying the oscillation probability according to Eq. 8.3. The number of neutral current interactions are preserved because the total number of neutrinos interacting via them is conserved, even if neutrino oscillations occur. The same errors as in the case of no oscillation case excluding the absolute normalization error are assigned to these background events, i.e. ±47% for ν_μ and ±41% for beam ν_e.

- Calculate χ^2

  The following χ^2 is defined to draw contours of excluded regions:

$$\chi^2 = \min_{\alpha,\beta,\gamma}\left\{ L(\alpha,\beta,\gamma) + \frac{\alpha^2}{\sigma_\alpha^2} + \frac{\beta^2}{\sigma_\beta^2} + \frac{\gamma^2}{\sigma_\gamma^2}\right\} \tag{8.3}$$

$$L(\alpha,\beta,\gamma) = -2\sum_{i=1}^{6}\left(\frac{(X_i)^{N_i}\exp{(-X_i)}}{N_i!}\right) \tag{8.4}$$

$$X_i = (1+\alpha)M_i(signal)$$
$$+(1+\alpha)(1+\beta)M_i(BG\ \nu_\mu) + (1+\alpha)(1+\gamma)M_i(BG\ \nu_e), \tag{8.5}$$

where N_i is the observed number of events (1 event at 612MeV in this thesis) in the i-th energy bin, $M_i(signal, mbox BG\ \nu_\mu, BG\ \nu_e)$ is the expectation of ν_e appearance signal or mis-identified ν_μ or beam ν_e contamination after the oscillations, α is a factor relevant to the absolute normalization with its error $\sigma_\alpha = 10\%$, β to the $\nu_\mu \to$ e-like mis-identification

probability with its error $\sigma_\beta = 47\%$, γ to the fraction of beam ν_e contamination with its error $\sigma_\gamma = 41\%$.

- If the χ^2 difference from its minimum in the $(\sin^2(2\theta_{13}), \Delta m^2)$ plane exceeds 4.61, we reject the set of assumed oscillation parameters at the 90% C.L..

Figure 8.1 shows the results from the oscillation analysis. The region of the parameter space $(\Delta m^2, \sin^2 2\theta_{13})$ to the right side of the curve is excluded at 90% C.L. by this measurement. From Fig. 8.1, the region $\sin^2 2\theta_{13} \gtrsim 0.7$ and $\Delta m^2 \gtrsim 3 \times 10^{-3}$ is excluded at 90% C.L. which is consistent with the CHOOZ result as already shown in Fig.1.2. The region $3 \times 10^{-3} \lesssim \Delta m^2 \lesssim 10^{-2} \mathrm{eV}^2$ is a newly excluded result by ν_e appearance experiments using artificial ν_μ beam in the world.

Figure 8.1: The 90% C.L. upper limit on $\nu_\mu \to \nu_e$ oscillations assuming one mass scale dominance and $\sin^2 2\theta_{23} = 1$. The excluded is the area to the right side of the curve.

This experiment continues and is expected to accumulate a total of 10^{20} protons on the target (POT) in 4 years (2.29×10^{19}POT in this thesis). Figure 8.2 shows the expected sensi-

tivity that will be obtained with the designed statistics for $\nu_\mu \rightarrow \nu_e$ oscillations. The excluded region will extend to $\sin^2 2\theta_{13} = 0.2$ at $\Delta m^2 = 7 \times 10^{-3}$ with systematic errors estimated in this thesis.

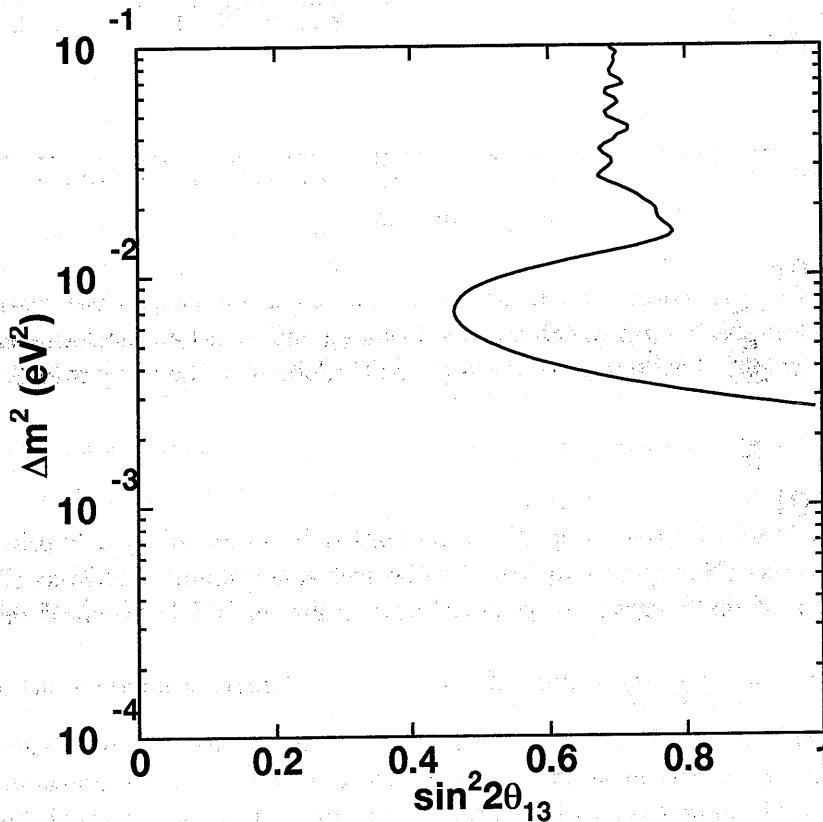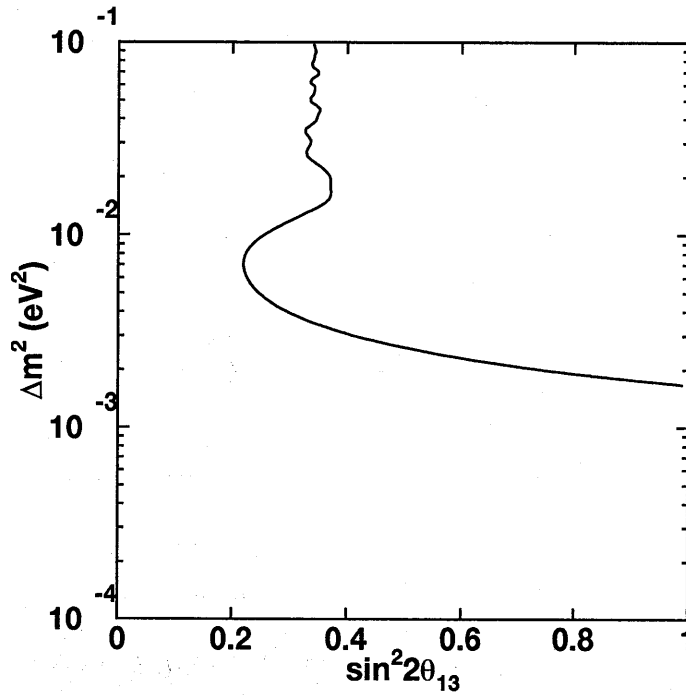Figure 8.2: The 90% C.L. designed sensitivity of this experiment (10^{20}POT in 4 years) for $\nu_\mu \rightarrow \nu_e$ oscillations assuming one mass scale dominance and $\sin^2 2\theta_{23} = 1$. The excluded region of $\sin^2 2\theta_{13}$ and Δm^2 is to the right side to the curve.

Chapter 9

Conclusion

The KEK-Kamioka (K2K) long baseline ν_μ beam experiment has successfully taken data both at KEK and at Kamioka to search for neutrino oscillations for the period from June 1999 to June 2000, during which 2.29×10^{19} protons were delivered on the target to generate neutrinos.

When we assume 3-flavor neutrino oscillations with one mass scale dominance, the electron neutrinos are expected to appear against the background events from ν_μ mis-identification and ν_e contamination to our beam.

First of all, we measured the ν_e/ν_μ interaction ratio to be $1.76 \pm 0.62(\text{stat.})^{+0.76}_{-1.00}(\text{sys.})(\%)$ at the KEK site. Thus, it is confirmed that the amount of ν_e contamination in our ν_μ beam is as small as the prediction by our beam simulation, 1.3%.

We searched for ν_e appearance at Super-Kamiokande by detecting single-ring e-like fully-contained events, and found 1 such event.

We estimated the number of background electron events to be observed in Super-Kamiokande by extrapolating the neutrino interaction rate in the 1 kilo-ton water Cherenkov detector at the KEK site. As a result, the expected number of single-ring e-like FC events in Super-Kamiokande is calculated to be $1.92^{+0.89}_{-0.88}(\text{sys.})$ events from ν_μ mis-identification and beam ν_e contamination, which is consistent with the observed number, 1 event.

Therefore, we conclude that no evidence for $\nu_\mu \to \nu_e$ oscillations is found in this analysis. The following parameter region assuming $\nu_\mu \to \nu_e$ oscillations is excluded at 90% confidence level: $\sin^2 2\theta_{13} \gtrsim 0.7$ and $\Delta m^2 \gtrsim 3 \times 10^{-3}$. This is the first experimental limit in the world on $\nu_\mu \to \nu_e$ appearance oscillation sensitive to $\Delta m^2 \sim 3 \times 10^{-3} \text{eV}^2$.

Appendix A

Vertex Reconstruction in the Water Cherenkov Detector (TDC-fit)

The vertex reconstruction method named "TDC-fit" is used in common for KT and Super-Kamiokande. There are two step in vertex fitting, one is a rough fitting without the Cherenkov edge information (PFIT), another is a more precise fitting using the edge (TDC-fit).

We use the time information called time residual (t_i), which is calculated by subtracting photon time-of-flight (TOF) from the photon arrival time to the i-th PMT, as follows:

$$t_i = t_i^0 - \frac{1}{c(Q_i, l_i)} \times \sqrt{(x - x_i)^2 + (y - y_i)^2 + (z - z_i)^2}$$

$$
\begin{array}{ll}
t_i^0 & \text{hit time of the i-th PMT} \\
(x, y, z) & \text{vertex position} \\
(x_i, y_i, z_i) & \text{position of the i-th PMT} \\
c(Q_i, l_i) & \text{light velocity in water}
\end{array}
$$

The time residual is expected to have a common value in all PMTs for the real vertex if the Cherenkov photons are emitted by an infinitesimally short track particle, but in fact, it is not. Also some of the photons are scattered in the water. Nevertheless the distribution of the time residual becomes sharp near the real vertex. In order to quantify its sharpness, we define the goodness as a estimator of the vertex fitting as follows: In case of PFIT:

$$G_P = \frac{1}{N_{hit}} \sum_i \exp\left(-\frac{(t_i - \langle t \rangle)^2}{2(1.5\sigma)^2}\right)$$

and in case of TDC-fit:

$$G = \begin{cases} \dfrac{\sum_i \frac{1}{\sigma^2} \exp\left(-\frac{(t_i - \langle t \rangle)^2}{2(1.5\sigma)^2}\right)}{\sum_i \frac{1}{\sigma^2}} & \text{(inside Cherenkov cone)} \\[4ex] \dfrac{\sum_i \frac{1}{\sigma^2} \text{Max}\left[\exp\left(-\frac{(t_i - \langle t \rangle)^2}{2(1.5\sigma)^2}\right), 0.8 \exp\left(-\frac{t_i - \langle t \rangle}{20 nsec}\right)\right]}{\sum_i \frac{1}{\sigma^2}} & \text{(outside Cherenkov cone)} \end{cases}$$

126

where σ is the mean value of PMT timing resolution, $\rangle t\langle$ is the mean of t_i. The goodness takes the value from 0 to 1 and the higher value is estimated to be better. The track length of charged particle and time delay of the scattered light are also taken into account in the calculation of goodness of TDC-fit. TDC-fit finds the vertex where the goodness becomes maximum.

In order to find out the particle direction, TDC-fit picks up the outer edge of the Cherenkov cone from the observed charge image.

The Cherenkov edge is obtained from the charge distribution as a function of the Cherenkov opening angle (PE(θ)). The Cherenkov edge (θ_{edge}) is determined so as to be outside but nearest the peak of PE(θ) distribution (θ_{peak}) with $d^2PE/d\theta^2$ 0. Under these conditions, the direction is searched so as to maximize the following evaluation function:

$$f = \frac{\int_0^{\theta_{edge}} PE(\theta)d\theta}{\sin\theta_{edge}} \cdot \left(\frac{dPE(\theta)}{d\theta}\right)^2 \cdot \exp\left\{-\frac{(\theta_{edge} - \theta_C)^2}{\sigma_\theta^2}\right\}$$

where θ_C and σ_θ are the Cherenkov opening angle and its resolution, respectively.

Bibliography

[1] S.L. Glashow, Nucl. Phys. **22**, 579 (1961).

[2] S. Weinberg, Phys. Rev. Lett. **19**, 1264 (1961).

[3] A. Salam, "Elementary particle physics", Nobel Symp. No.8

[4] T. Yanagida, Proc. of Workshop Unified theory and Baryonn Number in the Universe (KEK, Tsukuba, Japan), 1970; Prog. Theor. Phys., **B135** (1978) 66

[5] W.Pauli, *Open Letter to Radioactive Ladies and Gentlemen*, (1930) (translation into English) Physics Today **31**, 27 (1978)

[6] A.I. Belesev *et al.*, Phys. Lett. **B350**, 263 (1995)

[7] Particle Data Group, European phys. J. **C15**, 1 (2000)

[8] K. Assamagan *et al.*, Phys. Rev. **D53**, 6065 (1996)

[9] R.Barate *et al.*, European Phys. J. **C2**, 395 (1998)

[10] E. Majorana, Nuo. Cim. **5**, 171 (1931).

[11] L.Baudis *et al.*, Phys. Rev. Lett. **83**, 41 (1999)

[12] Z.Maki, M.Nakagawa and S.Sakata, Prog. Theor. Phys. **28**, 870 (1962)

[13] B.Pontecorvo, Sov. Phys. **JETP6**, 429 (1958); ibid., **7** 172 (1958)

[14] G.L.Fogli et al., Phys. Rev **D55** 4385 (1997)

[15] C.Giunti et al., hep-ph/9709439

[16] M.Kobayashi and T.Maskawa, Prog. Theor. Phys. **49**, 652 (1979)

[17] Y. Fukuda *et al.*, Phys. Lett. **B335**, 237 (1994).

[18] Talk given by Ed. Kerns at the XXXth International Conference on High Energy Physics, Osaka, Japan, July 27 - August 2, 2000, to appear in the proceedings.

[19] R.Becker-Szendy *et al.*, Phys. Rev. **D 46**, 3720 (1992).

[20] M.Aglietta *et al.*, Europhys. Lett. 8 (1989) 611.

[21] Ch.Berger *et al.*, Phys. Lett. B 227 (1989) 489;Ch.Berger *et al.*, Phys. Lett. B 245 (1990) 305.

[22] K.Daum *et al.*, Z. Phys. C 66 (1995) 417.

[23] W. W. M. Allison *et al.*, Phys. Lett. **B449**, 137 (1999).

[24] T. Kajita for the Super-Kamiokande Collaboration, Nucl. Phys. Proc. Suppl. **77**, 123 (1999) hep-ex/9810001.

[25] L. Borodovsky *et al.*, Phys. Rev. Lett. **68**, 274 (1992).

[26] M. Apollonio *et al.*, Phys. Lett. **B420** 397 (1998).

[27] G. Zacek *et al.*, Phys. Rev. **D34**, 2621 (1986).

[28] B. Achkar *et al.*, Nucl. Phys. **B434**, 503 (1995).

[29] [FERMILAB E531 Collaboration],
N. Ushida *et al.*, Phys. Rev. Lett. **57**, 2897 (1986),
G. N. Taylor *et al.*, Phys. Rev. **D28**, 2705 (1983),
E. B. Brucker *et al.*, Phys. Rev. **D34**, 2183 (1986).

[30] F. Dydak *et al.*, Phys. Lett. **B134**, 281 (1984).

[31] F. Bergsma *et al.*, Phys. Lett. **142**, 103 (1984).

[32] O. Sato [CHORUS Collaboration], Nucl. Phys. Proc. Suppl. **77**, 220 (1999).

[33] J.J. Gomez-Cadenas [NOMAD Collaboration], Nucl. Phys. Proc. Suppl. **77**, 225 (1999).

[34] C. Athanassopoulos *et al.*, Phys. Rev. **C54**, 2685 (1996); Phys. Rev. Lett. **77**, 3082 (1996); Phys. Rev. Lett. **81** 1774 (1998).

[35] The KARMEN Collaboration, B. Armbruster *et al.*, Proc. of the XXXIIIrd Rencontres de Moriond: '98 Electroweak Interactions and Uni,ed Theories, to be published in Editions Frontieres (1998), available from http://wwwik1.fzk.de=www=karmen; Phys. Rev. **C57**, 3414 (1998); K. Eitel and B. Zeitnitz, proceedings of the XVIIth International Conference on Neutrino Physics and Astrophysics, Takayama, Japan, June 1998 (hep-ex/9809007);

[36] K. Nishikawa *et al.*, "Proposal for a Long Baseline Neutrino Oscillation experiment, using KEK–PS and Super–Kamiokande" (1995).

[37] A. Jodido *et al.*, Phys. Rev. **D 34**, 1967 (1986).
G. Barenboim *et al.*, Phys. Rev. **D 55**, 4213 (1997).
G. Beall *et al.*, Phys. Rev. Lett. **48**, 848 (1982).
W.S. Hon and A. Soni, Phys. Rev. **D32**, 163 (1985).
J. Baseq *et al.*, Phys. Rev. **D32**, 175 (1985).
P. Colaugelo and G. Nardulli , Phys. Lett. **B253**, 154 (1991).

[38] L. Wolfenstein, Nucl. Phys. **B186**, 147 (1981)

[39] Development of Coordinate Tranformation Program TKY2WGS, GSI technical Report, B·1-No.23(1994)8.

[40] H. Noumi *et al.*, Nucl. Instrum. Meth. **A398**, 399 (1997).

[41] Rika Nenpyo (Chronological Scientific Table), ed. National Astronomical Observatory, Maruzen Co., Ltd., 1997, p629, (in Japanese)

[42] OHO-'96 (written in Japanese, KEK accelerator school(1996) text).

[43] M. Ieiri *et al.*, Given at 1st Asian Particle Accelerator Conference (APAC 98), Tsukuba, Japan, 23-27 Mar 1998.

[44] KEK-PS USERS GUIDE BOOK (1992), KEK Publication.

[45] K.L. Brown *et al.*, TRANSPORT, CERN 80-04

[46] K.L. Brown and Ch Iselin, DECAY TURTLE, CERN 74-02

[47] Y. Suzuki *et al.*, Proc. of Int. Conf. on Accelerator and Large Experimental Physics Control system, (1997) 266.

[48] M.Kohama, Master thesis "The study of magnetic horns for long base-line neutrino oscillation experiment." (in japanese, unpublished)

[49] Y. Yamanoi *et al.*, Proc. 15th Int. Conf. on Magnet Technology (1997).

[50] F. Sauli, CERN Report 77-09 (1977).

[51] K.H. Tanaka *et al.*, KEK preprint 91-27

[52] S.Nakayama, "The data aquisition system of front water Cherenkov detector in long-baseline neutrino oscillation experiment." (Master Thesis of Tokyo U., unpublished, in japanese)

[53] S. Kawabata *et al.*, Nucl. Instrum. Meth. **A270**, 11 (1988).

[54] Y. Ikegami *et al.*, IEEE Trans. Nucl. Sci. **36**, 665 (1989).

[55] KEK Data Aquisition Development Working Group, "TKO Specification",KEK Report 85-10 (1985).

[56] Y.Koshio, "Study of Solar Neutrinos at Super Kamiokande" (PhD Thesis of Tokyo U., unpublished)

[57] M.Shiozawa, "Search for Proton Decay $p \to e^+ \pi^0$ in a Large Water Cherenkov Detector" (PhD Thesis of Tokyo U., unpublished)

[58] H. Kume *et al.*, Nucl. Instr. and Meth., **205**, 299 (1983).

[59] A. Suzuki *et al.*, Nucl. Instr. and Meth., **A329**, 299 (1993).

[60] C.McGrew, PhD Thesis of U.C.Irvine, unpublished

[61] T.Tanimori *et al.*, IEEE Trans. Nucl. Sci. **NS-36**, 497 (1989).

[62] "PHOTOMULTIPLIER TUBE –principle to application–" HAMAMATSU PHOTON-ICS K.K.

[63] M. Nakahata *et al.* [KAMIOKANDE Collaboration], J. Phys. Soc. Jap. **55**, 3786 (1986).

[64] GEANT–Detector Description and Simulation Tool, Application Software Group, Computing and Networks Division (1993).

[65] A. Ferrari and P.R. Sala, "A new model for hadronic interactions at intermediate energies for the FLUKA code," *In *Tallahassee 1993, Monte Carlo simulation in high energy and nuclear physics* 277-288.*

[66] T.A. Gabriel, J.D. Amburgey and B.L. Bishop, "'Calor': A Monte Carlo Program Package For The Design And Analysis Of Calorimeter Systems," ORNL/TM-5619.

[67] J. R. Sanford and C. L. Wang, Brookhaven National Laboratory, AGS internal report, 1967 (unpublished);
C. L. Wang, Phys. Rev. Letters **25** 1068 (1970)

[68] R.A. Lundy *et al.*, Phys. Rev. Lett. **14** 504 (1966)

[69] D. Dekkers *et al.*, Phys. Rev. **137** B962 (1965)

[70] W.F. Baker *et al.*, Phys. Rev. Lett.**7** 101 (1971)

[71] A. Yamamoto, "Study On Low-Energy Intense Kaon Beam," KEK 81-13.

[72] Y. Cho *et al.*, Phys. Rev. **D 4** 7 (1971)

[73] J. G. Asbury *et al.*, Phys. Rev. **178** 2086 (1969)

[74] G. J. Marmer *et al.*, Phys. Rev. **179** 1294 (1969)

[75] G. J. Marmer *et al.*, Phys. Rev. **D 3** 1089 (1971)

[76] J. V. Allaby *et al.*, CERN Report No. CERN-TH-70-12 (unpablished)

[77] J. D. Jackson "Classical Electrodynamics" John Wiley &Sons, Inc

[78] C. -Y. Chien *et al.*, Phys. Lett. **35B** , 3 (1971).

[79] E. D. Commins & P. H. Bucksbaum, "Weak interaction of leptons and quarks" Cambridge University Press.

[80] C.H.Llewellyn Smith, Phys. Rep. **3C** 261 (1972).

[81] S.J.Barish *et al.*, Phys. Rev. **D16** 3103 (1977).

[82] S.Bonetti *et al.*, Nuovo. Cimento. **A38** 260 (1977).

[83] S.V.Belikov *et al.*, Z. Phys. **A320** 625.

[84] K.Abe *et al.*, Phys. Rev. Lett. **56** 1107 (1986).

[85] C.H.Albright *et al.*, Phys. Rev. **D14** 1780 (1976).

[86] D.Rein and L.M.Sehgal, Ann. of Phy. **133** 1780 (1981).
D.Rein Z.Phys. **C35** 43 (1987).

[87] M.Glück *et al.*, Z. Phy. **C67** 433 (1995)

[88] T.Sjostrand *et al.*, CERN-TH.7112/93 W5053/W5054

[89] S.J.Barish *et al.*, Phys. Rev. **D17** 1 (1978).

[90] H.Sarriko, *Neutrino 1979* 507 (1979).

[91] S.J.Barish *et al.*, Phys. Rev. **D19** 2521 (1979).

[92] P.Musset and J.P.Vialle, Phy. Rep. **C39** 1 (1978)

[93] J.E.Kim *et al.*, Rev. Mod. Phy. **53** 211 (1981)

[94] D.Rein and L.M.Sehgal, Nucl. Phy. **B223** 29 (1983).

[95] S.Adler *et al.*, Phy. Rev. **B135** 963 (1964)

[96] Private comminucation with Mastumoto (AIDA experiment group)

[97] T.Inagaki, Master thesis of Tokyo U. (1998: in Japanese, unpublished)

[98] J. E. Hill *et al.*, Beam Sci. Tech. **3** 18 (1998) .

[99] T.Maruyama *et al.*, K2K note 98-003 .

[100] T.Maruyama Doctor thesis University of Tohoku (2000)

[101] S. Kasuga *et al.*, Phys. Lett. **B 374**, 238 (1996).

[102] A.Sakai, Doctor thesis University of Tokyo (1997) (unpabulished)

[103] H. Leutz, Nucl. Instr. and Meth. **A 364**, 422 (1995).

[104] Delft high tech K.K., "The technical manual for the image-intensifiers" (1994) (written in Japanese).

[105] H. Park, *et al.*, talk presented at INSTR99, Hamamatsu, 1999;" Design, construction, and operation of SciFi tacking for K2K experiment",(to be published in special issue of Nucl.Instr and Meth.A.).

[106] M. Kitamura, "Study of the fake hit reduction in SCIFI detector", K2K internal report (1998)(written in Japanese).

[107] H. Kenmochi, master thesis (1998) (written in Japanese).

[108] T. Umeda, master thesis (1998) (written in Japanese).

[109] T.Inada Master thesis, Science university of Tokyo (1998)(written in Japanese).

[110] Shun'ichi Mine, "Report on the Data Analysis of the Cosmic–Ray Test of the Sci-Fi Tracker (I)", K2KNOTE/DET/SCI/97-005 (1997).

[111] H.Kume et al., Nucl. Instr. and Meth., **205**, 299 (1983)

[112] A.Suzuki et al., Nucl. Instr. and Meth., **A329** 299 (1993)

[113] C.McGrew PhD thesis, University of California at Irvine, 1994

[114] KEK Data Acquisition Development Working Group, "TKO Specification", KEK Report 85-10 (1985)

[115] T.Tanimori, H.Ikeda, M.Mori, K.Kihara, H.Kitagawa and Y.Haren, IEEE Trans. Nucl. Sci., bf NS-36, 497 (1989)

[116] G.J.Feldman and R.D. Cousins, Phys.Rev. **D57**,3873 (1998).

[117] MINUIT–Function Minimization and Error Analysis, Reference Manual, Computing and Networks Division (1994).

[118] D.Rein and L. M. Seligal, Ann. of Phys. **133** (1981) 1780; D.Rein, Z. Phys. **C53** (1992) 51

[119] E. Oltman et al., Z.Phys. **C53** (1992) 51.

[120] S.J.Barish et al., Phys. Rev. **D17** (1978) 1.

[121] H.Sarikko "Neutrino" 1979(1979) 507.

[122] T.A.Gabriel et al., IEEE Trans. Nulc. Sci 36,1

[123] K.Fujita, Master Thesis Tohoku University (1995)

[124] A.S.Carrol et al., Phys. Rev. **C14** (1976) 635

[125] E.Bracci et al., CERN/HERA 72-1 (1971)

[126] A.Morel et al., Limnology and Oceanography 22 (1977) 709

[127] K.Okumura, Doctor thesis University of Tokyo (1999)

[128] Y.Fukuda et al., Phys. Lett. **B433**, 9 (1998).

[129] Y.Fukuda et al., Phys. Lett. **B436**, 33 (1998).